UNIVERSITY OF OSLO
Department of informatics

**Simulation of nonlinear
ultrasound fields**

Mathematical modeling

Helge Fjellestad

Cand Scient Thesis

November 2000

Acknowledgment

This is the written part of the Cand. Scient. degree at the University of Oslo. It started in January 1999 and finished November 2000.

First, I would like to thank my supervisor, professor Sverre Holm, for giving me an interesting thesis and excellent guidance during this period.

I would also like to thank Kai Thomenius at GE Corporate Research & Development Schenectady, New York for giving me his implementation of the angular spectrum method as a starting point. He also went through the code with me when he was visiting this University and has answered questions via e-mail.

Simen Gaure from USIT has installed the FFT-code. I would like to thank him for this work. Also, I would like to thank the staff at the Library for being helpful and aiding in finding literature.

In addition I am greatly indebted to Ph.D. student Andreas Austeng for always being positive, giving very helpful discussions, finding literature and being interested in my work.

Finally, I will thank Keith Eikenes for proof-reading this thesis.

Oslo, November 2000

Helge Fjellestad

Contents

Chapter 1

Introduction

1.1 Medical ultrasound

The first ultrasound used in medicine was developed in 1947. It was not until about 1975 it became popular as a diagnostic technology. The introduction of B-mode imaging and real-time imaging was decisive. Today it is the most used diagnostic imaging system after X-ray.

Ultrasound has several advantages compared to other imaging methods. First, the equipment is smaller and cheaper than i.e. Magnetic Resonance. Because of the mechanical vibrations made by ultrasound it is possible to create localized heating. This heating may be used to heal certain diseases. If ultrasound is used with care, it is harmless. It is also possible to use Doppler motion to measure blood velocities, which do not exist in other forms of medical imaging systems. It is also non-invasive.

On the other hand there are disadvantages too. The penetration is shallow, about 10-15 cm. It is not possible to image through bones, which makes it difficult to image some objects.

1.2 Ultrasound imaging and nonlinear effects

The application of ultrasound in biomedical ultrasonic imaging requires stringent demands of image quality. Image quality is measured by contrast, axial and lateral resolution. It is important to get the best resolution and the highest contrast possible.

A lot of research has been done to improve image quality. Recently, it was discovered that finite-amplitude or nonlinear acoustics is a better way to model propagation in tissue [7]. This method is referred to as harmonic imaging. It is done by transmitting at one frequency and receive at the double. Images are

shown to have higher contrast and the lateral resolution is better. On the other hand, the penetration is shallower compared to linear propagation because of heavier attenuation at high frequencies.

1.3   Method used for modeling

To better understand the nonlinear effects, they are described mathematically and simulated on different transducers. Then it is possible to look at properties of the beam patterns to evaluate image quality.

There are different approaches to model wave propagation. In this thesis, one of the best methods for nonlinear propagation is used. It is the angular spectrum method combined with a frequency domain solution to Burgers equation to handle the generation of higher harmonics. This method can be used with non-axisymmetric sources and it is not restricted to a parabolic approximation.

1.4   Work in this thesis

This work is a continuation of another Cand. Scient. thesis, "Linear and nonlinear propagation of limited diffraction beams" by Johan-Fredrik Synnevåg, [19]. The referred thesis was restricted to circular symmetric sources. The simulator developed here is extended to non-symmetric sources. The starting point was a program received from Kai Thomenius, [20], which simulated a transducer using this technique. This program was modified to be able to simulate more general geometries.

Some 2D sparse arrays have been tested to see how good the image is with harmonic imaging in this case. The layouts have been chosen from an article written by Sverre Holm and Andreas Austeng [2]. They have tried to find the best sparse geometries for conventional ultrasound imaging.

Chapter two is an overview of ultrasound imaging used for medical purposes. Chapter three reviews the important properties of sound and sound propagation. A thorough derivation of the important Rayleigh-Sommerfeld integration formula is presented. Chapter four is devoted to the angular spectrum method. It is a description of the linear part of the algorithm implemented. Next, in chapter five, nonlinear acoustic is dealt with. Chapter five discusses the implementation and verifies the model. In chapter seven the simulation results are presented. The last chapter concludes the work done in this thesis and proposes some points for further investigation.

Chapter 2

Ultrasound imaging

Images made by ultrasound shows tissue structures and the images are in this case discussed for medical purposes. Ultrasound is the name of mechanical vibrations with frequencies higher than humans can hear. In medical ultrasound used today these frequencies are typically 2-10 MHz.

It started as a simple method, but today advanced techniques are used. A lot research has been done in developing electronic arrays used for beam forming. Optimal processing requires good mathematical models of the signal. Also electronic beam forming with arrays requires skills in three-dimensional wave propagation, as described in the next chapter.

2.1   History

The first ultrasound developed showed the intensity along a fixed beam. This is called the A-mode. Development continued by scanning a plane, first by mechanically moving the probe. However, moving was too slow for moving organs like the heart, so the M-mode was invented. This mode was made possible by electronic focusing. A pulse-echo technique was developed in 1948-49, and Doppler shift used to measure the velocity of blood was presented in 1957. Real time two-dimensional imaging was introduced in late sixties, early seventies.

Great progress in the area of integrated circuits, as well computer and display technology has made it possible to experiment and develop three dimensional imaging. This is still a field of intensive research. The speed of sound restricts the time it takes to capture an image and this is further limited in the case of moving objects. Data recordings from the heart has to be done at the same phase and ECG is used to synchronize the fire of pulse and the same phase of the heart.

2.2 Waves

Waves are good carriers of information if they are cleverly coded with adequate data. This requires an understanding of the physical process that generates and influences the wave as it propagates. In ultrasound, waves are transmitted towards a system, and the scattered waves are studied to obtain information about the system.

2.3 Resolution and frequency

Resolution of an ultrasound image is proportional to the wavelength or inversely proportional to the frequency. Therefore, to get good resolution one should use as high a frequency as possible. Unfortunately, attenuation increases with frequency, but harmonic imaging has made it possible to get better resolution and contrast.

2.4 Transducers

To measure and create waveforms one has to use a sensor. In ultrasound these sensors are called transducers. A transducer are converting one energy form into another. An ultrasound transducer is made of a plate of piezoelectric material with thin metal electrodes on each face. Voltage is coupled to the electrodes and this increases or decreases its thickness. Energy is transformed from acoustic vibrations into an electric voltage at the receiving end. Electric voltage is used to generate waves.

To get a good image, one wishes to send a delta impulse into the body and measure the impulse response from the tissue. This is impossible because of physical limitations. The transducer will oscillate for a while. This is called ringing. The longer the pulse time period, the shorter the frequency will be.

2.4.1 Arrays

Transducers used in medical ultrasound are compound of a various number of elements in different ways. A way to put together these sensors gives a certain network and is called an array. These arrays should be made in a clever way to get a good ultrasound image. It is possible to divide medical transducers into different classes.
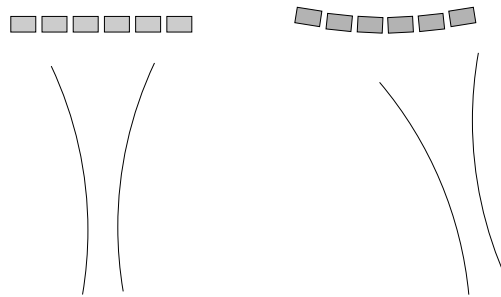
Figure 2.1: Linear and curvilinear arrays.

Phased linear arrays

These transducers are characterized by putting the elements in one direction. This is illustrated in figure 2.1. To radiate most energy in the forward direction, an inter-element distance smaller than $\lambda/2$ is required. This also prevents grating lobes, which is described later in this chapter. It is possible to make an appropriate delay on the elements to focus to a point or steer the beam in a certain direction. To get an adequate aperture a large number of elements are required. It is typically 64 to 128 elements and the width of the transducer are 10 to 20 mm. at 5 MHz.

Switched linear and curvilinear arrays

To avoid the long delays required for the previous type, only some elements may be used at each recording. It is then possible to sweep the beam horizontally. When the beam direction is normal to the array, the requirement of small element spacing can be given up. Then the elements can be several wavelengths long. This type of transducer is most used for flow imaging and Doppler measurements in vessels that are parallel to the skin.

To permit shaping of the array, the curvilinear array is introduced. If the array is concave-shaped, then the rectangular image format is changed to a sector like format. This is illustrated to the left in figure 2.1. The size of transducer can be reduced since the beam from this transducer is transferred more to the sides. This is especially advantageous when imaging the heart or when imaging a fetus.

Annular arrays

An array of concentric rings is called the annular array. The rings can be delayed differently to make a focus point. The advantage of the annular array is the symmetry. The beam is equal in all radial directions from the center
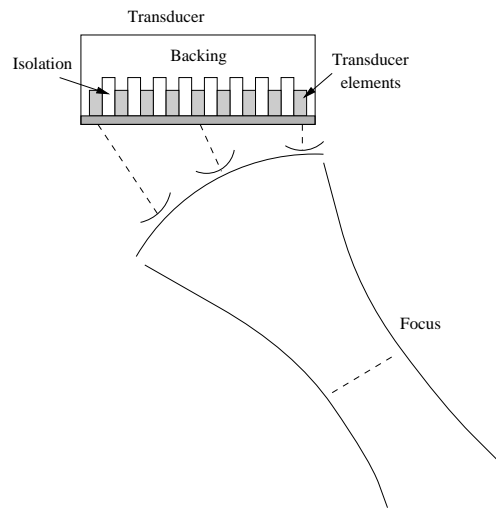
Figure 2.2: Example of delay focusing.

point.

2.4.2 Focusing

It is possible to focus energy in one certain point in space. This is done for example by shaping the transducer into a part of a spherical shell. Another way is to make a parabolic time delay of the elements. Diffraction gives us an unsharp focus. Sidelobes generate acoustic noise since they detect targets that are not along the beam direction. This noise causes a reduction in the contrast resolution. Contrast resolution is the ability to detect weak targets close to a strong one.

Wavelength is a critical parameter. If the diameter is constant and the frequency increases, the beam will be narrower. This delay focusing is not as sharp as geometrical focus. Apodization can be used to get lower sidelobes, but this will increase the mainlobe, so there is a trade-off between sidelobe level and mainlobe width.

An example of focusing by delay is shown in figure 2.2. The elements at the left edge has to be fired first because the distance to the focal point is longest in that direction.

2.4.3 Pulse echo imaging

When the ultrasound pulse hits a boundary between two tissue structures the pulse will be partially reflected and partially transmitted. Reflection depends on the difference between the impedances of the two materials. In soft tissue,

reflection is small. In bones and dense tissue almost everything is reflected. Modern electronics permits us to measure structures in soft tissue.

A-mode

This transmits a pulse and picks up the backscattered signal with the same transducer. The A-mode is displayed on an oscilloscope. Multiple reflections (reverberations) are an important factor that reduces image quality.

Time lag until the reflected pulse is received is

$$\tau = \frac{2r}{c} \tag{2.1}$$

where r is the distance into the tissue from the transducer face and c is the sound speed. Range resolution is defined as

$$\Delta r = \frac{cT_p}{2} = \frac{c}{2B_w} \tag{2.2}$$

where T_p is the length of transmitted pulse and B_w is the bandwidth of the pulse. This pulse is always a few oscillations long because of the ringing.

Attenuation occurs due to three different factors:

1. Absorption of wave energy to heat (strongest attenuation factor).

2. Reflection and scattering.

3. Diverging regions of the beam.

Attenuation in human tissue is approximately 1 dB/cm/MHz one way of propagation.

Distant targets receives a much weaker signal than near targets. The signal has to be amplified due to the depth and this is called time gain compensation (TGC). One wishes to use high frequencies to get good resolution, but they are more heavily attenuated so frequencies between 2.5-10 MHz are used depending on how deep the target is. The best possible resolution at the different depths are chosen.

M-mode

This is used of moving objects like the heart. Depth is shown in one axis, while the other axis represents time. Gray-scale represents the amplitude. The advantage of M-mode is that it is easy to see the movement of cardiac walls and valves.

Two dimensional (2D) amplitude imaging

This method scans a plane and show amplitude as gray scale. This makes it possible to scan sections of organs and display them in two dimensions. The scanning can be done by mechanically moving the transducer or swept over by steering the beam trough the scanning plane.

2.4.4 Resolution

The point targets smear out in the image. Point targets define the spatial resolution limit of the imaging system. Resolution along the direction of the beam is called the radial resolution and is determined by the length of the transmitted pulse. The resolution transverse to the beam is called the lateral resolution and is determined by the with of the beam.

If point targets are so close that they are covered by the same pulse, an interference is generated in the image. When these interferences occur in homogeneous tissue, the image gets a texture that is different from a sum of the individual images.

The time, T, it takes to generate an image is equal to the time per beam, T_b, multiplied by the number of beams, N. To collect data from depth R it takes $2R/c$ seconds to transmit and receive the data. In addition an extra period of time, T_0, has to be added to be sure that the pulse is sufficiently attenuated. The frame rate is then

$$\text{frame rate} = \frac{1}{T} = \frac{1}{NT_b} = \frac{1}{N(2R/c + T_0)}. \tag{2.3}$$

With a depth of 16 cm and 128 beams, the frame rate is 30 frames per second, which is acceptable for cardiac imaging. For greater depths, the number of beams has to be reduced, or a lower frame rate has to be accepted. Since the beam width increases with lower frequencies, it can compensate for the depth, or the image can be narrower.

2.4.5 Signal compression and processing

To visualize weak targets side by side the strong ones, a compression has to be done. This is similar to what the eye does to enable us to see in shadow and bright light. In ultrasound this compression is done by showing the image in logarithmic scale.

The gray scale does not have to be a linear mapping between input amplitude and the amplitude to display. If a small area in the input signal is of interest, then the gray scale mapping can be steep in that area so as to cover

more colors. An example of this being used, is where one wants to see the ventricle of the heart better.

2.4.6   Three-dimensional (3D) imaging

Ultrasound imaging in three dimensions was proposed already in the fifties, but available technology made it possible to process and display the large amount of data.

Todays computer technology is more fit for the requirements of this method. There are some fundamental limitations that make real-time imaging difficult. The speed of sound implies that scanning an image must take some time. To collect data at a depth of 15 cm one beam takes about 200 μsecs. A total of 100×100 beams requires 2 secs. to collect. For stationary objects, this is not a problem. But with moving objects, such as the heart, care must be taken. It is necessary to collect the data when the heart is in the same position, since recording have to be taken over several heart cycles. To trigger the recording at the correct times requires a stable heart rate, and the heart's position in the chest, due to breathing, must also be accounted for.

2.5   Beam forming

The elements of the transducer introduces flexibility of the beam. It is possible to focus the beam or steer the beam to another direction. This is an important technique to improve the image.

2.6   Sparse arrays

The most used 1-D arrays are the phased arrays with distance between elements $d = \lambda/2$. The array-pattern has a falling sidelobe level. In ultrasound this level has to be as low as possible to avoid noise in the images. There has been done a lot research in finding the array with best properties.

When extending to 2-D arrays, the element number increases greatly. It is hard to produce arrays that satisfy the sampling theorem in both dimensions. There are also too many channels to handle in a dense 2-D array. Therefore it is necessary to remove some elements. This process is called thinning. A raise in sidelobe level and mainlobe width has to be accepted because the sampling theorem is no longer fulfilled. There are many ways of choosing the array pattern and it is hard to find an optimal solution. This thesis does not deal with

algorithms for finding optimal layouts, but simulates nonlinear propagation of some known and assumed good geometries.

2.6.1 Grating lobes

If the element distance is periodic with element distance $d > \lambda/2$, grating lobes appear. Grating lobes are lobes that look like a main lobe, but is located at an angle different from zero. This results in energy transmitted to unwished directions. It makes beam forming not optimal, and should therefore be avoided.

Chapter 3

Waves and acoustic propagation

The goal of signal processing is to extract as much information as possible from our environment. In this case information is carried with propagating waves. It is therefore important to understand and describe mathematically the universal physical laws that underlie propagation.

Waves are important carriers of information. As the wave is propagating, the shape is preserved, and this is the core of using waves as carriers of information. Our ears are sensors for sound waves and by processing this information we are extremely good at estimate direction of sound.

3.1   Principles of sound theory

Sound can be regarded as a disturbance propagating in a medium. This disturbance is a traveling wave. A known example is a stone dropped into water. Then there will be a disturbance spread from where the stone got into the water. In this case the disturbance is transverse to the propagating wave and this type of waves is called shear or transversal waves. Another important example of transverse waves is electro-magnetic waves. The electric field is transversal to the propagation direction and the magnetic field is perpendicular to the electric field again. The other type of waves are longitudinal waves. In the case of ultrasound these are pressure waves propagating in tissue. Only transversal waves are of interest in ultrasound because the medium are assumed to be non-viscous[1]. Shear waves are heavily attenuated, so the assumption are valid.

A sound wave needs a medium to propagate in. This is different from electro-magnetic waves, which can propagate in vacuum. A sound wave is an oscillatory motion with small amplitude in a compressible fluid[2]. At each point

---

[1]No internal friction in the medium

[2]Liquids and gases

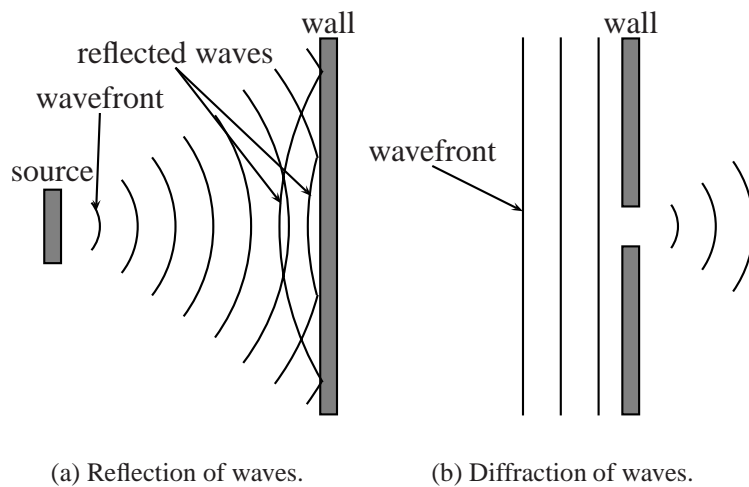(a) Reflection of waves.   (b) Diffraction of waves.

Figure 3.1: Wave propagation phenomena.

in the fluid, the sound wave causes alternate compression and rarefaction.

In fluid dynamics, which concerns the study of the motion of fluids, it is common to consider the phenomena as macroscopic. Thus fluid is regarded as a continuous medium. It means that any small volume element contains a very great number of molecules. Small volume elements are small compared to the medium, but large compared to molecules. This is the main assumption for the derivation of the following equations.

3.1.1 Reflection

Reflection is an important physical property that is explored in ultrasound. The transducer is transmitting a pulse and is receiving the reflection of the wave. Different acoustic impedance in the medium causes different amount of reflection of energy. If the impedance is small between two points, then the reflection is weak and the transmission further into the tissue is large. On the other hand, if the impedance is large, then almost all energy is reflected. This happens typically in ultrasound when waves hits bones. Almost no energy is transmitted further into tissue and this is the reason for not being able to image behind bones.

A basic case of reflection is illustrated in figure 3.1(a). It is assumed that all energy is reflected. Wavefronts hits the wall and changes the propagation direction. Then they are traveling back to the source.

3.1.2 Diffraction and Huygens' principle

When a plane wave is going through an aperture like the situation in figure 3.1(b) it is not propagating like an plane wave any more. It is deflected to a circular wave. This phenomenon is called diffraction. The amount of diffraction depends on the size of the aperture measured in wavelengths. If the aperture size is fixed and the frequency is increased, then the diffraction is decreasing. The aperture gets larger measured in wavelengths when the frequency increases. For instance, light has very high frequency and therefore it is diffracted little and the shadow edges are sharper.

This phenomenon was explained by Christian Huygens in the year 1678 [8]. Hugyens tried to develop a simple theory to explain why shadow edges were not sharp. If a light source is placed in front of an opaque screen with an aperture and the light intensity is observed a distance behind the screen, then it is not a sharp edge where the geometrical shadow starts. Actually, an interference pattern can be observed if the measurements are done exact.

Huygens postulated that each point on the wavefront can be considered as a new source of a secondary spherical disturbance. This simple idea is known as Huygens' principle and it was later given a mathematical foundation. One result is the Rayleigh-Sommerfeld diffraction formula

$$s(\vec{x}) = \frac{1}{j\lambda} \iint_A s(\vec{x}_h) \frac{\exp\{jkr\}}{r} \cos\theta \, dA. \tag{3.1}$$

The integral is taken over the aperture A, and dA represents an infinitesimal patch of area located at the position $\vec{x}_h$ within the hole. The variable θ represents the angle between the vector normal to the plane and the vector joining the aperture patch dA and the position $\vec{x}$. This is shown in figure 3.2.

A more throughout derivation of this equation is presented later in this chapter.

3.1.3 Phase and wavelength

An example of a wave can be a pure sinusoid. Points that are in the same position and are propagating in the same direction are in phase. The distance between two consecutive phase fronts is called a wavelength and is denoted by λ. There is a relation between velocity c, wavelength, and frequency

$$\lambda = \frac{c}{f}. \tag{3.2}$$

This means that if the sound velocity are doubled, then the wavelength is also doubled. Both, the velocity and the frequency has to be known to calculate the wavelength.
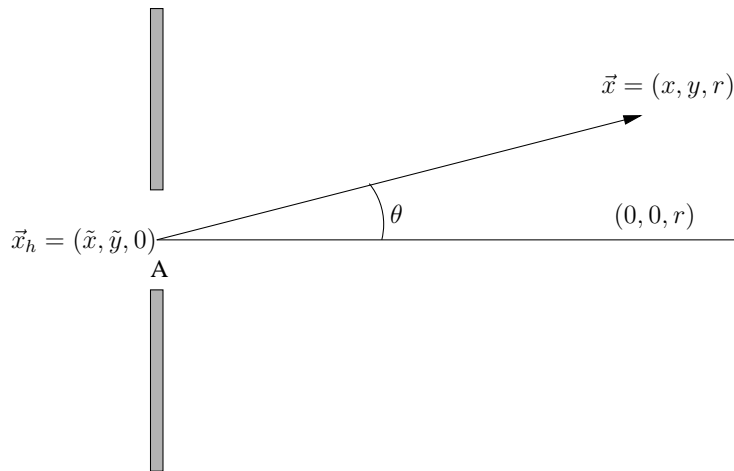
Figure 3.2: Coordinate system for Rayleigh-Sommerfeld diffraction formula.

3.1.4 Dispersion

Dispersive waves have frequency-dependent propagation characteristics. Unfortunately, this occurs frequently in the nature. Propagation velocity are dependent of the frequency. Different frequencies have different velocities and this causes distortion of the wave.

Evanescent waves

Some solutions to the dispersion relation are not real-valued, and when they are pure imaginary, the solution of the wave equation has a real negative exponent. The positive solution is physically impossible, because the wave can not grow as it is propagating. Because of this exponentially decaying, the solution is called an evanescent wave.

3.2 Derivation of the wave equation

An important and fundamental equation in array signal processing is the wave equation. Sometimes it is referred to as the equation in signal processing. In this section the linear three-dimensional wave equation in homogeneous medium is treated. To start the derivation, two fundamental equations from fluid dynamics are needed.

3.2.1 Fundamental equations of fluid dynamics

These two equations are called the equation of continuity and Euler's equation. The first is derived and the latter are presented without a derivation.

Let V_0 be some volume in space. The mass of fluid in this volume is $\int \rho dV$, where ρ is the fluid density and the integration is taken over the volume V_0. The mass of fluid flowing in unit time through an element $d\mathbf{f}$ of the surface bounding this volume is $\rho v \cdot d\mathbf{f}$. The magnitude of the vector $d\mathbf{f}$ is equal to the area of the surface element, and its direction is along the normal. By convention $d\mathbf{f}$ is chosen to be the outward normal. Then $\rho \vec{v} \cdot d\mathbf{f}$ is positive if the fluid is flowing out of the volume, and negative if the flow is into the volume. The total mass of fluid out of the volume V_0 in unit time is therefore

$$M_{\text{out}} = \oint \rho v \cdot d\mathbf{f} \tag{3.3}$$

where the integration is taken over the whole closed surface surrounding the volume in question.

The decrease per unit time in the mass of fluid in the volume V_0 can be written

$$-\frac{\partial}{\partial t} \int \rho \, dV. \tag{3.4}$$

Equating these expressions we have

$$\Delta M(V_0) = \frac{\partial}{\partial t} \int \rho dV = - \oint \rho v d\mathbf{f}. \tag{3.5}$$

By Green's formula this surface integral can be transformed to a volume integral

$$\oint \rho v d\mathbf{f} = \int \nabla(\rho v) dV \tag{3.6}$$

where ∇ is divergence. Then

$$\int \left[\frac{\partial \rho}{\partial t} + \nabla(\rho v) \right] dv = 0. \tag{3.7}$$

Since this equation must hold for any volume, the integrand must vanish

$$\frac{\partial \rho}{\partial t} + \nabla(\rho v) = 0. \tag{3.8}$$

This is the equation of continuity and it says that net ratio that flows into a fixed volume equals the mass increase in the volume.

The second equation is Euler's equation of motion of non-viscous fluids

$$\rho \frac{\partial \vec{v}}{\partial t} = -\nabla p. \tag{3.9}$$

where ∇ is the Laplace operator

$$\nabla = \frac{\partial}{\partial x} + \frac{\partial}{\partial y} + \frac{\partial}{\partial z} \tag{3.10}$$

A derivation of this can be found in i.e. [12].

3.2.2 Wave equation

From the two fundamental equations in the previous section, we can study flow of compressive fluids with small oscillations. With no sound present a fluid has an equilibrium state that is described with a constant pressure p_0, density ρ_0 and velocity $\vec{v}_0$. These are functions in space and time (x, y, z, t) and they describe the fluid state entirely. A disturbance (wave) can be regarded as a perturbation from this equilibrium state.

$$\mathbf{p} = \mathbf{p}_0 + \mathbf{p}', \qquad \rho = \rho_0 + \rho', \qquad \vec{v} = \vec{v}_0 + \vec{v}' \tag{3.11}$$

where p', ρ' and $\vec{v}'$ denotes small perturbations ($p' \ll p_0$ and $\rho' \ll \rho_0$) in pressure, density and velocity respectively. If the relation $\frac{\mathbf{p}}{\mathbf{p}_0} \ll 1$ is not valid, the disturbance is large and non-linear effects has to be considered. This is treated further in chapter 5.2.

By assuming constant specific entropy we have from the equation of state that p is a function of ρ, $\mathbf{p}(\rho)$. Then a Taylor expansion about zero of the pressure can be written as

$$\mathbf{p}'(\rho) = \left(\frac{\partial p}{\partial \rho}\right)_0 \rho' + \frac{1}{2}\left(\frac{\partial^2 p}{\partial \rho^2}\right)_0 (\rho')^2 + \dots \tag{3.12}$$

By retaining only the first term, we get a linear approximation to equation (3.7) and equation (3.9).

$$\frac{\partial p'}{\partial t} + \rho_0 \nabla \vec{v}' = 0 \tag{3.13}$$

$$\rho_0 \frac{\partial \vec{v}'}{\partial t} = -\nabla p' \tag{3.14}$$

If we let $c^2 = (\frac{\partial p}{\partial \rho})_0$, where c is the speed of sound, we have from equation (3.12)

16

$$p' = c^2 p' \tag{3.15}$$

and

$$\frac{1}{c^2}\frac{\partial p'}{\partial t} + \rho_0 \nabla \vec{v}' = 0. \tag{3.16}$$

By taking the time derivative of equation (3.16) this is the result

$$\frac{1}{c^2}\frac{\partial^2 p}{\partial t^2} + \rho_0 \nabla \left(\frac{\partial \vec{v}'}{\partial t}\right) = 0 \tag{3.17}$$

and by using equation (3.14) this is

$$\frac{1}{c^2}\frac{\partial^2 p'}{\partial t^2} - \nabla \nabla p' = 0 \tag{3.18}$$

or rearranged to the more familiar equation

$$\nabla^2 p' - \frac{1}{c^2}\frac{\partial^2 p'}{\partial t^2} = 0. \tag{3.19}$$

This is the wave equation in three dimensions. By replacing ∇ we get

$$\left(\frac{\partial^2}{\partial x^2} + \frac{\partial^2}{\partial y^2} + \frac{\partial^2}{\partial z^2} + \frac{\partial^2}{c^2 \partial t^2}\right) \mathbf{p}' = 0 \tag{3.20}$$

3.3 Solution of wave equation

There are many ways to solve the wave equation. The rest of this chapter presents two solutions of the equation. First, a separable solution is assumed. At last a general solution is derived.

3.3.1 Separable solution

A common way to solve differential equations are to assume a separable solution. The solution should have the form

$$s(x, y, z, t) = f(x)g(y)h(z)p(t). \tag{3.21}$$

Exponential functions are convenient to solve differential equations, and it is assumed that $s(x, y, z, t)$ has the form

$$s(x, y, z, t) = A e^{j(\omega t - k_x x - k_y y - k_z z)}. \tag{3.22}$$

When this equation is replaced into the wave equation and the s-function is cancelled, this relation appears

$$k_x^2 + k_y^2 + k_z^2 = \frac{\omega^2}{c^2}. \qquad (3.23)$$

As long as this constraint is satisfied, the signal satisfy the wave equation. It can be shown that c denotes the speed of sound [11].

The wave equation is a linear equation, which means that if $s_1(\vec{x}, t)$ and $s_2(\vec{x}, t)$ are two solutions to the wave equation, then a linear combination $as_1(\vec{x}, t) + bs_2(\vec{x}, t)^3$ is also a solution. Then more complicated solutions can be found by combining solutions on the form

$$s(\vec{x}, t) = s(t - \vec{\alpha} \cdot \vec{x}) = \sum_{-\infty}^{\infty} S_n e^{jn\omega_0(t - \vec{\alpha} \cdot \vec{x})}. \qquad (3.24)$$

This is a harmonic series. Because of the Fourier theory, an arbitrary periodic waveform $s(u)$ with period $T = 2\pi/\omega_0$ can be written by such a series. Therefore every signal is a solution to the wave equation.

3.3.2 Rayleigh-Sommerfeld integral

In this section a method to calculate the field distribution in a point, which is called Rayleigh-Sommerfeld integral, is derived. The radiation source can have an arbitrary shape in the plane. Apodization functions are also included in the equation. This method is used in Ultrasim, a matlab toolbox developed at the University of Oslo.

First, Kirchoff's solution of the problem is presented and then the Rayleigh-Sommerfeld integral is derived from this. The idea of Rayleigh-Sommerfeld integral was described in section 3.1.2 and here is the more throughout derivation given.

The field is determined by the source and the medium. It is assumed that the medium is isotropic and homogeneous. This means that the waves propagate equal in all directions. In addition the diffraction aperture must be large compared by a wavelength and the field must not be observed too close to the aperture. Diffraction is sound waves ability to bend around corners or to spread when propagating through a little hole or aperture and this was described in section 3.1.2.

---

[3] a and b are scalars

Monochromatic waves

First, a scalar function $u(P, t)$ is introduced which denotes the disturbance in position $P = (x, y, z)$ at time t. In this case it is sound pressure, but the theory is also available for electric or magnetic field strengths. For monochromatic[4] waves this type of waves can be described with the function.

$$u(P, t) = U(P) \cos[2\pi ft + \phi(P)] \tag{3.25}$$

$U(P)$ denotes the amplitude and $\phi(P)$ the phase at position P and frequency f. This can be written in a more compact form by using complex notation.

$$u(P, t) = Re[\mathbf{U}(P)e^{-j2\pi ft}] \tag{3.26}$$

where $\mathbf{U}(P)$ is the following complex function

$$\mathbf{U}(P) = U(P)e^{j\phi(P)} \tag{3.27}$$

Since the disturbance, $u(P, t)$, represents a wave, it has to satisfy the wave equation 3.20. A sufficient description of the disturbance when the time is known, is $\mathbf{U}(P)$. It is thus sufficient to consider only $\mathbf{U}(P)$ further. If $u(P, t)$ is replaced in the wave equation, the result is

$$(\nabla^2 + k^2)\mathbf{U} = 0 \tag{3.28}$$

where

$$k = 2\pi\frac{f}{c} = \frac{2\pi}{\lambda}. \tag{3.29}$$

Equation (3.28) is called Helmholtz equation. To calculate the field in a given observation point, we need Green's theorem.

Green's theorem

Let $\mathbf{U}(P)$ and $\mathbf{G}(P)$ be two complex-valued functions and let S be a closed surface surrounding a volume V. If $\mathbf{U}$ and $\mathbf{G}$, and their first and second partial derivate are single-valued and continuous within and on S, then we have

$$\iiint_V (\mathbf{G}\nabla^2\mathbf{U} - \mathbf{U}\nabla^2\mathbf{G})dv = \iint_S \left(\mathbf{G}\frac{\partial\mathbf{U}}{\partial n} - \mathbf{U}\frac{\partial\mathbf{G}}{\partial n}\right)ds \tag{3.30}$$

---

[4]Means one frequency.

where $\frac{\partial}{\partial n}$ signifies a partial derivative in the outward normal direction at each point on S.

This theorem is in many respects the foundation of scalar diffraction theory. We will now use the theorem with a special choosen Green's function ($\mathbf{G}$).

$$\mathbf{G}(P_1) = \frac{e^{jkr_{01}}}{r_{01}} \tag{3.31}$$

where P_1 is an arbitrary point on S' (defined in equation (3.32)) and r_{01} denotes the length of the vector $\vec{r}_{01}$ from P_0 to P_1. To use Green's theorem, the point P_0 has to be avoided since $\mathbf{G}(P_0)$ is not defined. It can be done by introducing a spherical surface surrounding P_0, S_ϵ (the symbol ϵ denotes the radius). This is shown in figure 3.3. Green's theorem is used on the volume, V', between S and S_ϵ. It is illustrated by the shaded area in the figure. The surface of integration is then

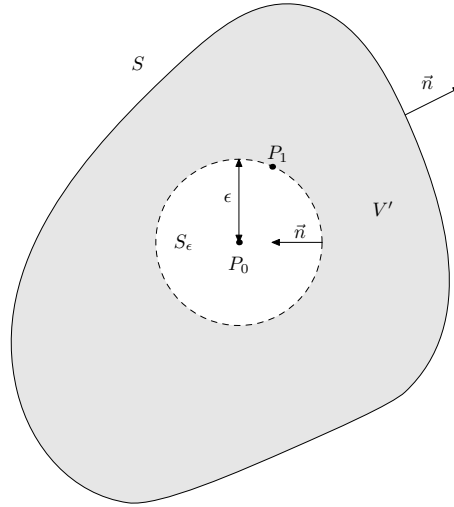$$S' = S + S_\epsilon. \tag{3.32}$$

Figure 3.3: Surface of integration

The functions $\mathbf{U}$ and $\mathbf{G}$ has to satisfy Helmholtz equation (3.28).

$$(\nabla^2 + k^2)\mathbf{U} = 0 \qquad (\nabla^2 + k^2)\mathbf{G} = 0 \tag{3.33}$$
$$\nabla^2\mathbf{U} = -k^2\mathbf{U} \qquad \nabla^2\mathbf{G} = -k^2\mathbf{G}. \tag{3.34}$$

If this is used in left side of Green's theorem, we get

$$\iiint\limits_{V'} (\mathbf{G}\nabla^2\mathbf{U} - \mathbf{U}\nabla^2\mathbf{G})dv = -\iiint\limits_{V'} (\mathbf{G}\mathbf{U}k^2 - \mathbf{U}\mathbf{G}k^2)dv \equiv 0 \quad (3.35)$$

when we know also from the theorem that

$$\iint\limits_{S'} \left(\mathbf{G}\frac{\partial\mathbf{U}}{\partial n} - \mathbf{U}\frac{\partial\mathbf{G}}{\partial n} \right) ds = 0 \tag{3.36}$$

or

$$-\iint\limits_{S_\epsilon} \left(\mathbf{G}\frac{\partial\mathbf{U}}{\partial n} - \mathbf{U}\frac{\partial\mathbf{G}}{\partial n} \right) ds = \iint\limits_{S} \left(\mathbf{G}\frac{\partial\mathbf{U}}{\partial n} - \mathbf{U}\frac{\partial\mathbf{G}}{\partial n} \right) ds. \tag{3.37}$$

We have an expression for the partial derivative to $\mathbf{G}$ in the normal direction

$$\frac{\partial\mathbf{G}(P_1)}{\partial n} = \cos(\vec{n}, \vec{r}_{01})\left(jk - \frac{1}{r_{01}} \right) \frac{e^{jkr_{01}}}{r_{01}} \tag{3.38}$$

where $\cos(\vec{n}, \vec{r}_{01})$ denotes cosine to the angle between the outward normal, $\vec{n}$, and the vector $\vec{r}_{01}$.

When P_1 are on S_ϵ, we get $\cos(\vec{n}, \vec{r}_{01}) = \cos(\pi) = -1$ and the equations can be simplified to

$$\mathbf{G}(P_1) = \frac{e^{jk\epsilon}}{\epsilon} \qquad \text{og} \qquad \frac{\partial\mathbf{G}(P_1)}{\partial n} = \frac{e^{jk\epsilon}}{\epsilon}\left(\frac{1}{\epsilon} - jk \right) \tag{3.39}$$

If we let ϵ be arbitrary small, we get

$$\iint\limits_{S_\epsilon} \left(\mathbf{G}\frac{\partial\mathbf{U}}{\partial n} - \mathbf{U}\frac{\partial\mathbf{G}}{\partial n} \right) ds = \lim_{\epsilon\to 0} 4\pi\epsilon^2 \left[\frac{\partial\mathbf{U}(P_0)}{\partial n}\frac{e^{jk\epsilon}}{\epsilon} - \mathbf{U}(P_0)\frac{e^{jk\epsilon}}{\epsilon}(\frac{1}{\epsilon} - jk) \right]$$
$$= -4\pi\mathbf{U}(P_0). \tag{3.40}$$

If this is substituted into equation (3.37), we get

$$\mathbf{U}(P_0) = \frac{1}{4\pi} \iint\limits_{S} \left(\frac{\partial\mathbf{U}}{\partial n}\frac{e^{jkr_{01}}}{r_{01}} - \mathbf{U}\frac{\partial}{\partial n}\frac{e^{jkr_{01}}}{r_{01}} \right) ds. \tag{3.41}$$

21

This equation is called Helmholtz and Kirchhoffs integral theorem.

This is the general theory. To get a step further, some additional assumptions have to be done.

The integral theorem can be used to consider diffraction of a plane screen. If we consider an infinite opaque screen with a small aperture, equation (3.41) can be used to calculate the field in a point P_0 behind the screen. A surface that is easy to calculate have to be chosen. A good choice for the surface is a circle with radius R surrounding P_0 on the screen, and this surface is called S_2. To get a closed surface a new surface is added along the screen (S_1). The construction is shown in figure 3.4. It can be shown that the contribution from S_2 is zeros when $R \to \infty$, [8]. Then it is sufficient to integrate the surface over S_1. To simplify the expression a step further, Krichhoff did two assumptions.
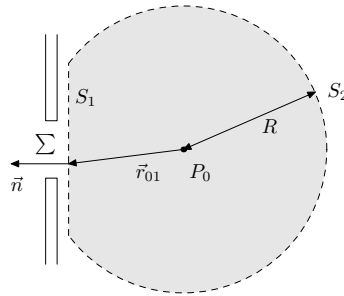

Figure 3.4: Diffraction of a plane screen.

1. Across the surface Σ, the field distribution $\mathbf{U}$ and its derivative $\frac{\partial \mathbf{U}}{\partial n}$ are exactly the same as they would be in the absence of the screen.

2. Over the portion of S_1 that lies in the geometrical shadow of the screen, the field distribution $\mathbf{U}$ and its derivative $\frac{\partial \mathbf{U}}{\partial n}$ are identically zero.

These assumptions are not correct. In the first it is claimed that removing the screen does not influence the field. This is not completely valid because the screen will influence at the edges. To the other assumption it can be said that the shadow is not perfect behind the screen because the field is some wavelengths behind.

If we in addition assume that the wavelength is a lot smaller that the size of the aperture, then these assumptions are reasonable. The special effects can be neglected, just like these assumptions does. Experiments show good agreements with the two assumptions.

Rayleigh-Sommerfeld integral

The two assumptions that Kirchhoff made, are shown to be incompatible. They can not be true simultaneous. Then it was interesting to search for a better mathematical model, such that this contradiction was removed. This work was done by Sommerfeld.

The problem was a result that says if a potential function and its derivate disappears on a finite curve, then it has to disappear in the whole plane. This means that the assumption that the field is zero behind the screen gives a zero-field at the whole screen. The physical situation shows that this is not the case.

Sommerfeld did not need to assume boundary conditions at both, in the disturbances and the normal derivative at the same time. This was done by choosing another Green's function. Consider again the equation

$$U(P_0) = \frac{1}{4\pi} \iint_{S_1} \left(\frac{\partial U}{\partial n} G - U \frac{\partial G}{\partial n} \right) ds. \tag{3.42}$$

We wish a Green's function that is valid in this equation and in addition either G or $\frac{\partial G}{\partial n}$ disappears over the whole surface S_1. Then the discrepancy to Kirchhoff will disappear.

Sommerfeld showed that there exists a Green's function that satisfies these requirements. He thought that G is constructed from two point-sources, P_0 and $\tilde{P}_0$. These sources are mirrored, so they are located at different sides of the screen and has equal distance from the screen. They have the same wavelength, λ, and oscillates with $180°$ phase difference. This means that the field on S_1 is zero, since the two sources cancel each other there. The new Green's function is given by

$$G_-(P_1) = \frac{e^{jkr_{01}}}{r_{01}} - \frac{e^{jk\tilde{r}_{01}}}{\tilde{r}_{01}} \tag{3.43}$$

here r_{01} denotes the distance from $\tilde{P}_0$ to P_1. The expression to the normal derivate to G_- are given by

$$\frac{\partial G_-}{\partial n} = \cos(\vec{n}, \vec{r}_{01}) \left(jk - \frac{1}{r_{01}} \right) \frac{e^{jkr_{01}}}{r_{01}} - \cos(\vec{n}, \tilde{\vec{r}}_{01}) \left(jk - \frac{1}{\tilde{r}_{01}} \right) \frac{e^{jk\tilde{r}_{01}}}{\tilde{r}_{01}}. \tag{3.44}$$

At a point, P_1, on S_1 we have

$$r_{01} = \tilde{r}_{01} \tag{3.45}$$

$$\cos(\vec{n}, \vec{r}_{01}) = -\cos(\vec{n}, \tilde{\vec{r}}_{01}) \tag{3.46}$$

23

then we get this result at the chosen surface

$$\mathbf{G}_-(P_1) = 0 \tag{3.47}$$

$$\frac{\partial \mathbf{G}_-(P_1)}{\partial n} = 2 \cos(\vec{n}, \vec{r}_{01}) \left(jk - \frac{1}{r_{01}} \right) \frac{e^{jkr_{01}}}{r_{01}}. \tag{3.48}$$

By substitution of $\mathbf{G}_-$ with $\mathbf{G}$ in equation (3.42), we get

$$\mathbf{U}(P_0) = \frac{1}{4\pi} \iint\limits_{S_1} -\mathbf{U}(P_1) \left[2 \cos(\vec{n}, vecr_{01}) \left(jk - \frac{1}{r_{01}} \right) \frac{e^{jkr_{01}}}{r_{01}} \right] ds. \tag{3.49}$$

This expression can be simplified by assuming that $r_{01} \gg \lambda$.

$$\mathbf{U}(P_0) = \frac{1}{j\lambda} \iint\limits_{S_1} \mathbf{U}(P_1) \frac{e^{jkr_{01}}}{r_{01}} \cos(\vec{n}, \vec{r}_{01}) ds \tag{3.50}$$

Now Kirchhoffs second assumption can be used on $\mathbf{U}$ alone. This leads to

$$\mathbf{U}(P_0) = \frac{1}{j\lambda} \iint\limits_{\Sigma} \mathbf{U}(P_1) \frac{e^{jkr_{01}}}{r_{01}} \cos(\vec{n}, \vec{r}_{01}) ds. \tag{3.51}$$

By using a source in a point, P_2, to the left of the screen, that has distance r_{21} to the point P_1 and are sending out a frequency

$$\mathbf{U}(P_1) = \frac{e^{jkr_{21}}}{r_{21}} \tag{3.52}$$

then the Rayleigh-Sommerfeld integral is

$$\mathbf{U}(P_0) = \frac{1}{j\lambda} \iint\limits_{\Sigma} \mathbf{U}(P_1) \frac{e^{jk(r_{21}+r_{01})}}{r_{21}r_{01}} \cos(\vec{n}, \vec{r}_{01}) ds. \tag{3.53}$$

Chapter 4

Angular spectrum method

In this chapter we will take another approach to the problem of scalar diffraction. This method is called the angular spectrum and is closely related to linear time-invariant filters. Implementation is much easier with this approach and it is a widely used method to simulate acoustic fields. The idea is to look at the Fourier transform with respect to a specially chosen plane. The Fourier-components can be regarded as plane waves traveling in different directions. The field can be calculated by summarizing the contributions from the different components.

The problem considered, is to calculate the beam pattern of a transducer. As an input to the algorithm, the initial velocity pressure in a certain plane is given. From this it is possible to calculate the field of a parallel plane at an arbitrary distance. This is referred to as forward projection of acoustic field data [18]. The theory may be applied to field pressure distribution as well.

4.1   Background

There are various methods to solve the forward projection problem. These can be divided into two main categories:

1. Time-domain solutions.

2. Frequency-domain solutions.

An example of the first method is the Rayleigh integral formula, which was derived in section 3.3.2. Methods in the second category are mainly based on the Fourier transform.

The angular spectrum method was originally developed as a technique to model the propagation from a known field distribution to a parallel plane a

certain distance away. To simulate realistic acoustic propagation, a number of effects have to be included. It is important to consider attenuation, dispersion, diffraction, refraction and phase distortion. All these phenomena are included in the model. Also nonlinear acoustic propagation was incorporated in the model and this is discussed in chapter 5. Multiple reflections are not developed by using the angular spectrum method yet. In this work, only a point scatterer is considered.

The name angular spectrum itself explains the physical interpretation of the method. Different components of the Fourier transform can be explained as plane waves propagating in different directions.

4.2 Definition of angular spectrum

We will consider a wave in space that is traveling in a positive z-direction. First, we have to consider the xy-plane. The complex field in this plane can be denoted by $\mathbf{U}(x, y, 0)$. The objective is to find the field, $\mathbf{U}(x, y, z)$, at a new point P_0 with coordinates (x, y, z).

In the xy-plane the function $\mathbf{U}$ gets the two-dimensional Fourier transform

$$\mathbf{A}_0(f_X, f_Y) = \iint\limits_{-\infty}^{\infty} e^{-j2\pi(f_X x + f_Y y)} dx dy. \tag{4.1}$$

The Fourier transform decomposes a complicated function into a collection of simpler complex-exponential functions. The inverse transform of the spectrum is given by

$$\mathbf{U}(x, y, 0) = \iint\limits_{-\infty}^{\infty} \mathbf{A}_0(f_X, f_Y) e^{j2\pi(f_X x + f_Y y)} df_X df_Y. \tag{4.2}$$

The equation for a unit-amplitude plane wave traveling in the direction cosine(α, β, γ) is

$$\mathbf{B}(x, y, z) = e^{j\frac{2\pi}{\lambda}(\alpha x + \beta y + \gamma z)} \tag{4.3}$$

where

$$\gamma = \sqrt{1 - \alpha^2 - \beta^2}. \tag{4.4}$$

This means that in the plane $z = 0$, the complex exponential function $e^{j2\pi(f_X x + f_Y y)}$ can be regarded as a plane wave traveling in direction cosine(α, β, γ), where

$$\alpha = \lambda f_X \qquad \beta = \lambda f_Y \qquad \gamma = \sqrt{1 - (\lambda f_X)^2 - (\lambda f_Y)^2}. \qquad (4.5)$$

The complex amplitude of the plane wave component is $\mathbf{A}_0(f_X, f_Y)df_X df_Y$ evaluated at $(f_X = \alpha/\lambda, f_Y = \beta/\lambda)$. Therefore the function

$$\mathbf{A}_0\left(\frac{\alpha}{\lambda}, \frac{\beta}{\lambda}\right) = \iint\limits_{-\infty}^{\infty} \mathbf{U}(x, y, 0)e^{-j2\pi(\frac{\alpha}{\lambda}x + \frac{\beta}{\lambda}y)}dxdy \qquad (4.6)$$

is called the angular spectrum to the disturbance $\mathbf{U}(x, y, 0)$.

4.3 Calculating field by angular spectrum

The problem now is to find the field $\mathbf{U}$ in a plane parallel with the xy-plane, but at a distance z from it. The angular spectrum to $\mathbf{U}(x, y, z)$ is given by

$$\mathbf{A}\left(\frac{\alpha}{\lambda}, \frac{\beta}{\lambda}; z\right) = \iint\limits_{-\infty}^{\infty} \mathbf{U}(x, y, z)e^{-j2\pi(\frac{\alpha}{\lambda}x + \frac{\beta}{\lambda}y)}dxdy. \qquad (4.7)$$

We wish to find a relation between $\mathbf{A}_0(\frac{\alpha}{\lambda}, \frac{\beta}{\lambda})$ and $\mathbf{A}(\frac{\alpha}{\lambda}, \frac{\beta}{\lambda}; z)$. To find this relation, we note that $\mathbf{U}$ can be written as the inverse transform

$$\mathbf{U}(x, y, z) = \iint\limits_{-\infty}^{\infty} \mathbf{A}\left(\frac{\alpha}{\lambda}, \frac{\beta}{\lambda}; z\right) e^{j2\pi(\frac{\alpha}{\lambda}x + \frac{\beta}{\lambda}y)}d\frac{\alpha}{\lambda}d\frac{\beta}{\lambda}. \qquad (4.8)$$

In addition $\mathbf{U}$ has to satisfy the Helmholtz equation (3.28) in all source free points. By applying this to equation (4.8), $\mathbf{A}$ has to satisfy the differential equation

$$\frac{d^2}{dz^2}\mathbf{A}\left(\frac{\alpha}{\lambda}, \frac{\beta}{\lambda}; z\right) + \left(\frac{2\pi}{\lambda}\right)^2 [1 - \alpha^2 - \beta^2]\mathbf{A}\left(\frac{\alpha}{\lambda}, \frac{\beta}{\lambda}; z\right) = 0. \qquad (4.9)$$

This second order differential equation has an elementary solution

$$\mathbf{A}\left(\frac{\alpha}{\lambda}, \frac{\beta}{\lambda}; z\right) = \mathbf{A}_0\left(\frac{\alpha}{\lambda}, \frac{\beta}{\lambda}\right) e^{j\frac{2\pi}{\lambda}\sqrt{1-\alpha^2-\beta^2}z}. \tag{4.10}$$

Since there is a square root function in the complex exponential function, three cases have to be considered. The first case is when α and β satisfies

$$\alpha^2 + \beta^2 < 1. \tag{4.11}$$

Then the effect of propagation over the distance z is a change of the relative phase of the different components in the angular spectrum. Since every plane wave is propagating at different angles, they are traveling different distances to a given observation point and relative phase-delays are introduced.

When α and β are such that

$$\alpha^2 + \beta^2 > 1 \tag{4.12}$$

another explanation is needed. In this case the square root in equation (4.10) is purely imaginary, and the equation can be written as

$$\mathbf{A}\left(\frac{\alpha}{\lambda}, \frac{\beta}{\lambda}; z\right) = \mathbf{A}_0\left(\frac{\alpha}{\lambda}, \frac{\beta}{\lambda}\right) e^{-\mu z} \tag{4.13}$$

where

$$\mu = \frac{2\pi}{\lambda}\sqrt{\alpha^2 + \beta^2 - 1}. \tag{4.14}$$

Since μ is a positive integer, these wave components are strongly attenuated in the wave propagation. These components of angular spectrum are called evanescent waves.

The borderline case

$$\alpha^2 + \beta^2 = 1 \tag{4.15}$$

corresponds to plane waves that are perpendicular to the z-axis and are not contributing to a gain in z-direction.

The conclusion is that the disturbance observed in (x, y, z) can be written as an initial angular spectrum by inverse-transforming equation (4.10). This gives

$$\mathbf{U}(x, y, z) = \int\!\!\!\int_{-\infty}^{\infty} \mathbf{A}_0\left(\frac{\alpha}{\lambda}, \frac{\beta}{\lambda}\right) e^{j\frac{2\pi}{\lambda}\sqrt{1-\alpha^2-\beta^2}z} e^{j2\pi(\frac{\alpha}{\lambda}x + \frac{\beta}{\lambda}y)} d\frac{\alpha}{\lambda} d\frac{\beta}{\lambda}. \tag{4.16}$$

28

4.4 Diffraction by linear time-invariant filter

Again, we are considering the spreading of a wave from the plane $z = 0$ to a parallel plane with distance z. The disturbance $\mathbf{U}(x, y, 0)$ in the plane can be regarded as a mapping of the propagation phenomenon to a new field $\mathbf{U}(x, y, z)$. It will be shown that the propagation phenomenon behaves like a linear, time-invariant system, and can be characterized by a simple transfer function.

The linearity has already been discussed. It follows directly from the linearity of the wave equation. The time-invariant property can be shown by deriving an expression of the transfer function. If there exists a transfer function, then the system has to be time-invariant and the result follows.

To find a transfer function, the angular spectrum is considered. Instead of using the angular spectrum as a function of direction cosine(α, β), the spatial spectrum (f_X, f_Y) is used. The relation between these representations is given by equation (4.5).

Let the spatial spectrum to $\mathbf{U}(x, y, z)$ be represented by $\mathbf{A}(f_X, f_Y; z)$, while the spectrum to $\mathbf{U}(x, y, 0)$ can be written as $\mathbf{A_0}(f_X, f_Y)$. Then $U(x, y, z)$ can be expressed by

$$\mathbf{U}(x, y, z) = \iint\limits_{-\infty}^{\infty} \mathbf{A}(f_X, f_Y; z) e^{j2\pi(f_X x + f_Y y)} df_X df_Y. \qquad (4.17)$$

In addition, from equation (4.16) we have

$$\mathbf{U}(x, y, z) = \iint\limits_{-\infty}^{\infty} \mathbf{A_0}(f_X, f_Y) e^{j2\pi\frac{z}{\lambda}\sqrt{1-(\lambda f_X)^2-(\lambda f_Y)^2}} e^{j2\pi(f_X x + f_Y y)} df_X df_Y.$$

$$(4.18)$$

A comparison of these equations shows that

$$\mathbf{A}(f_X, f_Y; z) = \mathbf{A_0}(f_X, f_Y) e^{j2\pi\frac{z}{\lambda}\sqrt{1-(\lambda f_X)^2-(\lambda f_Y)^2}} \qquad (4.19)$$

and the propagation phenomenon can be regarded as the transfer function $\mathbf{H}$ given by

$$\mathbf{H}(f_X, f_Y) = \frac{\mathbf{A}(f_X, f_Y; z)}{\mathbf{A_0}(f_X, f_Y)} = e^{j2\pi\frac{z}{\lambda}\sqrt{1-(\lambda f_X)^2-(\lambda f_Y)^2}} \qquad (4.20)$$

If the distance z is at least some wavelengths, then the evanescent waves can be neglected and we have the transfer function

$$\mathbf{H}(f_X, f_Y) = \begin{cases} e^{j2\pi\sqrt{1-(\lambda f_X)^2-(\lambda f_Y)^2}} & f_X^2 + f_Y^2 < \frac{1}{\lambda^2} \\ 0 & \text{otherwise} \end{cases} \quad (4.21)$$

Until now, the equations have been presented in the frequency domain. Another method to find the propagation function is given in [22]. In this article the functions are in the spatial domain and the exact equation for the Rayleigh-Sommerfeld integral is

$$\mathbf{U}(P_0) = \frac{1}{j\lambda} \iint\limits_{S_1} \mathbf{U}(P_1) \frac{e^{jkr_{01}}}{r_{01}} \cos(\vec{n}, \vec{r}_{01}) ds + \frac{1}{2\pi} \iint\limits_{S_1} \mathbf{U}(P_1) \frac{e^{jkr_{01}}}{r_{01}^2} \cos(\vec{n}, \vec{r}_{01}) ds. \quad (4.22)$$

The point P_1 is on the aperture and the new point to evaluate is P_0. By changing to Cartesian coordinates with the equations

$$r_{01} = \sqrt{(x_0 - x_1)^2 + (y_0 - y_1)^2 + z^2} \quad \text{and} \quad z = r_{01} \cos(\vec{n}, \vec{r}_{01}) \quad (4.23)$$

we get

$$\mathbf{U}(x_0, y_0, z) = \frac{1}{j\lambda} \iint\limits_{x_1 y_1} \mathbf{U}(x_1, y_1) \frac{r_{01} \cos(\vec{n}, \vec{r_{01}}) e^{jk\sqrt{(x_0-x_1)^2+(y_0-y_1+z^2)^2}}}{(x_0 - x_1)^2 + (y_0 - y_1)^2 + z^2} dx_1 dy_1$$

$$+ \frac{1}{2\pi} \iint\limits_{x_1 y_1} \mathbf{U}(x_1, y_1) \frac{r_{01} \cos(\vec{n}, \vec{r_{01}}) e^{jk\sqrt{(x_0-x_1)^2+(y_0-y_1)^2+z^2}}}{((x_0 - x_1)^2 + (y_0 - y_1)^2 + z^2)^{3/2}} dx_1 dy_1. \quad (4.24)$$

This is a convolution integral and can be written as

$$\mathbf{U}(x_0, y_0, z) = \mathbf{U}(x, y, z) * h(x, y, z) \quad (4.25)$$

where

$$h(x, y, z) = \frac{1}{j\lambda} \iint\limits_{x_1 y_1} \frac{z}{x_1^2 + y_1^2 + z^2} e^{jk\sqrt{x_1^2+y_1^2+z^2}} dx_1 dy_1$$

$$+ \frac{1}{2\pi} \iint\limits_{x_1 y_1} \frac{z}{(x_1^2 + y_1^2 + z^2)^{3/2}} e^{jk\sqrt{x_1^2+y_1^2+z^2}} dx_1 dy_1. \quad (4.26)$$

This is the exact solution to the problem. It is used to simulate fields where the propagation distance is small and the last expression can not be neglected. To derive the transfer function from the last equation, the second expression is neglected. This is done because propagation over greater distances are assumed.

4.5 Simulation using the angular spectrum method

The Christopher and Parker articles, [5] and [6], describes how to simulate a field from circular transducers using the angular spectrum. The implementation used here is an extension to non-symmetric sources.

It is straightforward to extend the formulas to non-symmetric sources. It requires a lot of more calculation compared to the symmetric ones. A complete description of the field is present when the field distribution is known along the radius in the symmetric case. But when extending to non symmetric, the whole field has to be considered, which leads to one additional dimension in the calculations.

4.5.1 Linear propagation

There exists two different approaches to the propagation problem. The difference is whether the harmonic point pressure is going to be sampled in the frequency domain or in the spatial domain. An analytically derived expression for the radial pressure field in a plane z_1, due to a harmonic point pressure source in a parallel plane z_0, is

$$h(z, r) = -\frac{1}{2\pi}\left(j2\pi\frac{f}{c} - \frac{1}{d}\right)e^{jkd}, \tag{4.27}$$

where

$$z = z_1 - z_0, \qquad d = \sqrt{r^2 + z^2}, \qquad k = 2\pi(f/c). \tag{4.28}$$

The radial normal velocity field in the plane z_1 due to the field in z_0 can be derived. Since this function is radially symmetric, an analytical Hankel transform of $h(z, r)$ can be derived.

$$H(z, R) = \begin{cases} e^{j2\pi z\sqrt{(f/c)^2 - R^2}}, & |R| \leqslant f/c, \\ e^{-2\pi z\sqrt{R^2 - (f/c)^2}}, & |R| > f/c. \end{cases} \tag{4.29}$$

The variable R is the spatial frequency. And is defined as

$$R = \frac{f}{c} \sin \theta \tag{4.30}$$

where θ is the complex angle between a plane and the propagating plane wave. The angle is zero when the plane wave is normal to the plane.

Sampling equation (4.27) and then taking the discrete Hankel transform are referred to as spatially sampled convolution (SSC). Sampling directly equation (4.29) is called frequency sampled convolution (FSC). Theoretically these are equivalent, but there are significant differences due to the finite length discrete transform operations used. The SSC algorithm consists of the following steps:

1. Select a radius, r_d, greater than the source radius a over which correct field propagation results are desired. This determines the minimum transform extent as $T \geqslant r_d + a$. The radius has to be large enough to contain most of the energy in the field.

2. Select a spatial sampling rate, ψ, which exceeds the Nyquist requirements of the highest expected spatial frequency emitted from the source. This article proposes a sampling rate of $4 \times f/c$, as this ensures finely sampled output and the inclusion of any significant evanescent waves. The number of radial samples is then $N = \psi \times T$.

3. Using the above specified N and T, compute the specified samples of function $s(z_0, r)$. Call these complex values $s_d(i), i = 1, \ldots, N - 1$. Compute the DHT of these s_d values. Call the complex transform output values $S_d(m), m = 1 \ldots, N - 1$.

4. Again using the same definition of N and T, compute the specified samples of $h(z_1 - z_0, r)$, where $z_1 - z_0$ is the desired propagation distance. Call these values $h_d(i), i = 1, \ldots, N - 1$. Compute the DHT of these h_d values. Call these complex transform output values $H_d(m), m = 1, \ldots, N - 1$.

5. Compute the complex product $S_d(m) \times H_d(m), m = 1, \ldots, N - 1$. Now compute the inverse DHT of this product to obtain the desired complex field result. Call these normal velocity field results $u_d(z_1, i), i = 1, \ldots, N - 1$.

6. Now the u_d values can be examined as real and imaginary components, or by computing their magnitude and phase. Note the field samples describing $r_d < r < T$ contain "wraparound error," from the transform-based convolution.
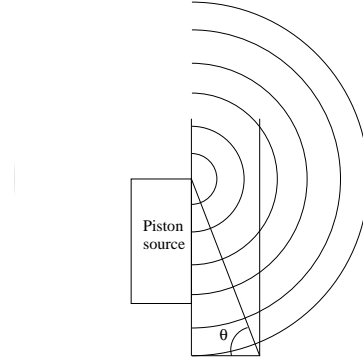
Figure 4.1: Geometry used for ray theory.

The FSC algorithm differs only in point 4. The FSC algorithm is then the same, except

4'. Using the previously determined N and T, directly sample $H(z_1 - z_0, R)$ to obtain $\hat{H}_d(m)m = 1, \ldots, N - 1$. Now use these values as the H_d values where used in the SSC algorithm.

Ray theory truncation for the FSC algorithm

The FSC algorithm described above can be greatly improved with a ray theory interpretation of the $h - H$ transform pair. Ray theory suggests that the lateral spatial frequency, η, of the field in the plane z_1 at point (r_i, z) is given by [5]

$$\eta_{max} = (f/c)\sin(\theta_{max}). \tag{4.31}$$

The angle θ_{max} is the most distant source contributing to the field at point (r_i, z). Huygen's principle is used to find this maximum lateral spatial frequency. The most distant source is chosen to the most distant point in the field. This is illustrated in figure 4.1. The new sampling rate can be applied to the SSC-algorithm by computing fewer samples of $h(z, r)$, or to the FSC-algorithm by truncating $H(z, R)$ so the maximum frequency is given by equation (4.31). The latter method is used in this implementation and it is referred to as the ray theory-updated FSC-algorithm (RFSC).

4.5.2 Inclusion of attenuation

When simulating the beam pattern in tissue, or when using pulsed beams, it is important to consider attenuation. In water the attenuation is so small that it can be neglected.

The attenuation is frequency-dependent. Higher frequencies are more attenuated than lower, because the lower ones have less energy. Attenuation for spherical or plane waves can be modeled by the expression

$$A = e^{-\alpha f^n \cdot d} \tag{4.32}$$

where A denotes the attenuation coefficient and d denotes the distance propagated in the medium. This expression is valid for weak attenuation, which means $\alpha / k \ll 1$. Typical values for n, are 1 for water and 2 for tissue. It should be noted that a new α has to be calculated for each occasion. The value of α is not very informative. Therefore it is more usual to use a parameter that describes the attenuation as x dB/cm/MHz (denoted by a_{dB}). This is an easy recalculation, and the resulting equation are

$$\alpha = \frac{a_{dB}}{20} \cdot \ln(10). \tag{4.33}$$

The attenuation-factor can be applied to both the point spread function h and the propagation function H. Here, it is applied to the propagation function

$$H_a(z, R) = H(z, R) \times e^{-\alpha \cdot \text{freq} \cdot 100 \cdot z_i nc / 10^6}. \tag{4.34}$$

4.6 A complete model

Realistic calculation of beam patterns requires consideration of diffraction, attenuation and nonlinear effects. Here it is assumed that the medium is homogeneous and isotropic. This means that the characteristics of the medium is independent of position and propagation direction. The model can be extended to multilayer, but this is not considered here.

Nonlinear effects are dealt with in chapter 5. An illustration of the process is given in figure 4.2. Figure 4.3 gives an impression of the field that is calculated. First, every harmonic is carried one step further. Then the nonlinear effects are calculated, and this is repeated until the desired distance has been reached.

It is important to make small steps, so the nonlinear effects are realistic. It will be shown later that it is also important to make the spatial extent of the field large enough.

The main stages of the simulation process are
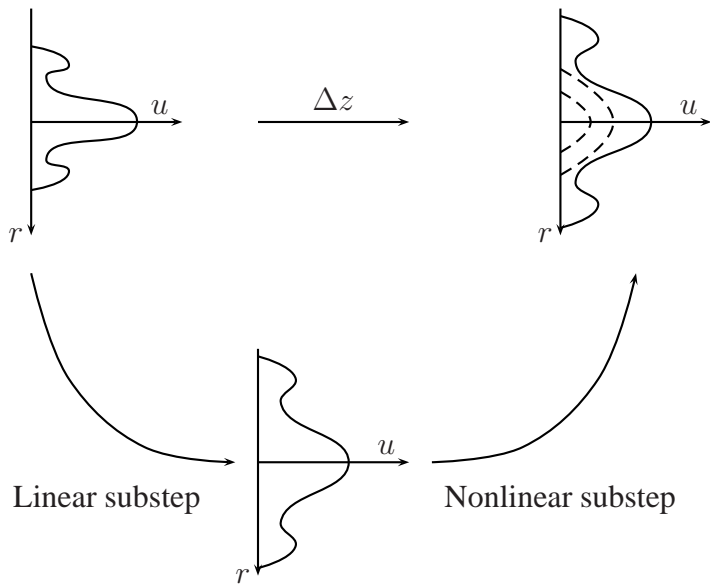
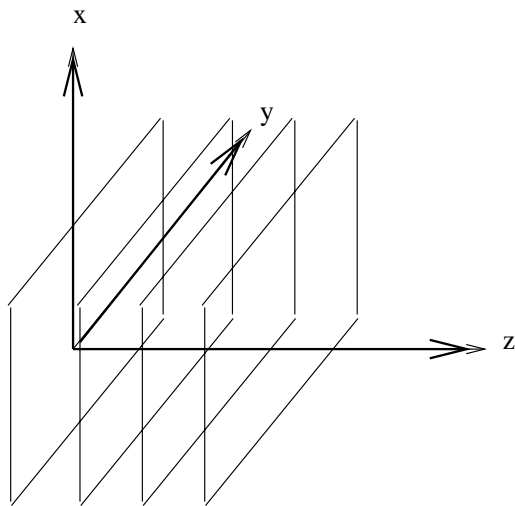Figure 4.2: One step of propagation.

Figure 4.3: Calculated fields.

1. Calculate the initial velocity of the transducer.

2. Calculate the propagation function for every harmonic with the desired propagation distance. Multiply with the attenuation coefficient, if desired.

3. Fourier transform the velocity matrices.

4. Multiply every propagation-matrix with every velocity-matrix for the harmonics. This multiplication is elementwise. This is the linear propagation step.

5. Inverse transform the velocity field.

6. Use the Burgers equation to account for nonlinear propagation.

7. Repeat step 3-6 until the desired distance is obtained.

Chapter 5

Nonlinear acoustics

Although nonlinear acoustics is an old field, it is mainly in the last 50 years it has been developed. Only in the last years it has been used in algorithms. The nonlinear wave equation was developed at the same time as the linear one, about 1750 [9]. For the first 200 years the progress was very slow. There are two main reasons for this. First, linear acoustics provided for sufficiently good modeling. This is due to the use of infinitesimal acoustics, but in the past decades it was realized that finite acoustics was needed. Second, the mathematical tools needed to handle nonlinearity were not developed. In the last decades is has been a lot of research and progress in the field of nonlinear acoustics.

5.1 Nonlinear effects in ultrasound

In the years since it was first proposed to use higher harmonics for ultrasound imaging in about 1980, several manufacturers of medical ultrasound have introduced harmonic imaging. This new feature gives better spatial resolution and higher contrast in images, which results in an improvement of diagnostic information.

Ultrasound in biomedical research has relied on convenient assumptions of infinitesimal acoustics. Some of the assumptions are not valid at most of the frequencies and intensities used today. Two questionable assumptions are:

1. The transmitted frequency is the only frequency in the medium.

2. Raising the source amplitude by a certain factor, raises the amplitude in the medium by that factor.

The reason why these assumptions are invalid is the existence of is nonlinear disturbance as the wave propagates. The invalidity of the first assumption was discovered with contrast agents. Contrast agents are small gas-filled

micro-bubbles. They are injected into the blood to enhance ultrasound images. It was assumed that only contrast agents produced energy at the second harmonic. It is claimed in [3] that it is not only contrast agents that produce higher harmonics. By taking advantage of this, better images can be achieved with harmonic imaging.

5.2 Nonlinear wave equation

The usually assumed linearity of acoustic pressure p with excess density ρ is only an approximation valid at infinitesimal amplitudes. A more accurate pressure density relationship is given by the series expansion

$$p = c_0^2 \rho + \frac{1}{2} \frac{c_0^2}{\rho_0} \left(\frac{B}{A} \right) \rho^2 + \dots \tag{5.1}$$

where c_0 is the infinitesimal sound speed constant (phase velocity), ρ_0 the static density and B/A is the second order parameter of nonlinearity. Retention of only the first term in equation (5.1) leads to linear acoustics. Keeping the first two terms enables one to deal with problems in nonlinear acoustics.

The derivation of the nonlinear wave equation is rather complicated, and it is beyond the scope of this text. A derivation can be found in [15], and the nonlinear wave equation is

$$\frac{\partial^2 \phi}{\partial t^2} - c_0^2 \triangle \phi = \frac{\partial}{\partial t} \left[(\nabla \phi)^2 + \frac{B/A}{2c_0^2} \left(\frac{\partial \phi}{\partial t} \right)^2 \right]. \tag{5.2}$$

where $\triangle$ denotes the Laplace operator and b is known at the absorption coefficient given by

$$b = \frac{1}{\rho_0} \left(\zeta + \frac{4}{3} \eta + \left(\frac{1}{c_v} - \frac{1}{c_p} \right) \kappa \right) \tag{5.3}$$

where ζ and η are shear and bulk viscosities, κ is the coefficient of thermal conductivity, and c_p and c_v are the specific heats.

A direct solution to this complex equation is probably not possible. A lot of approximations and simplifications have been made to be able to solve this equation. A variation of Burger' equation is used in this case.

5.3 Harmonic imaging

Harmonic imaging is a new method used to improve the quality of ultrasound images. The idea is to listen for sound bursts at twice the transmitted frequency. This has resulted in an improvement in spatial and contrast resolution.

Conventional ultrasound imaging has traditionally both transmitted and received the signal at the same frequency. The returned signal is less intense because it loses strength as propagates in tissue. Part of this energy is transmitted to higher frequencies. The returned signal consists of many frequencies.

Higher harmonics are generated by interactions with contrast agents and with tissue. Contrast agents are micro-bubbles injected into the blood for different purposes. These can be used to see the veins clearer. Two kinds of responses are generated from the bubbles. First, because of acoustic impedance, the pulse is reflected in the same way as from a bone. But the important response for harmonic imaging is the vibration generated by the shock from the pulse. This vibration generates a harmonic signal at twice the frequency of the original ultrasound pulse. Thus, when listening at twice the transmitted frequency, the strong signals are from the micro-bubbles. It is then possible to determine the location of the bubbles. Using bubbles is not the only way higher harmonics can be generated. It is important to note that a clean sine wave sent to the body will be distorted and changed by the properties of the tissue through which it travels. When tissue is compressed, the speed of sound generally increases in the compressed area. On the other hand, when the tissue is relaxed, the speed of sound decreases. Since a sound wave in the body is a pressure wave, this pressure wave exposes the body to different pressures. Since the speed of sound varies at different parts of the waveform, the clean sine wave is distorted. Different tissues distort the wave in different ways. For instance, fat tends distort the wave in this way much more significantly than muscle, liver or kidney tissue does.

Distortion of the sound wave is dependent on how far the wave has traveled. In the nearfield no harmonics have been generated. After a while harmonics are increasing. Then comes a period of unchanged harmonics. Finally the harmonics are attenuated and harmonics are decreasing and in the far field it is only an attenuated version of the fundamental frequency.

A comparison between fundamental and harmonic imaging is shown in figure 5.1. The harmonic image is shown to left and the fundamental image is shown to the right. It is an image of a liver. The harmonic image has more contrast and the texture is smoother, but the penetration is shallower compared to the fundamental image.

5.4 Harmonic generation

As stated previously in section 3.1.4, the speed of propagation is not constant. It depends on the frequency. At appreciable intensities, the velocity v at a point x on an acoustical waveform becomes
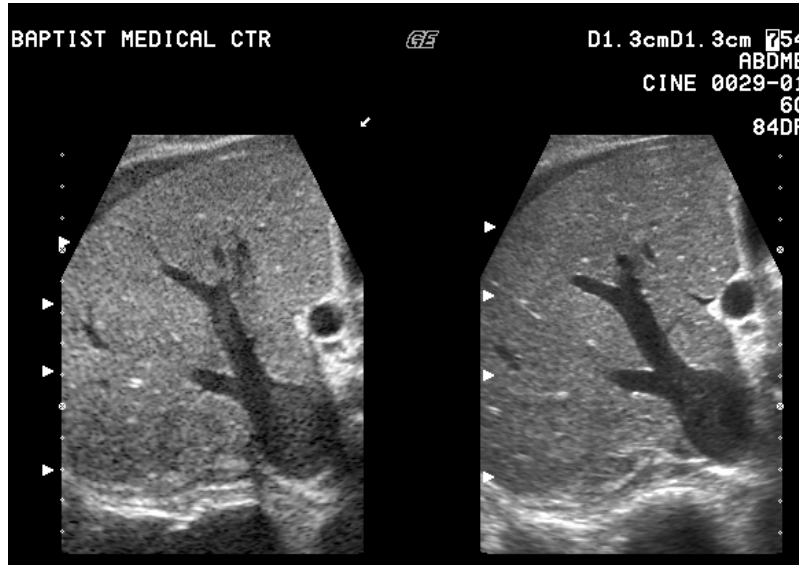
Figure 5.1: Comparison between fundamental and harmonic imaging.

$$v(x) = c_0 + \left(1 + \frac{1}{2}\frac{B}{A}\right)u(x) \tag{5.4}$$

where $u(x)$ is the particle velocity at that point. This means that the signal speed depends not only on the infinitesimal sound speed constant, but also on the local particle velocity, via the parameter of nonlinearity. Here it is seen that the velocity, $v(x)$, can be supersonic (greater that c_0). The distortion is cumulative and is illustrated in figure 5.2. Different stages of disturbance are shown. First, in part (a), the wave is a pure sinusoidal wave. As the wave is penetrating into the medium disturbance increases. At some time the waveform are approaching a shock wave. This is not desirable in medical ultrasound, because it can cause damage to tissue. Later, the higher harmonics are heavily attenuated and the waveform is the same as the excited waveform with smaller amplitude.

Distortion of the waveform in the time domain causes the generation of higher components in the frequency domain. Because these components are harmoniously related, it is called harmonic generation.

Figure 5.2 shows different stages of the disturbance. Five main stages are illustrated.

1. Near Field : No harmonics are being generated. The signal has not traveled enough to be distorted.
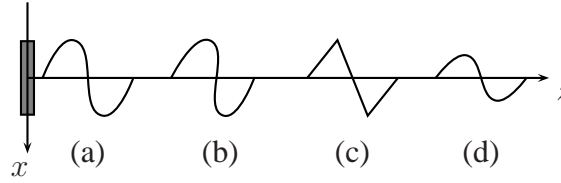
Figure 5.2: Different stages of disturbance as the wave propagates. (a) illustrates the excited waveform and in (b) is is slightly disturbed. (c) shows a sawtooth waveform and (d) is attenuated version of the original wave.

2. Near Mid Field : Harmonics are increasing. Harmonics are beginning to be produced as signal travels through tissue.

3. Mid Field : Harmonics are unchanging. Additional harmonics are generated and attenuated in equal proportion.

4. Far Mid Field : Harmonics are decreasing. Harmonics being attenuated faster than they are produced.

5. Far Field : Fundamental frequency only. Higher harmonics are attenuated and no new harmonics are being produced because the fundamental frequency has insufficient energy.

It is useful to think of this concept in terms of Fourier analysis. A fundamental result of this theory is that an arbitrary function, $f(x)$, can be decomposed into a sum of harmonic complex exponential functions

$$f(x) = \sum_{k=-\infty}^{\infty} c_k e^{jkx}.$$ (5.5)

The values c_k are called the spectral components of the function.

5.5 Harmonic simulation using Burgers equation

To derive the equation that models harmonic generation, a plane wave traveling in z-direction is considered. The change of particle velocity, U, can be approximated by a truncated power series in the form

$$U(z + \Delta z, t) = U(z, t) + \frac{\partial U}{\partial z} \Delta z. \tag{5.6}$$

The higher order terms have been neglected. This is valid if the step size (Δz) is chosen to be small. To obtain the differential change of particle velocity with respect to z, the following version of Burgers' equation can be used

$$\frac{\partial U}{\partial z} = \frac{\beta \omega_0}{c_0^2} U \frac{\partial U}{\partial \tau} + \Gamma \frac{\partial^2 U}{\partial \tau^2} \tag{5.7}$$

where c_0 is the infinitesimal bulk wave velocity (dispersion is neglected), β is the first nonlinear term in the pressure-density relation, and ω_0 is the angular frequency. $\Gamma = \beta U_0 \omega_0 / c_0^2 \alpha$ is a constant related to the thermo-viscous dissipation of the transmission medium, and $\tau = \omega_0 t - kz$, where k is the wavenumber. A continuous wave can be expressed as a Fourier series

$$U = \sum_{n=-\infty}^{\infty} u_n e^{jn(\omega_0 t - kz + \phi)} \tag{5.8}$$

where ϕ is an arbitrary phase constant, u_n is the real amplitude of the nth harmonics and $j = \sqrt{-1}$. A more compact form of the above equation is

$$U = \sum_{n=-\infty}^{\infty} \frac{1}{2} U_n e^{jn\tau} \tag{5.9}$$

where $U_n = u_n e^{in\phi}$ is half the complex amplitude. The derivation in [10] is missing the half factor as noted by [21]. Since the spectral decomposition extends from $-\infty$ to ∞, U_n is only half the amplitude. The derivation is correct, but there is an inconsistency in the notation. A property used to make simplifications later is $U_n = U_{-n}^*$, where * represents the complex conjugate. Now it is possible to find an expression for the differential change of the nth harmonic by substituting equation (5.9) into equation (5.7). With a rearrangement this can be expressed as

$$\frac{\partial U_n}{\partial z} = j \frac{\beta \omega_0}{4c_0^2} \sum_{m=-\infty}^{\infty} (n - m) U_{n-m} U_m - \frac{U_0}{\alpha} n^2 U_n. \tag{5.10}$$

The second term represents viscous losses having a quadratic dependency on frequency. The attenuation is included in the linear substep, so it is omitted in the further derivation.

To facilitate calculation by a computer, the summation term can be changed so that

$$\frac{\partial U_n}{\partial z} = j\frac{\beta\omega_0}{4c_0^2}\left(\sum_{k=1}^{n-1} kU_kU_{n-k} + \sum_{k=n}^{\infty} nU_kU_{k-n}^*\right) \qquad (5.11)$$

The infinite series has to be truncated and a finite number of harmonics, N, must be chosen.

The production of higher harmonics is a continuous process. The interaction between the different harmonics is given by the frequency domain solution the Burgers' equation. This equation updates the accretion and depletion of harmonics for each Δz step. The equation in article [6] is

$$u_n(z + \Delta z, i) = u_n'(z + \Delta z, i) + j\frac{\beta f\Delta z}{2c^2}\left(\sum_{k=1}^{n-1} ku_k'u_{n-k}' \right. \qquad (5.12)$$

$$\left. + \sum_{k=n}^{N} nu_k'u_{k-n}'^* \right), \quad n = 1, 2, \ldots, N \qquad (5.13)$$

where β is the nonlinear parameter and $u_n(z + \Delta z, i)$ denotes the nth term in an N term complex Fourier series. This series describes the temporal normal velocity waveform and the ith radial field sample in the plane $z + \Delta z$. In the bracket summation term the $u_k'(z + \Delta z, i)$ terms have been abbreviated by dropping the $(z + \Delta z, i)$ designation. The frequency has been chosen in the last equation by the relation $\omega = 2\pi \cdot f$.

Chapter 6

Implementation and verification

In this chapter the implementation and verification of the simulator is discussed. Some problems have to be overcome, and these are discussed first. The second part of this chapter consists of testing the simulator with real examples. It is shown to be in good agreement with measured values.

6.1 Implementation

There were many things to consider when implementing the simulator on a computer. The main challenge in this implementation was to reduce the memory usage. The program ran on a computer with large memory (reiknivel with 1 GB RAM). The execution time was also long, about 6-7 hours for the main simulations.

Some methods were not working correct in this program, and they are described in this first section. The phase front curvature was found not to be stable in this case, and a different form of attenuation was used. Finally a review of fast Fourier transform is presented.

6.1.1 Memory usage

The simulator requires a lot of computer memory to run. This is because the chosen simulation field has to be large enough to contain the most energy of the field. The main simulation is done in about 400 mm in both x and y-directions with a sampling rate of 0.308 mm. This implies a matrix of 1280 by 1280 samples of one harmonic. Since matlab operates only on double precision[1], this requires about 32 MB memory when the values are complex numbers. Such a matrix is needed for each harmonic. The propagation function is of the

---

[1]Requires 8 bytes to store a real number

exact same size. The propagation function could be calculated each time as needed, but this increases the computation time since this function is needed in each step of propagation. Saving it to disc once and then reading it into memory each time it was used, would also take too much time.

The goal was to reduce the memory usage as much as possible so as to be able to compute a pulsed wave. This has not been done in this thesis, but the program is ready to do this kind of simulation. The reduction of memory was achieved by using matrices declared used for different purposes at the different stages in the program. The listing is given in the appendix. The goal was to not exceed 128 MB, so the program could run on a parallel computer with 128 MB at the nodes. This has not been tested, but the program is close to this limit.

6.1.2 Phase front curvature

A correction term is proposed in [6]. This is a term that better accounts for wave or phase front curvature within the nonlinear substep. The Δz is replaced with $\Delta z/\cos(\theta[u_1(z,i)])$ and $u_n(z,i)$ is replaced by $u_n(z,i)/cos(\theta[u_1(z,i)])$, where

$$\theta[u_1(z,i)] = \frac{d}{dr}\left[\tan^{-1}\left(\frac{Im[u_1(z,r)]}{Re[u_1(z,r)]}\right)\right]_{r=r_i} \tag{6.1}$$

This equation assumes circular symmetry, but r could be replaced by x and y. It is a challenging equation to implement. It was tested to estimate the derivative by a bilinear interpolation in the radial direction. The noise from Fourier transform made the Re/Im factor rather arbitrary. When $\cos\theta$ was very small, artificial sources were introduced in the calculations. This is because division of a small number gives a large one. These numbers became new sources in the simulations. This method had to be left out of the calculations. The simulation results were shown to be very good in the test examples, so this will not restrict the model.

6.1.3 Attenuation

The attenuation was implemented as described in section 4.5.2. Article [5] proposes to include attenuation in the point spread function or in the propagation function. The latter is implemented by the equation

$$H_a(z,R) = H(z,R) \times e^{-\alpha f^n\{z/\cos[\sin^{-1}(Rc/f)]\}} \tag{6.2}$$

The expression in the curly brackets may look complicated, but it is just a calculation of the distance d in figure 6.1. The inner expression (in square

46
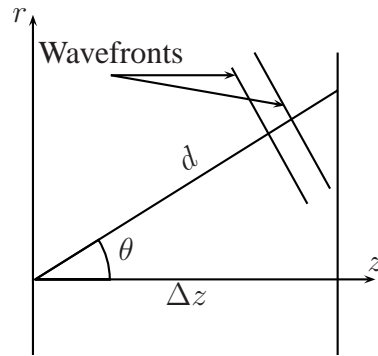
Figure 6.1: Travelling distance for waves.

brackets) is θ solved from equation (4.30). It is more correct to apply the attenuation in H instead of h, because the evanescent waves are neglected in h, and therefore they will not have any attenuation if h is used.

The implementation of this equation gave a larger attenuation when the radius was increasing. This could not be correct, and the approach described in section 4.5.2 was used.

6.1.4 Modification of the propagation function

Waag et al. [22] suggest an attenuation of the propagation function. This method was tested and in this case there was also a great attenuation at a larger radius. Grating lobes were suppressed, so this cosine taper window was not included in the model.

6.1.5 Fast Fourier transform

he main computation in the simulator is the Fourier transform. More than 90 % of the execution time is spent on transforming or inverse transforming. An efficient algorithm for implementing Fourier transform has been used. This is called fast Fourier transform. It is based on a so-called successive doubling method. Therefore it is important to use a power of two, or as many equal prime factors as possible, as the length of transform. Therefore the number $1280 = 2^8 \cdot 5$ has been chosen. Furthermore the selected number generates matrices small enough to satisfy the memory requirements.

The discrete Fourier transform (DFT) is defined as

$$X[k] = \sum_{n=0}^{N-1} x[n]W_N^{kn}, \qquad k = 0, 1, \ldots, N-1, \qquad (6.3)$$

where $W_N = e^{-j(2\pi/N)}$. The inverse transform is

$$x[n] = \frac{1}{N} \sum_{k=0}^{N-1} X[k]W_N^{-kn}, \qquad n = 0, 1, \ldots, N-1. \qquad (6.4)$$

Since these equations only differ in the sign of the exponent W_N and a scalar number, the computational procedures developed below applies to both with small modifications.

The crucial step is to use the complex conjugate symmetry and periodicity equations

$$W_N^{k[N-n]} = W_N^{-kn} = (W_N^{kn})^* \qquad (6.5)$$

$$W_N^{kn} = W_N^{k(n+N)} = W_N^{(k+N)n} \qquad (6.6)$$

The idea is to successively divide the DFT into smaller DFT computations. The decimation-in-time algorithm will be considered when N is an integer power of 2. By using equation 6.3 as a starting point and separating $x[n]$ into its even- and odd-numbered points, we get

$$X[k] = \sum_{n \text{ even}} x[n]W_N^{nk} + \sum_{n \text{ odd}} x[n]W_N^{nk} \qquad (6.7)$$

Changing variables $n = 2r$ when n is an even number and $n = 2r+1$ when n is an odd number leads to the equation

$$X[k] = \sum_{r=0}^{(N/2)-1} x[2r]W_N^{2rk} + \sum_{r=0}^{(N/2)-1} x[2r+1]W_N^{(2r+1)k} \qquad (6.8)$$

$$= \sum_{r=0}^{(N/2)-1} x[2r](W_N^2)^{rk} + W_N^k \sum_{r=0}^{(N/2)-1} x[2r+1](W_N^2)^{rk}. \qquad (6.9)$$

Since $W_N^2 = W_{N/2}$, the above equation can be simplified to

$$X[k] = \sum_{r=0}^{(N/2)-1} x[2r]W_{N/2}^{rk} + W_N^k \sum_{r=0}^{(N/2)-1} x[2r+1]W_{N/2}^{rk} \qquad (6.10)$$

$$= G[k] + W_N^k H[k]. \qquad (6.11)$$

G[k] and H[k] are two $(N/2)$-point DFT. It is required that these are computed with values $k = 0, 1, \ldots, N-1$. But since they are periodic in k with

period $N/2$, it is sufficient to compute when k is between 0 and $(N/2) - 1$. A more thorough derivation can be found in [16].

Another advantage is that the calculations can be done in-place. This means that it is not necessary to copy the data into another matrix.

6.2 Verification

It is important to check that the algorithm is correctly implemented. This check has been done by some examples. First, the linear substep was tested, then the full nonlinear program was tested.

6.2.1 Linear substep

To check the linear substep, the algorithm was configured using an example from article [5]. This was a 3 MHz circular piston with radius 10 mm. The acoustic medium is water with sound velocity $c = 1500$ m/s. In water the attenuation is so small that it can be neglected, as was done in this case. Radial extent of correctness was set to $r_d = 3$ cm, which led to a transform extent of $T = 4$ cm since the source had 1 cm radius. Sampling rate was proposed to be $\Psi = 4 \times f/c$ and this was 80 samples/cm in this case. The initial acoustic peak intensity was set to 0.1 W/cm^2. This algorithm requires the input field in normal velocity. A variation of the impedance equation gave the result

$$u_0 = \sqrt{\frac{I}{\rho \cdot c}} = \sqrt{\frac{0.1 \cdot \pi}{10^3 \cdot 1500 \cdot \pi (10^{-2})^2}} = 2.6 \text{cm/s} \qquad (6.12)$$

Christopher et. al. [5] have used the efficient discrete Hankel transform, (DHT). This method takes advantage of circular symmetry, and can only be used with circular symmetric transducers. Another method has been used here; the more general discrete Fourier transform. By using this method, any transducer geometries can be simulated, including the non-symmetric ones. The normal velocity field has been evaluated for two different propagation distances.

First, the propagation distance was $\Delta z = 0.5$ mm. The result is shown in figure 6.2(a). Compared to the article, there are some disturbances at distances greater than about 10 mm. This discrepancy can be explained by the fact that different approaches were used. This algorithm has disturbance from quantization of the circular transducer. This is illustrated in figure 6.3.

Points on a square grid with this sampling rate will not be completely circular. A comparison of the discrete Fourier transform versus the discrete Hankel
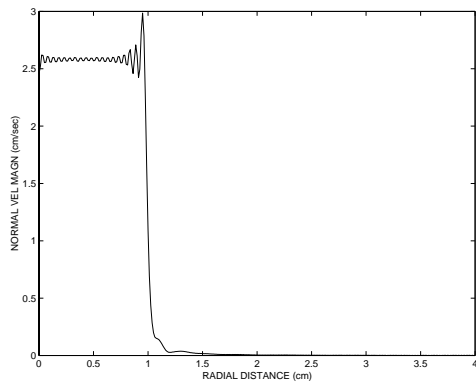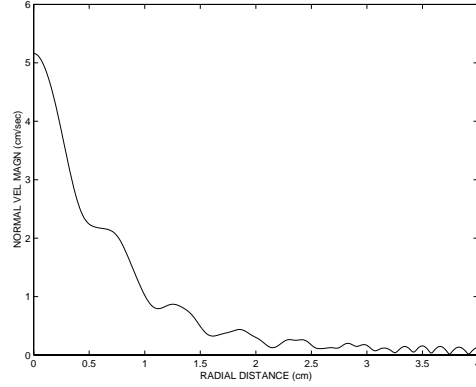
(a) $z = 0.5$ mm. (b) $z = 200$ mm.

Figure 6.2: Normal velocity field simulation from an unfocused piston transducer with radius 10 mm. Normal velocity is plotted along the radial distance, and the propagation distance is given under the figures.
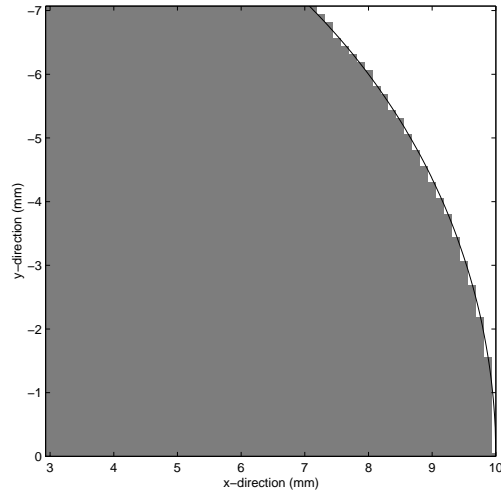
Figure 6.3: Discretization of 10 mm with sampling interval used in the linear example. It is shown in a 0 - $45°$ sector. All other cases are symmetric.

(a) Fourier transform   (b) Hankel transform
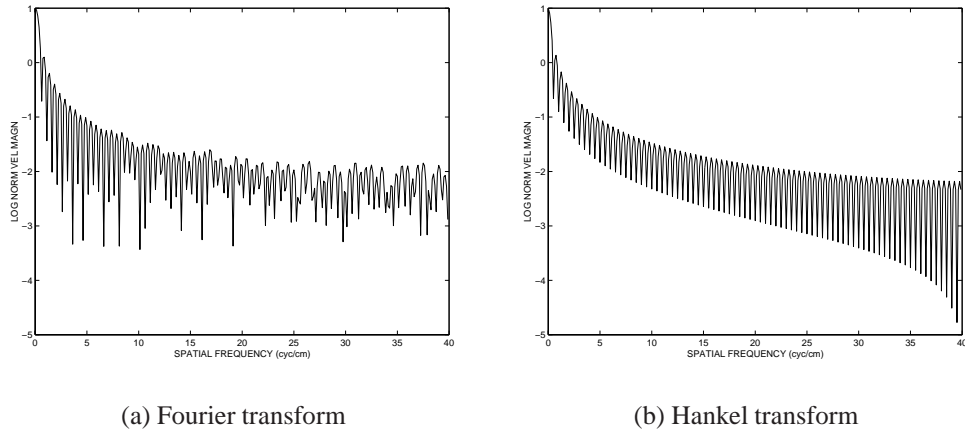
Figure 6.4: Comparison between Fourier and Hankel transform of the source.

transform used by Synnevåg , [19], is shown in figure 6.4.

The Fourier transform is calculated from the two-dimentional field with the piston in the center and the spatial extent as stated above. In this case the Fourier transform is circular symmetric, so it is shown along one axis. The Fourier transform has disturbances and these are especially evident at values greater than about 10 cyc/cm. Therefore one expects inaccurate results where the differences are greatest between the Fourier and the Hankel transform. This is verified in figure 6.5, where the field distributions are plotted in dB-scale. Different sampling intervals have been tested to see if this can improve the results. It is clear that the results are better as the sampling rate increases. However, there is not much to gain by changing from 80 to 160 samples/cm. When the sampling rate is increasing, the computation requires more memory and calculation time, so there is a trade-off. The disturbances are relative small, about -40 dB, so they are not contributing significantly to the results.

The second test is to propagate the field with $\Delta z = 20$ cm. This is shown in figure 6.2(b). In this case the results are worse, especially at large radius. The reason for this is that the propagation function has a smaller radius and therefore the quantization error is larger. This leads to more noise and the results are not very accurate. Propagation distances of this order are not important in this thesis, because the distance between the fields has to be small to model nonlinear effects.

51
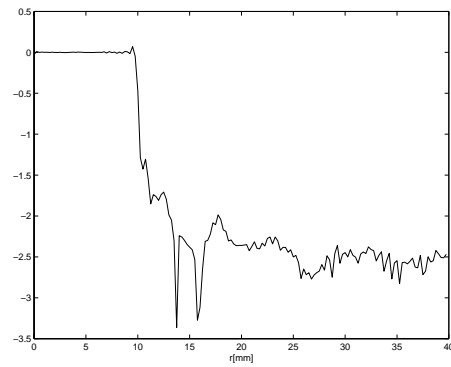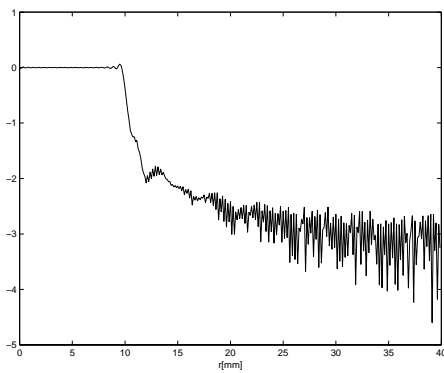
(a) $\Psi = 40$ samples/cm.

(b) $\Psi = 80$ samples/cm.
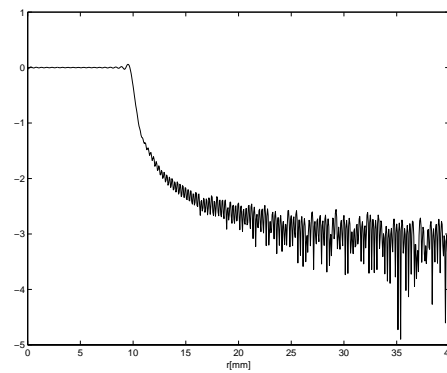
(c) $\Psi = 160$ samples/cm.

Figure 6.5: Logarithmic plot of propagation with $z = .5$ mm. with different sampling rates. Sampling rates are described under the figures.
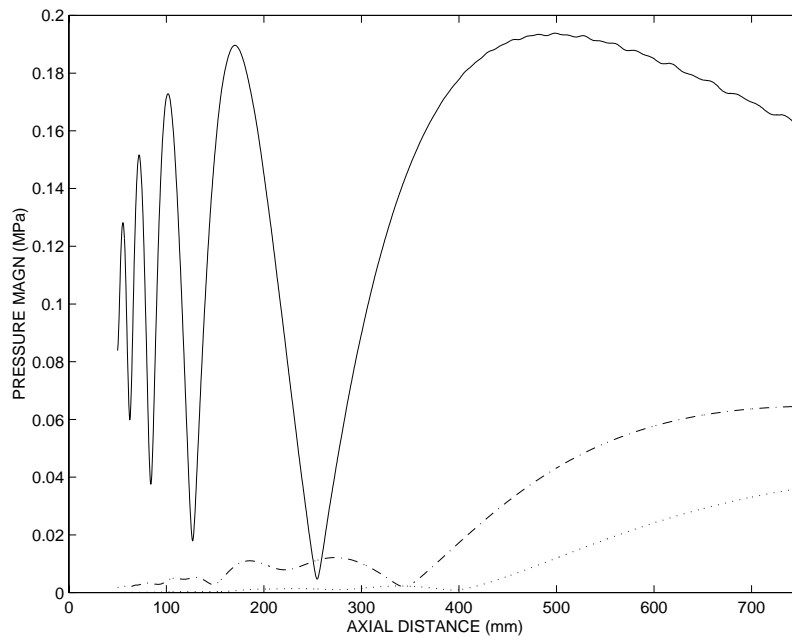
Figure 6.6: Multistep propagation with nonlinear modelling. The curves are the three first harmonics. Highest amplitude are the first, second in the middle and the lowest are the third.

6.2.2 Nonlinear substep

Nonlinear simulation is done by using Burgers equation. Since it is an approximation to the nonlinear wave equation, small steps have to be taken. Baker et al. have measured three harmonics (figure 1 in their article) in water and simulated it with the model based on a parabolic approximation to the nonlinear wave equation. The results are shown to have good accuracy. The general program used here produced the same results, and this is shown in figure 6.6.

GE Vingmed Ultrasound has measured two harmonics in a water tank. The program produced the results shown in figure 6.7. The simulation results are good. The signals are weak for the second harmonic, so it is difficult to model it accurately. But the results show good agreements with the measured values. The specification of this transducer is 2.3 MHz transmitted frequency. Elevation focus is 80 mm and azimuth focus is 90 mm. Azimuth aperture is 11/2 and elevation aperture is 17/2 and it is a dense array. The discrepancy of the first harmonic can be explained by a slightly wrong propagation velocity. Different initial pressures were tested because it was an unknown parameter. The shapes became almost equal with an initial pressure equal to 600 kPa. The simulated are slightly displaced, probably due to a not correct sound speed.
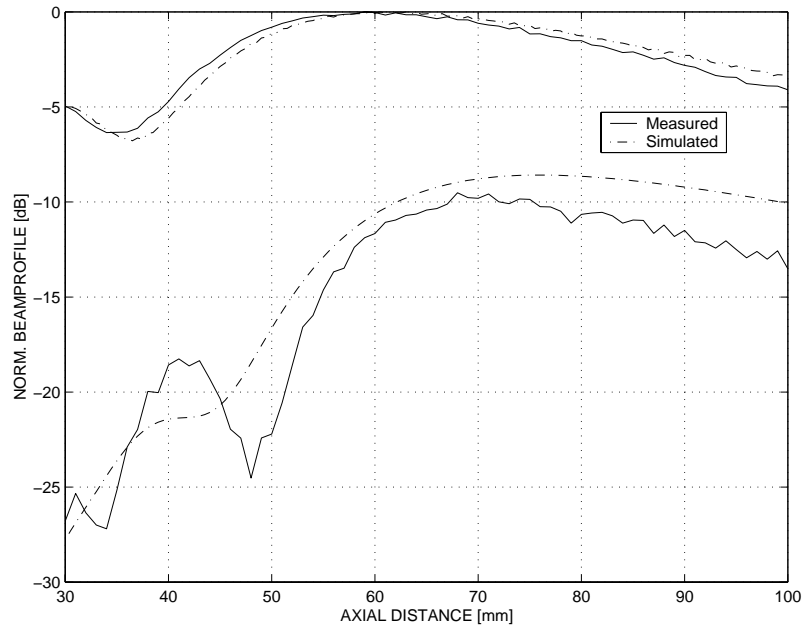
Figure 6.7: Simulation and measured values of a KK05 transducer. Measured an simulated first (highest amplitudes) and second harmonic.

6.2.3 Aliasing and grating lobes

A type of aliasing occurs when the field is not large enough in the spatial dimension compared to the depth of the field. In figure 6.8(a) an example is shown. As described earlier, the filtering process is not correct at the edges. When a large amount of energy are reaching the edges, it is aliased back and it looks like a reflection. The incorrect field at the edges are included in the figure. The simulation was done with the Vernier transducer shown in figure 6.8(b).

The angle of grating lobes can be calculated and in this case it is

$$\theta = \arcsin\left(\frac{1}{.622\lambda \cdot 3 \cdot .65}\right) \cdot \frac{180}{\pi} = 55.5°. \tag{6.13}$$

The factors 3 and 0.65 are used because the transmitted frequency is $0.65 \cdot 3$ MHz and .622 is the pitch[2].

Simulated values are found to be 55°. Experiments are done with focusing is set to 80 mm, and also with no focusing. Both cases show a small discrepancy (about .4°), and grating lobes are independent of focusing. The focusing does not move the grating lobes, they are only smoothed. An xz-plane is shown in figure 6.9.

---

[2]It is the distance between elements measured in wavelength
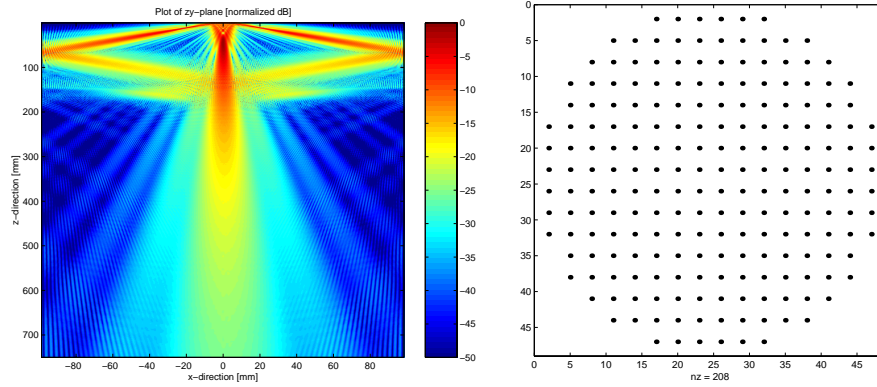
(a) Aliasing in the filtering process. (b) Transducer geometry.

Figure 6.8: Example of aliasing.

$$\theta = \arctan\left(\frac{44.2396}{30}\right) \cdot \frac{180}{\pi} = 55.9°$$ (6.14)

The simulator has been tested against Ultrasim and it shows good results. In figure 6.10 the same transducer is simulated with the two methods. The grating lobes are theoretically at 53.5°. With the simulator it is 54.2° and with Ultrasim it is 58.4°.
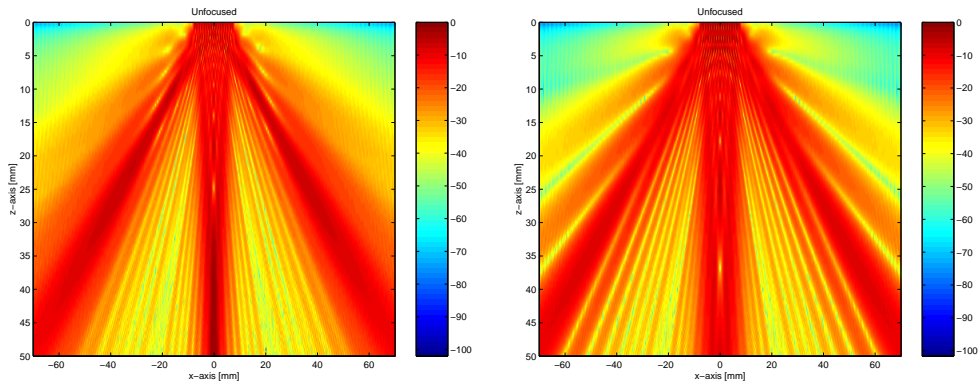
(a) Unfocused.

(b) Focus 80 mm.

Figure 6.9: Focused and unfocused transducer with grating lobes
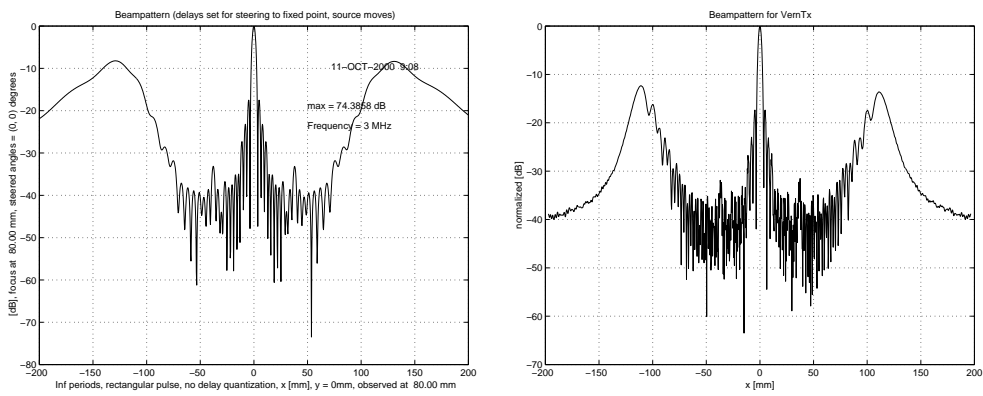
(a) Ultrasim.

(b) Angular spectrum simulator.

Figure 6.10: Vernier Rx transducer simulated at y = 0mm, z= 80mm

Chapter 7

Simulation

Since it is very expensive to produce a new transducer, a common way to test the performance is to simulate its behavior. In this chapter various layouts for a 2D transducer are simulated in water to see which strategy is best with nonlinear wave propagation. During the simulations a new phenomenon was discovered.

7.1 Response from a point scatterer

A first order approximation to calculate the pulse-echo response is used. It is based on the product of the continuous wave of the transmit and the receive responses, [17].

   The two-way response was calculated by assuming nonlinear propagation towards a point scatterer, and linear propagation back to the transducer. The linear propagation of the reflected beam is a valid assumption. The reason for this is that the reflected signal is so weak that it generates almost no distortion of this signal. Simulation of the receiving frequency is set to the double of the transmission frequency because it is the second harmonic that is interesting to study. This way to calculate the pulse-echo is valid in the focus of the beam. The examples have focus set to 80 mm. The transmission and receiving fields are multiplied and are in focus $z = 80$ mm.

   The field is propagated stepwise as shown in figure 4.3. The sampling rate in the z-direction is not necessarily an integer multiple of the focus. Therefore the closest field to the focus field[1] is chosen. Since the sampling frequency is high, the closest field is very near to the focus plane. In these examples the closest plane is 79.95 mm (=$205 \cdot .39$ mm).

---

[1]The field containing the focal point.
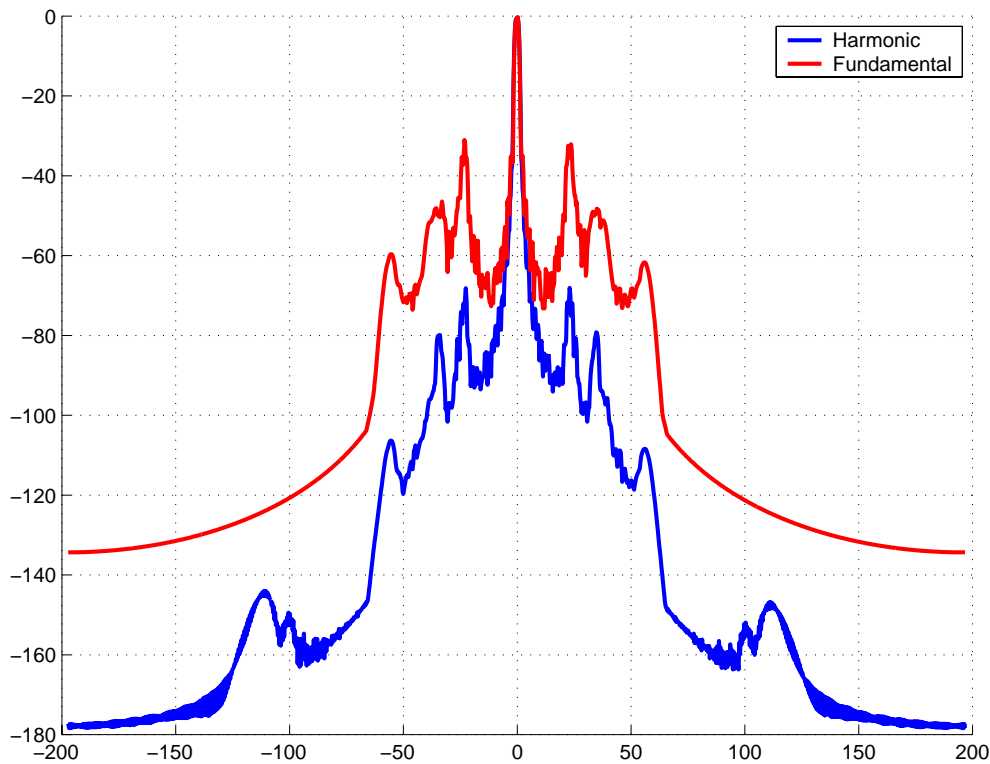
Figure 7.1: Comparison between fundamental and harmonic imaging.

	Transmit (Tx)	Receive (Rx)
1	Non-linear (f_0)	Linear ($2 \cdot f_0$)
2	Linear (f_0)	Linear (f_0)

Table 7.1: Methods for comparing harmonic and conventional response.

7.2   Conventional and harmonic imaging

A way to compare harmonic imaging with fundamental imaging is shown in table 7.1. The first case is simulated with nonlinear propagation and the second case is with conventional imaging. Linear propagation of the reflected wave is assumed also here. The receive and transmit field are multiplied and the two methods are compared in figure 7.1 by using a Vernier transducer. This is the worst case plot. This means that the largest value from all directions is chosen. From the figure it is seen that the sidelobes are lower when using harmonic imaging. This implies better image quality. The mainlobe width is also narrower, and this will be discussed later.

7.3   Nonlinear grating lobes

When using the nonlinear simulator, there was found a new grating lobe in the second harmonic. No reports of this lobe had been found in the existing literature. This new lobe is a kind of grating lobe and appears at half of the sinus to the angle of the fundamental.

It is known that fingers are created at the second harmonic. The first report on fingers is from 1973. It was experimentally found by Lockwood et al. [14], and later numerically by Tjøtta et al. [4]. Fingers appear at the second harmonic and they are the lobes that appear approximately when the fundamental is zero. This is shown in figure 7.6(b).

More examples of nonlinear grating lobes are shown later and the phenomenon is illustrated in figure 7.2. The scaling of the images is reduced to -25 dB in the first harmonic figure and -50 dB in the second harmonic. This has been done to make the grating lobes appear clearer since noise is removed. The lobes in the middle of the second harmonic are the nonlinear grating lobes. The phenomenon resembles fingers. The ratio between sine to the grating lobe and this nonlinear grating lobe is found to be .49 in this example. The other examples also show that this angle is approximately half of the fundamental.

7.4   Simulation of 2D sparse arrays

The main simulations are concentrated on a project, which objective was to lay the foundation of a real-time 3D imaging ultrasound system. Part of this project has been done at this University, specifically the construction of the sparse transducer for fundamental imaging. Transducer geometries that were used were developed in an Esprit project called "Real-Time 3D Ultrasound Imaging System with Advanced Transducer Arrays (NICE)". All the transducers considered in this section are evaluated in the project. Nonlinear propagation was not considered in the project.

When using harmonic imaging, the transmitted frequency has to be lowered because the double frequency has to be within the transducer bandwidth. This has not been done in these simulations because the grating lobes are moved to other locations and it is not possible to compare with conventional imaging.

This section presents the results of different geometries that are tested with nonlinear wave propagation. The second harmonic is studied with sparse arrays. Austeng et al. have tried to find the best possible sparse geometries for conventional imaging.

The specifications used here are the same as those used in the project. The center frequency is 3 MHz and 308 μm pitch (0.6 times the nominal

59
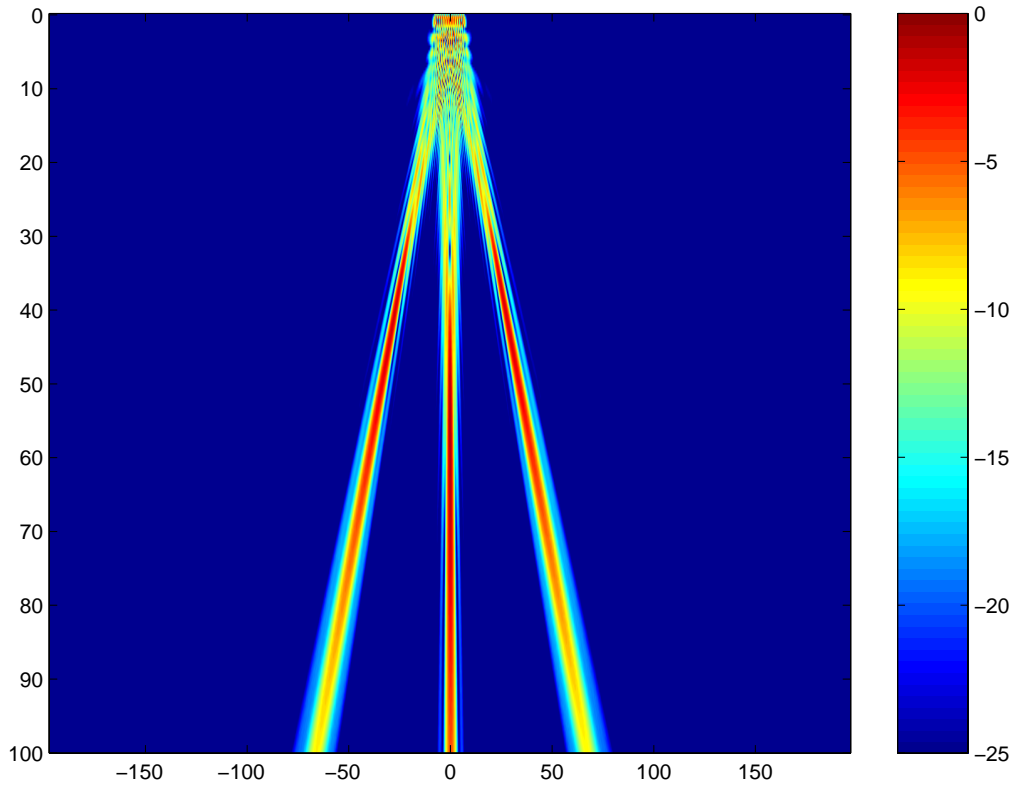
(a) First harmonic.
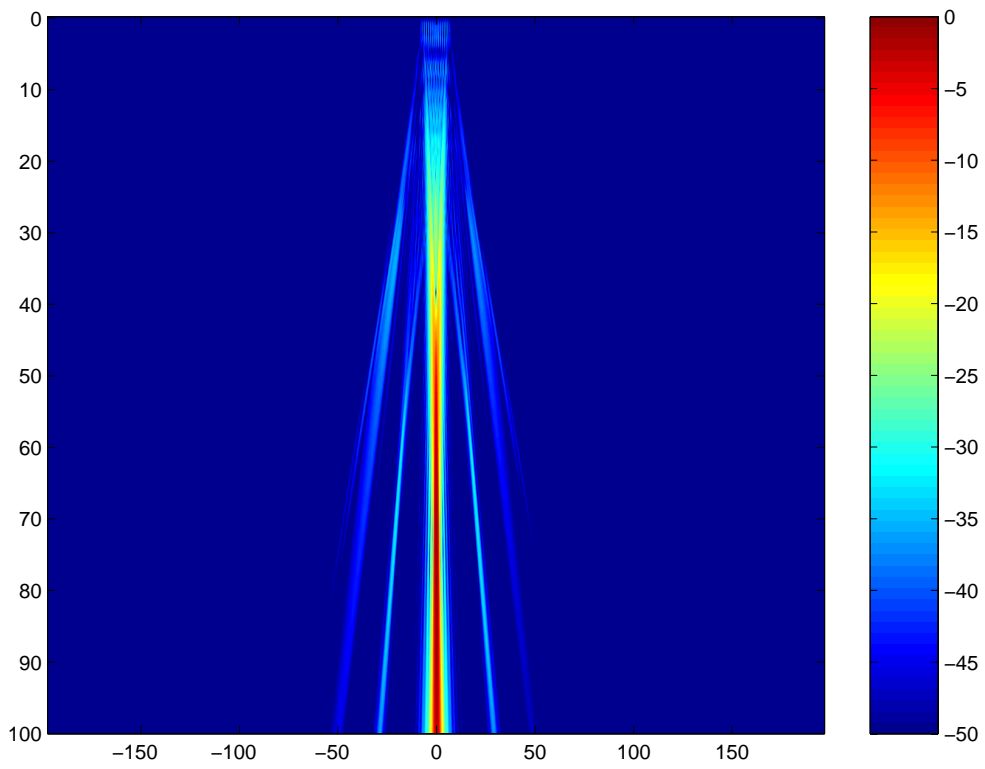
(b) Second harmonic.

Figure 7.2: Nonlinear grating lobes

wavelength) and the 2D array has 50x50 elements. No apodization is used, and the corner elements are removed to approximate a circular array. The parameters used in this simulation are summarized in table 7.2. Only the geometry is changed in the different simulations.

To prevent the formation of grating lobes and high sidelobes, it is necessary to have a maximum of 1/2 wavelength ($\lambda/2$) spacing between the elements. Using 2-D arrays, the number of elements could be as high as approximately 16000 elements, and it is impossible to fabricate such an array by using existing technology. Removing elements is a way of overcoming this problem. This process is called thinning. This will cause the probe to be undersampled.

A lot of considerations have to be taken when designing sparse arrays. First, there is an enormous amount of different layouts. The problem of selecting a relatively few number of 50x50 elements has an enormous number of solutions. It is impossible to go through every possible layout. Therefore, much effort has been made to develop the best possible sparse array. Some additional constraints can be set to further simplify the transducer design. An example of this is to reduce the number of overlapping elements between the transmission and the reception layouts. Then the same element is not used for transmission and reception. By using this separation, the elements are less complex and can be produced cheaper.

7.4.1 Vernier

The Vernier transducer is an example of a sparse periodic array. As described earlier, grating lobes appear when using sparse periodic arrays. It is shown that the number of elements can be reduced by a factor of six with little effect on the beam forming properties of the array, [13].

The idea of designing Vernier transducers is to use different layouts for transmission and reception. In this example, every second element is removed at transmission, and every third element is removed at reception. This is done because the grating lobes of transmission and reception will not be located in the same direction. The two-way response is calculated by multiplying transmission and reception fields. Grating lobes can be reduced if the other response is low in that direction. The optimal scenario would be to have a zero in the direction where the other geometry has a grating lobe. Then the grating lobe will be suppressed and the noise from this direction will be as small as possible. The layouts for this transducer at transmission and reception are shown in figure 7.3.

The simulation results for first and second harmonics are shown in figure 7.4. It is a cross-section of the focal plane $z = 80$ mm. It is worth noting that the second harmonic has a scaling down to -100 dB, while the funda-

Transducer:	
Beam type	CW
Radius	7.5 mm
Initial pressure	600 kPa
Frequency	3 MHz
Elevation focus	80 mm
Azimuth focus	80 mm
Wavelength	0.5133 mm
Medium:	
Velocity of sound	1540 m/s
Non-lin. parameter (beta)	3.5
Attenuation	0 dB/cm/MHz
Number of harmonics	4
Number of lateral samples	640
Density	1000 kg/m^3
Maximum depth	100 mm
Sampling in z	0.39 mm
Sampling in x and y	0.308 mm

Table 7.2: Simulation parameters.
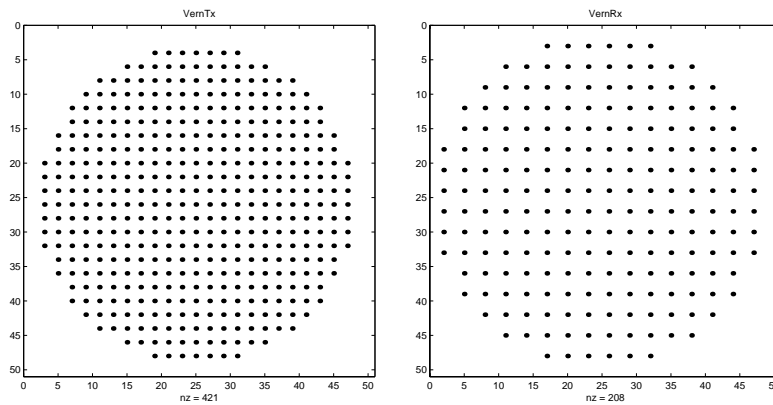
(a) VernTx. (b) VernRx.

Figure 7.3: Vernier transducer used at transmission (a) and reception (b).

mental shows values to -50 dB. The second harmonic has lower sidelobes than the fundamental. Grating lobes in the second harmonic are not as significant as in the fundamental, so better image quality is expected. Nonlinear grating lobes appear nearer the main lobe, so this has to be taken into consideration. The fingers should be close to a zero in the reception beam pattern.

In figure 7.5 the first and second harmonics are shown along the z-axis in the $y = 0$ plane. The generation of fingers is shown in the beam pattern of the second harmonic. The grating lobes are found in the outer areas of the x-axis. Closer to the mainlobe the nonlinear grating fingers can be found. A plot along the x-axis in focus is shown in figure 7.6. The upper figure shows the fingers clearly. The first and second harmonics are shown together. The lower figure is just a zooming of the center to show fingers and demonstrate that the mainlobe width of the second harmonic is narrower. This property, in addition to lower sidelobe levels, is the reason for using harmonic imaging.

The two-way response from a point scatterer is shown in figure 7.7(a). The grating lobes are now suppressed, and there are only some small fingers close to the mainlobe at level -80 dB. These small fingers is caused by the nonlinear grating lobes.

A conventional two-way response is shown in figure 7.7(b). The grating lobes appear and the mainlobe is larger.

An improved Vernier layout was suggested in the article [1] by changing the transmit layout. Now every third element is turned off and the two in between are used. This is shown in figure 7.7(c). The two-way response is shown in figure 7.7(d). Grating lobes appear in the same locations, but they are lowered somewhat to -90 dB. This layout is also more convenient to use in harmonic imaging because in this case more energy is transmitted into tissue. This is an advantage because the generation of higher harmonics requires more energy.

The conventional back-scattered image is shown in figure 7.8. The non-linear grating lobes are not appearing by using conventional imaging. The mainlobe width are also greater than by using harmonic imaging.

7.4.2 Diagonal

Periodicity by the diagonal axes have also been tested. The first of these is shown in figure 7.9. Every second element has been removed. The transmit array is not sparse along the diagonals and the element pitch along these axes is $\sqrt{2} \cdot 0.622\lambda$. The receive array is the same Vernier transducer with every third element removed.

Simulation in this case is given in figure 7.10. There are no grating lobes visible in this case, and the sidelobe level is small. Some disturbance can be seen along the diagonal axes.

63

Beampattern for VernTx, first harmonic

(a) First harmonic.

Beampattern for VernTx, second harmonic
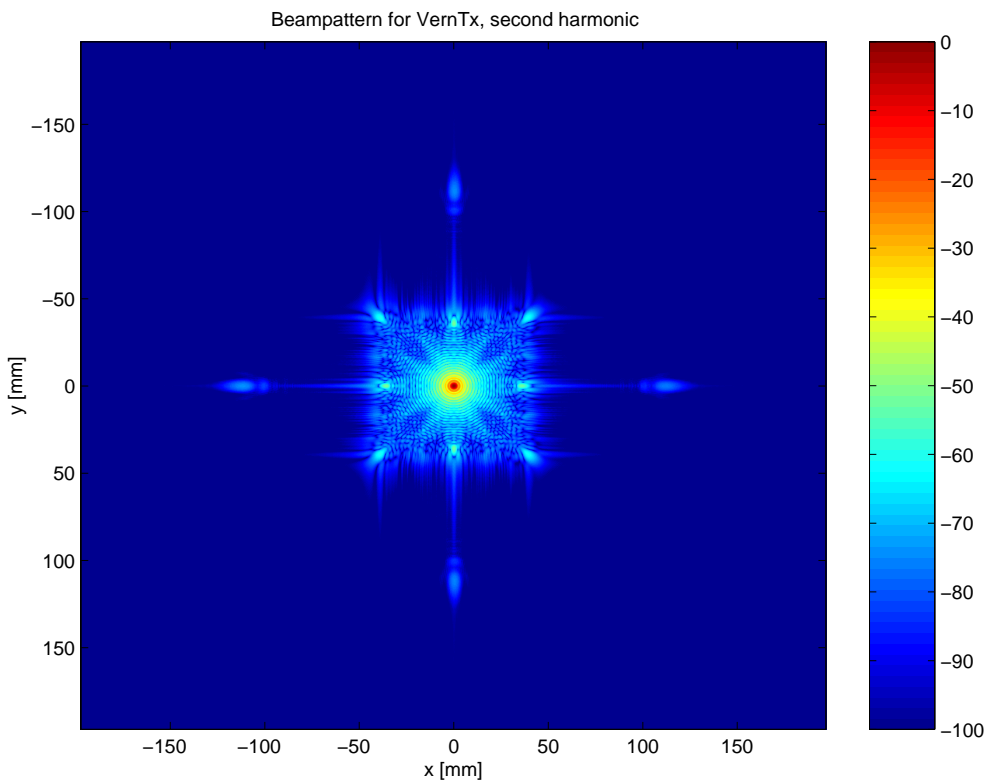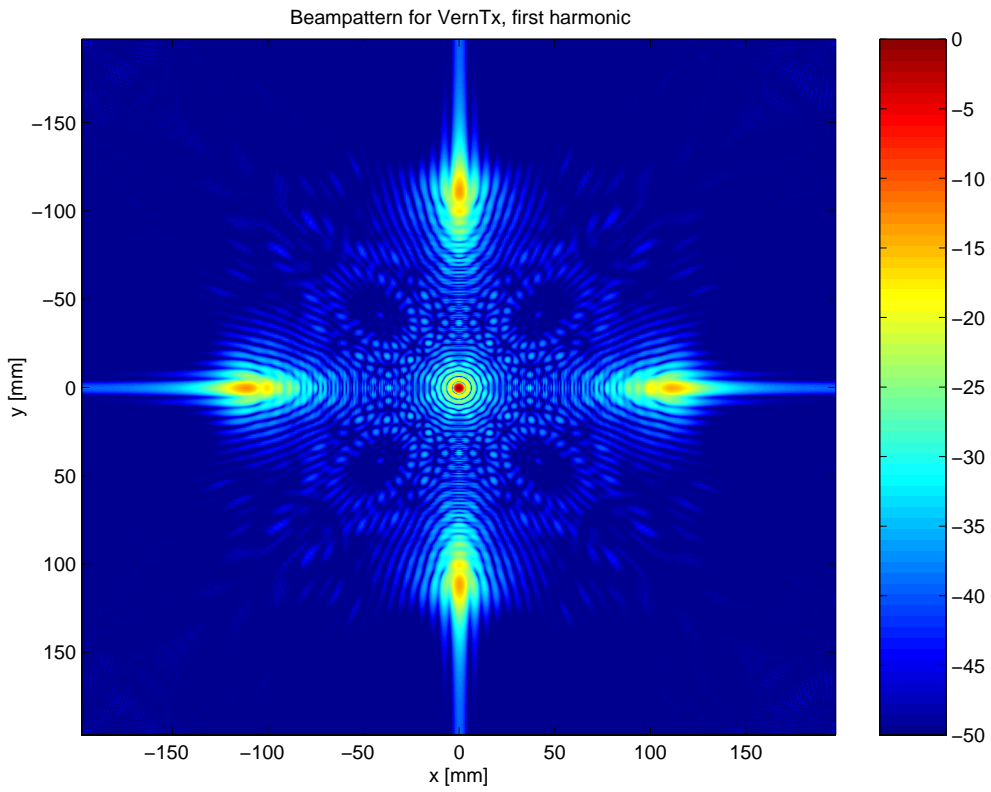
(b) Second Harmonic.

Figure 7.4: First and second harmonics in focal plane z=80 mm of a Vernier transducer.
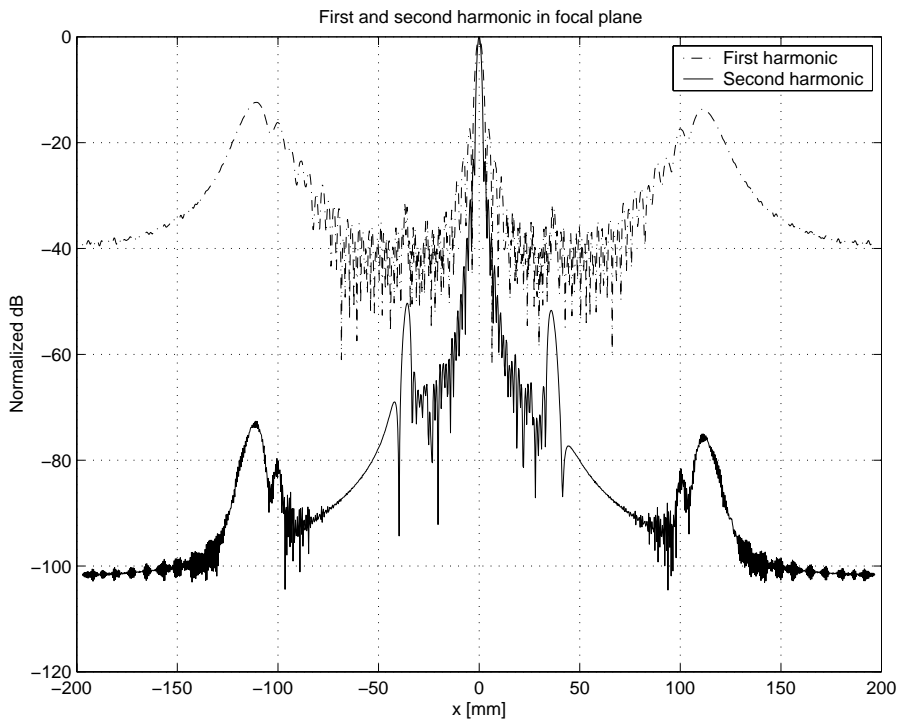
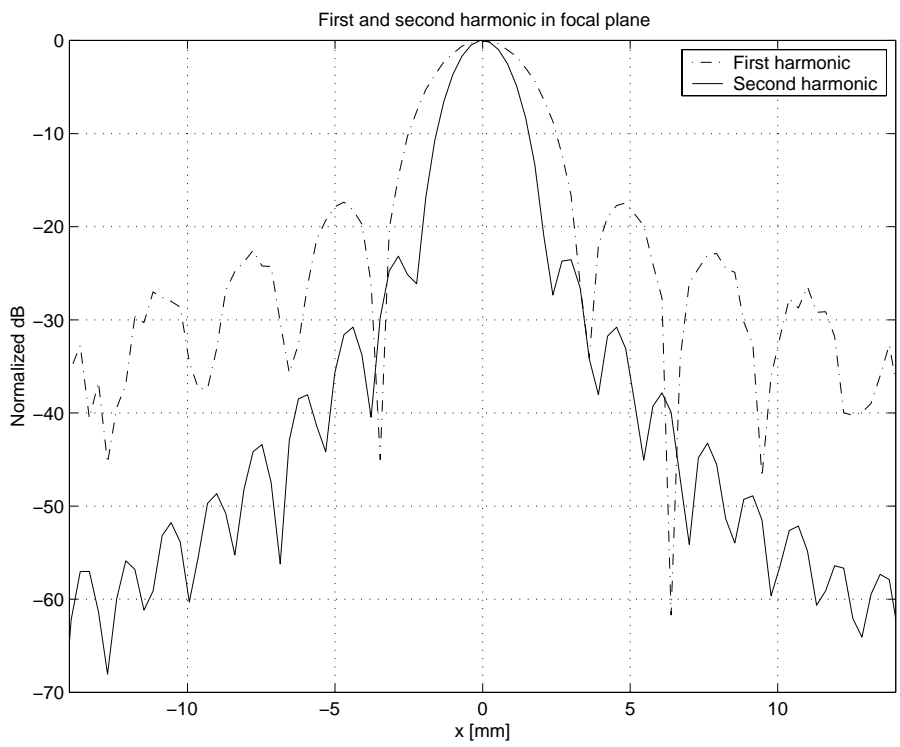64
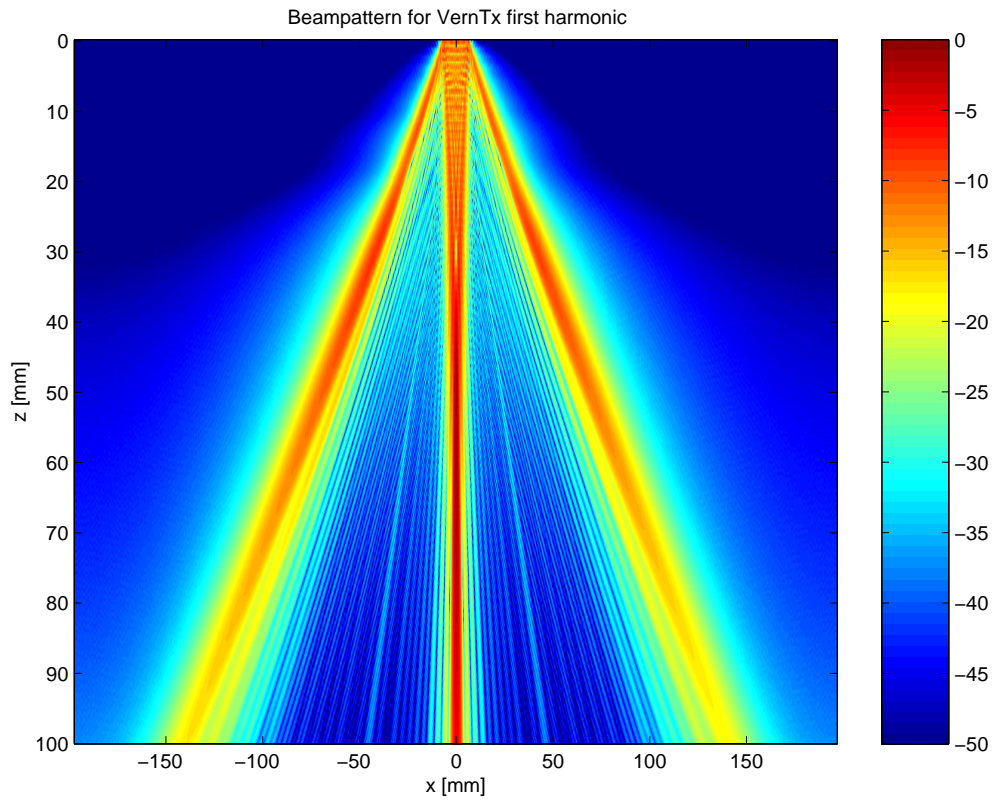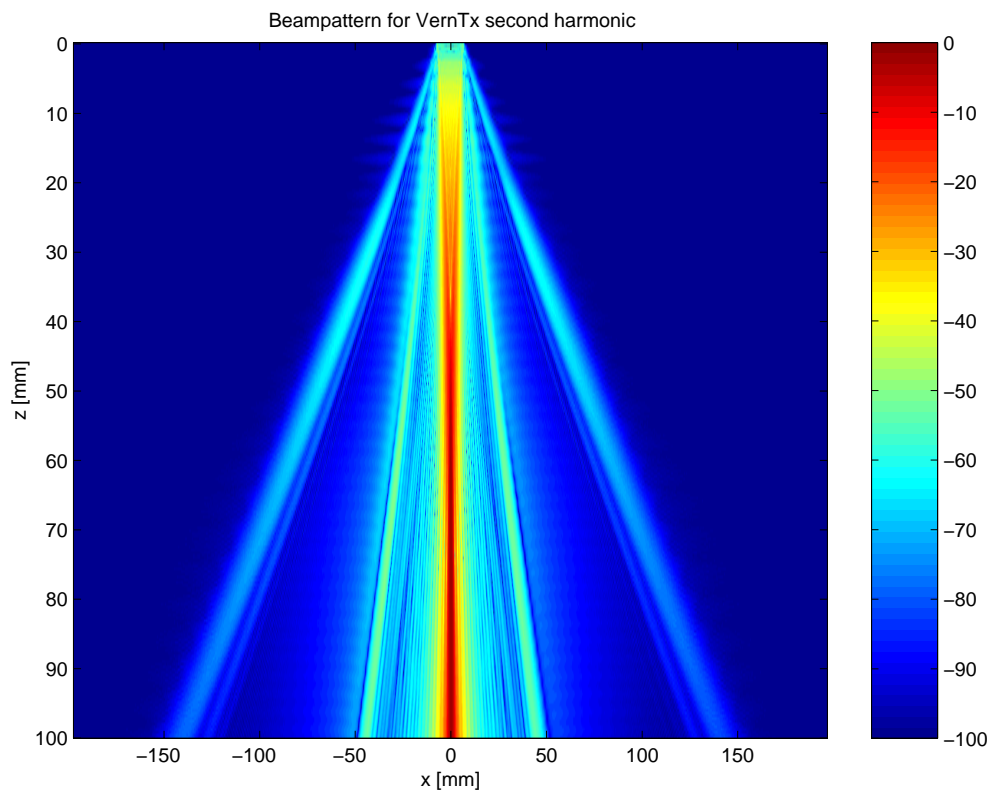
(a) First harmonic.

(b) Second harmonic.

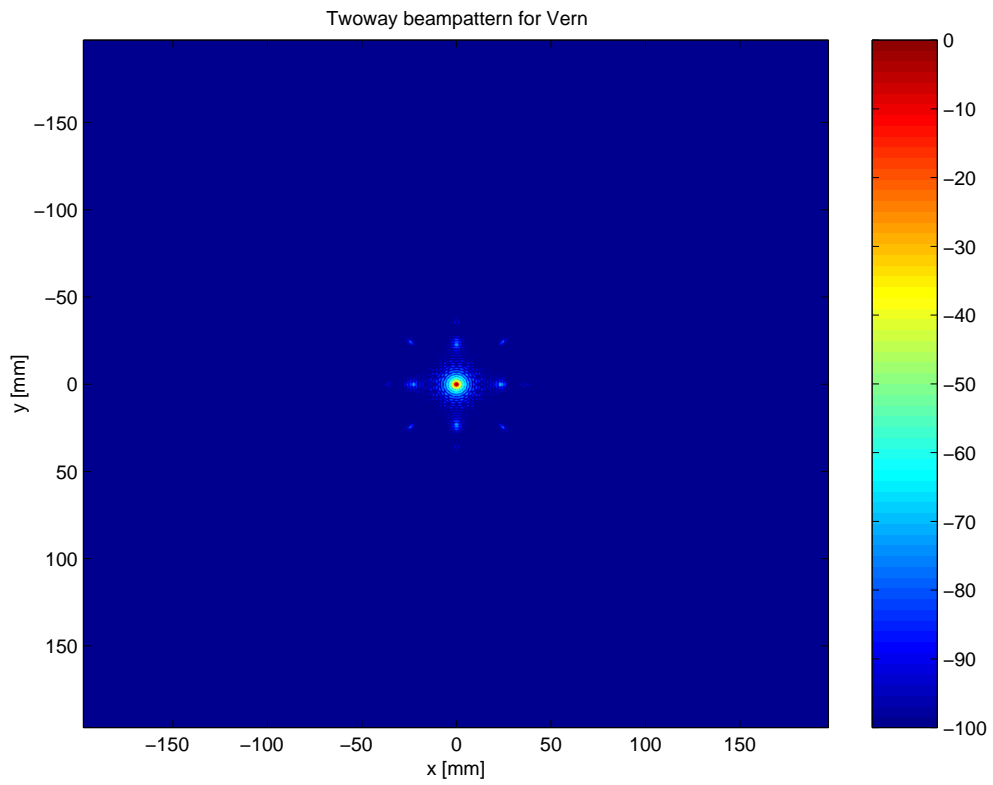Figure 7.5: First and second harmonics in $y = 0$ plane.

(a) Nonlinear grating lobes.

(b) Fingers.
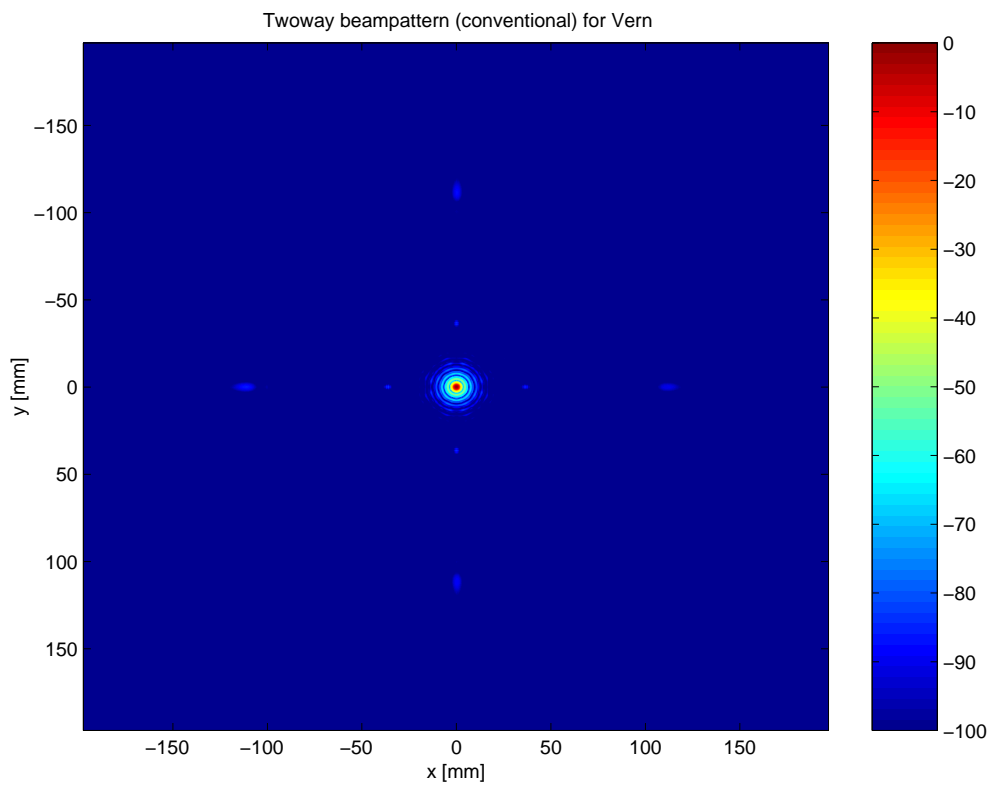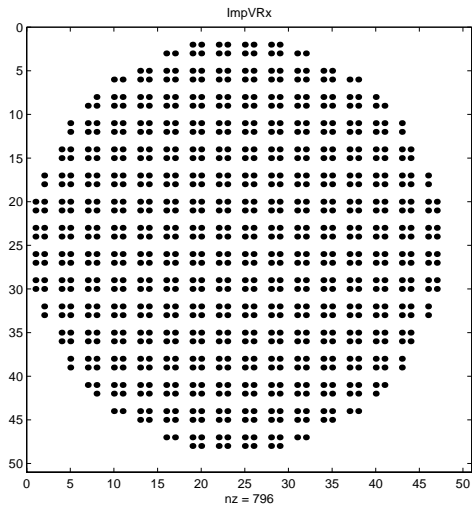
Figure 7.6: Zoomed version of plot (a).

(a) Harmonic two-way response from a point scatterer.

(b) Conventional two-way response from a point scatterer.

(c) ImpVRx.
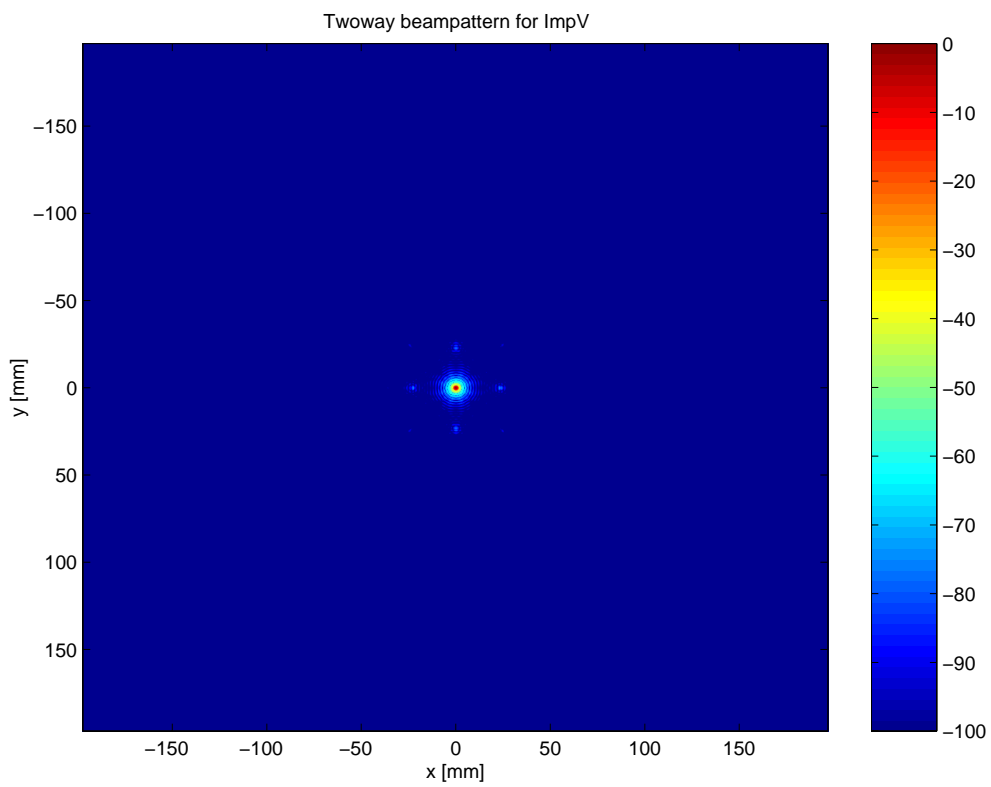
(d) Harmonic two-way response.

Figure 7.7: Improved Vernier.
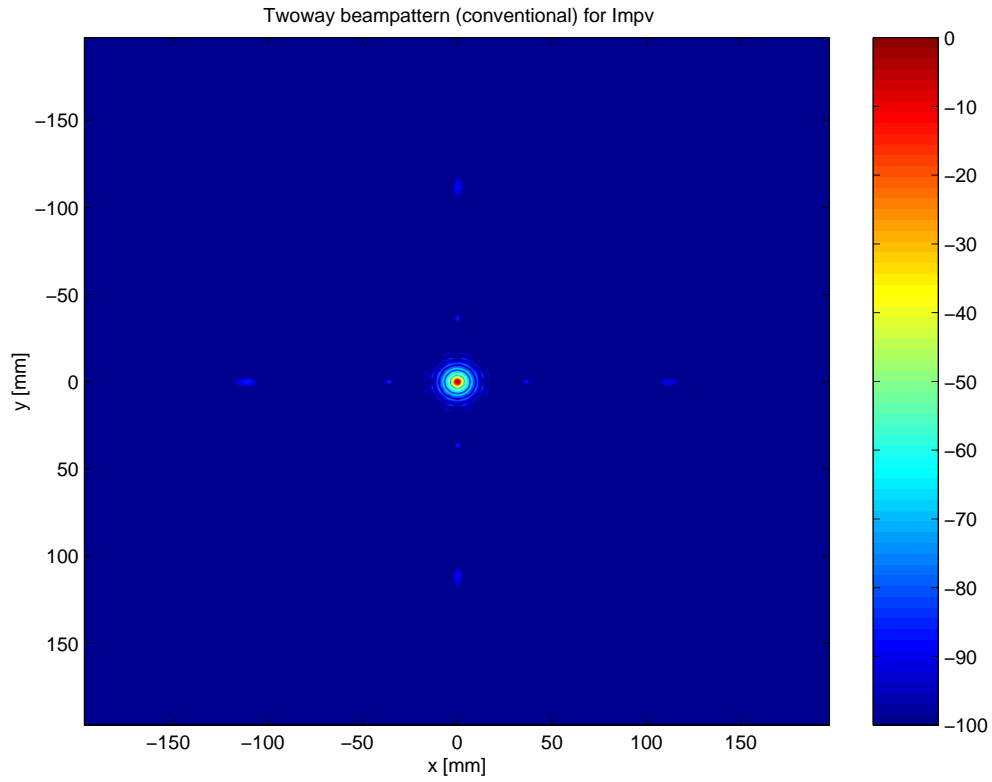
Figure 7.8: Conventional two-way response from a point scatterer.
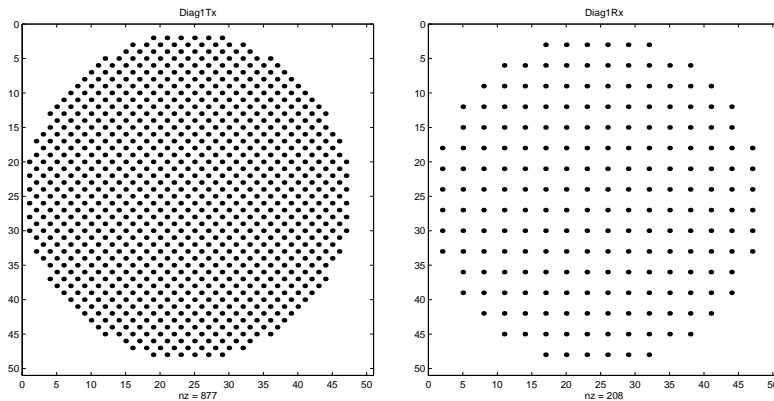
(a) Diag1Tx.

(b) Diag1Rx.

Figure 7.9: Diag first example.

(a) DiagTx.
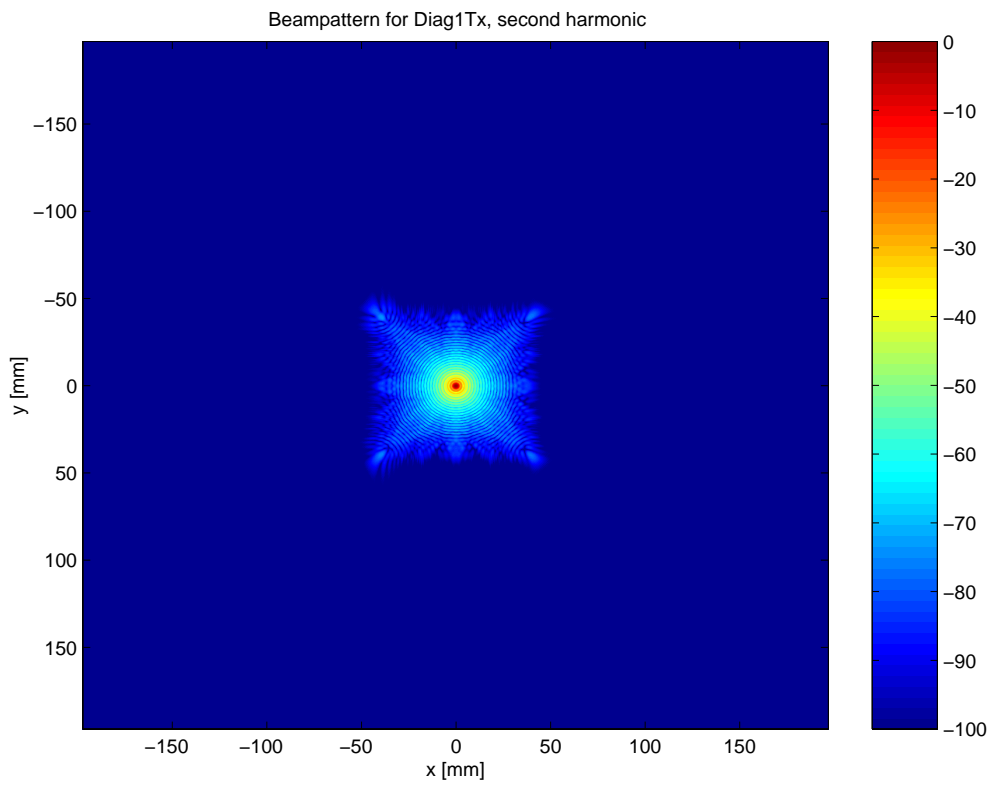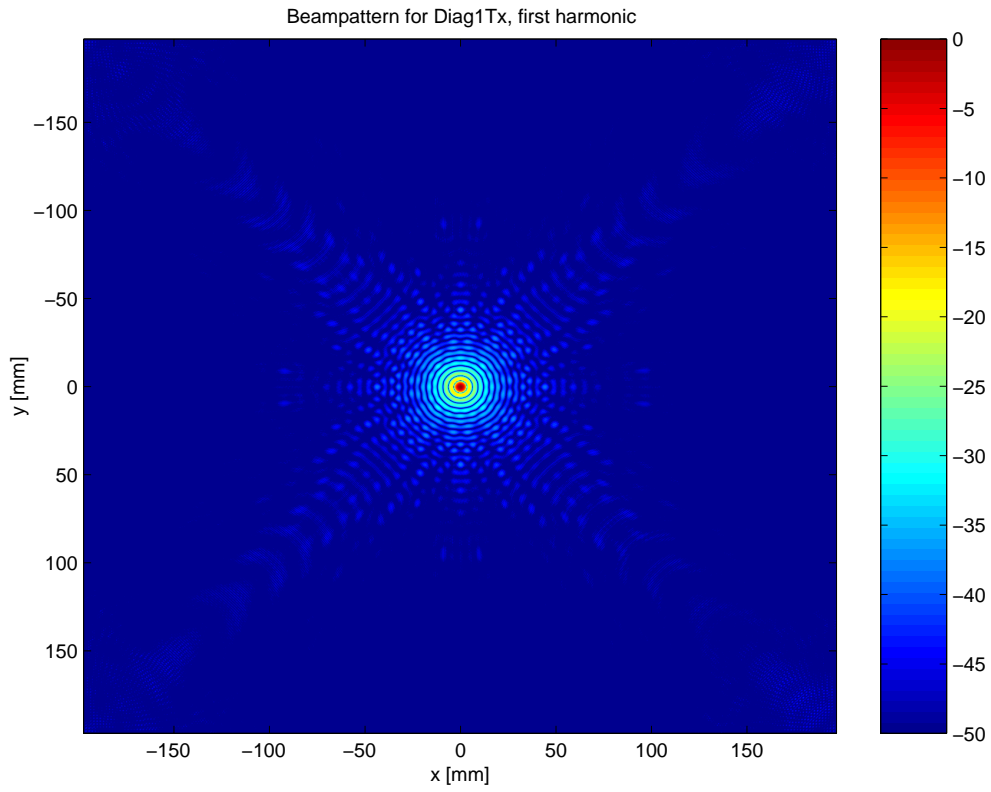
(b) Second harmonic.

Figure 7.10: First and second harmonics in focal plane $z = 80$ mm.

The beam patterns are shown in figure 7.11 and the two-way response is shown in figure 7.12(a). The beam pattern for the second harmonic appears to have a greater mainlobe, but this is not the case. Different scaling of the color bars makes the second harmonic look broader compared to the first.

A comparison between harmonic (figure 7.12(a)) and conventional (figure 7.12(b)) shows that harmonic has narrower mainlobe. The nonlinear grating lobes are also visible in the harmonic image.

Another way of combining diagonal symmetric periodic layouts is to use figure 7.9(a) as transmit array and figure 7.7(c) to receive the signal. This layout has more active elements.

Simulation in this case is given in figure 7.12.

The beam patterns in this case are almost equal to the previous example, so they are not repeated. Figure 7.11 can be considered again. The two-way response is shown in figure 7.13. Compared to the improved Vernier, this simulation has some more disturbance.

The conventional two-way image in figure 7.14 has grating lobes and larger mainlobe width compared to the harmonic image.

7.4.3 Axial dense-periodic transducer

Another way to consider the layouts is to let them be dense in one direction and sparse in the other. To suppress the grating lobes, the dense and sparse axes are changed in the receiving and transmitting part. This is illustrated in figure 7.15.

The simulation for these layouts is shown in figure 7.16. The same image scaling is used as in the previous example. It is seen that there are no grating lobes since it is along the x-axis and the sidelobe level is almost constant. The second harmonic has a smaller area with high sidelobes.

In this case the beam pattern in the $y = 0$ plane is given by figure 7.17. There are no fingers apparent in the second harmonic image.

The two-way response from a point scatterer is shown in figure 7.18(a). This shows a little more disturbance compared to the Vernier transducer. Both the fundamental and second harmonic have high sidelobe levels, in the same area. When one multiplies these to form the backscattered wave, it generates a high sidelobe level.

The conventional two-way response is shown in figure 7.18(b). Compared to the harmonic image, the mainlobe width is smaller and the sidelobe levels are generally lower.
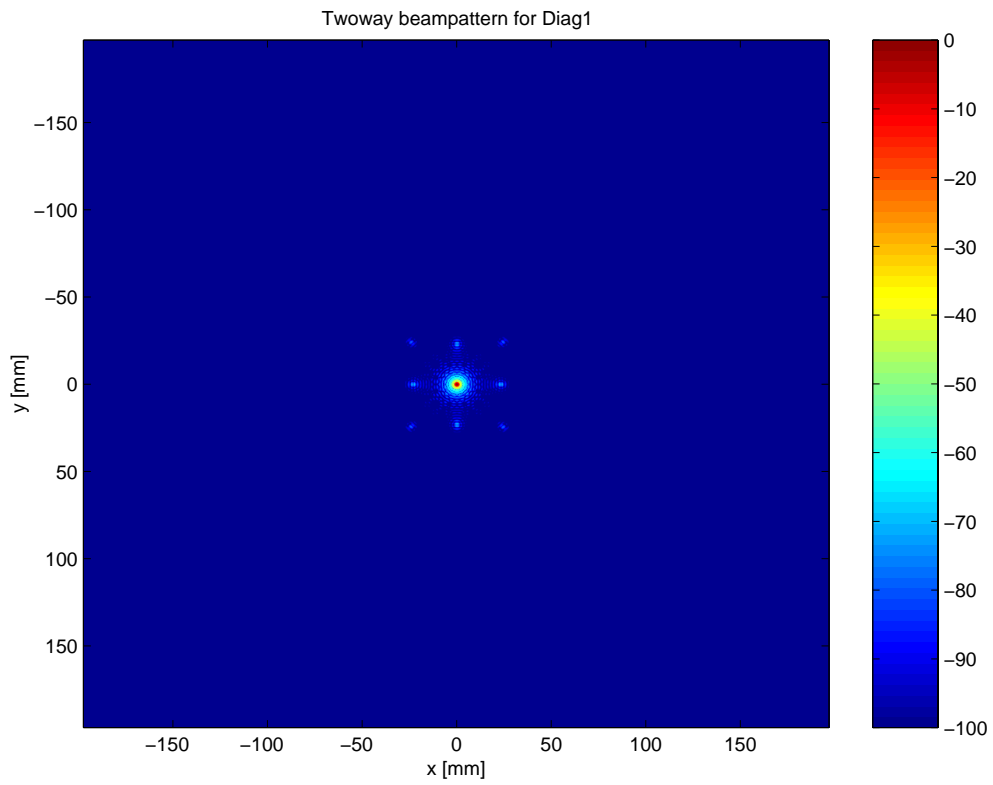
Beampattern for Diag1Tx first harmonic

(a) DiagTx.

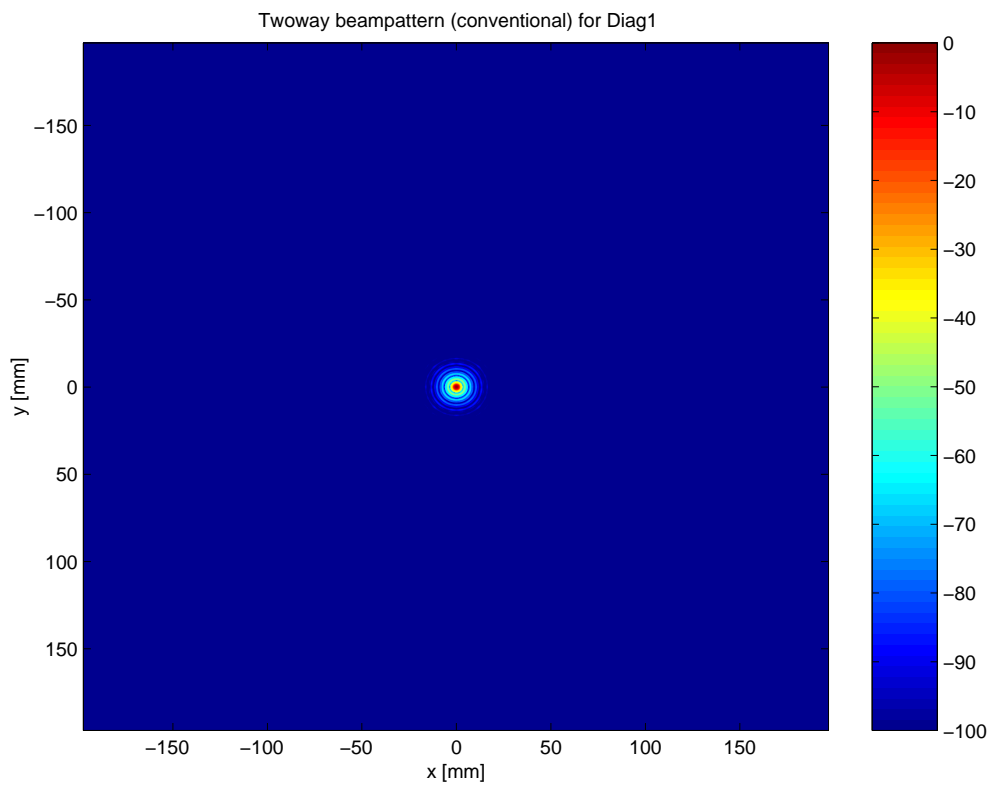Beampattern for Diag1Tx second harmonic
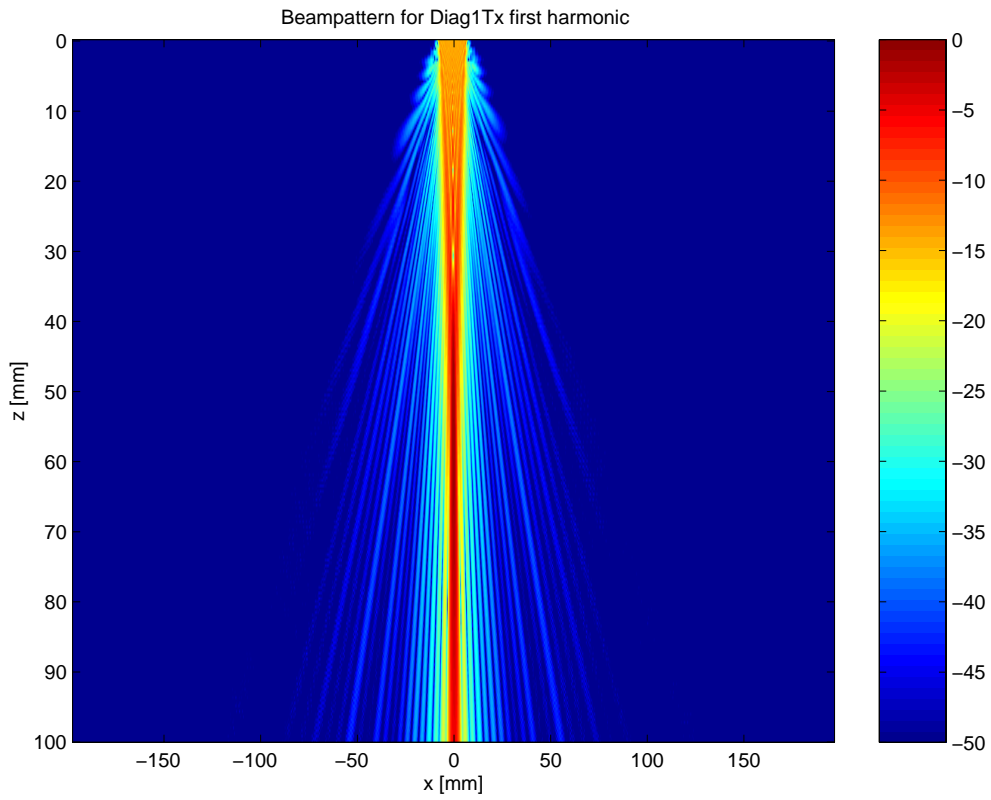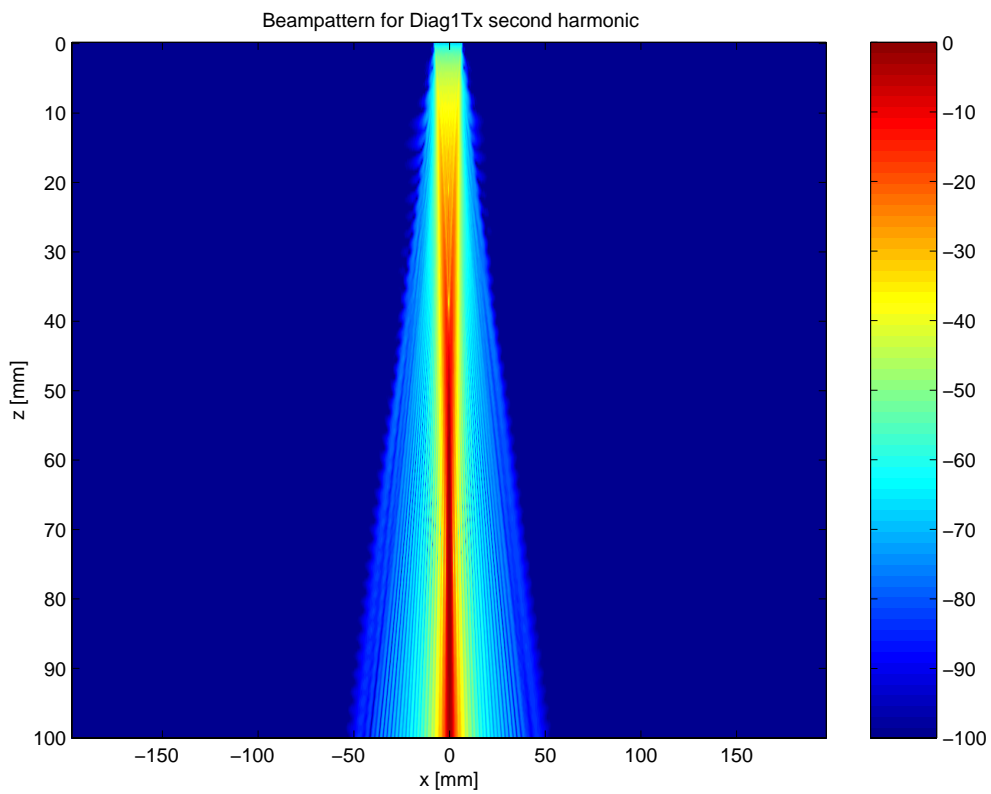
(b) Second harmonic.

Figure 7.11: First and second harmonics in focal plane $z = 80$ mm.

(a) Harmonic two-way response from a point scatterer.

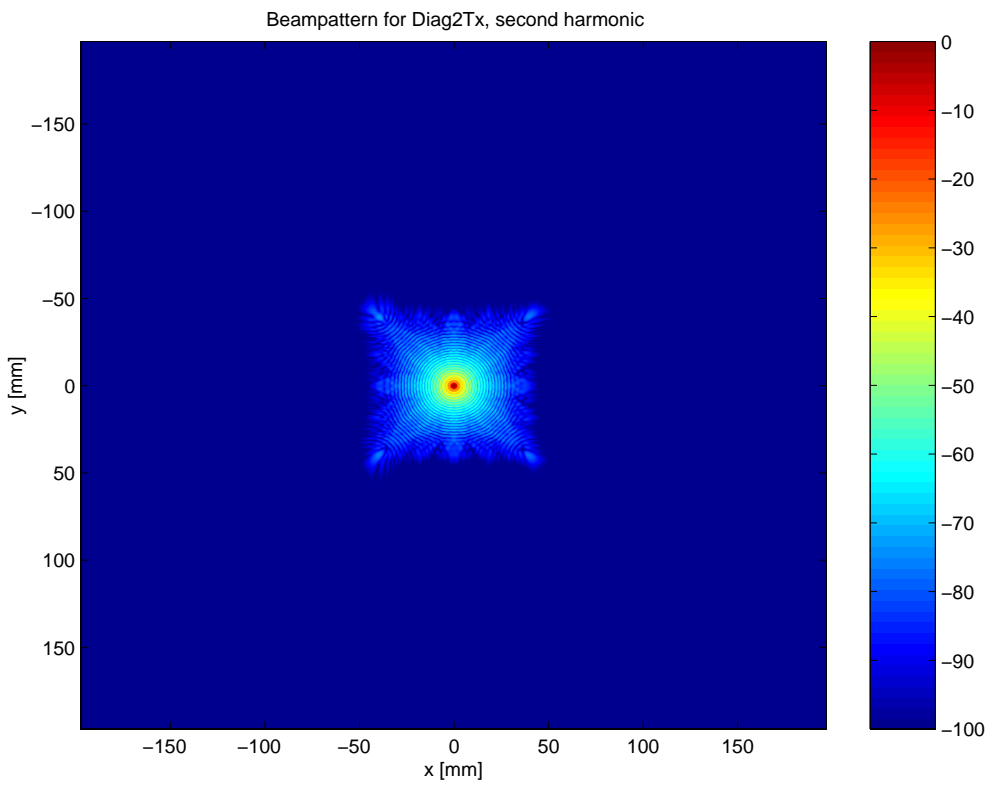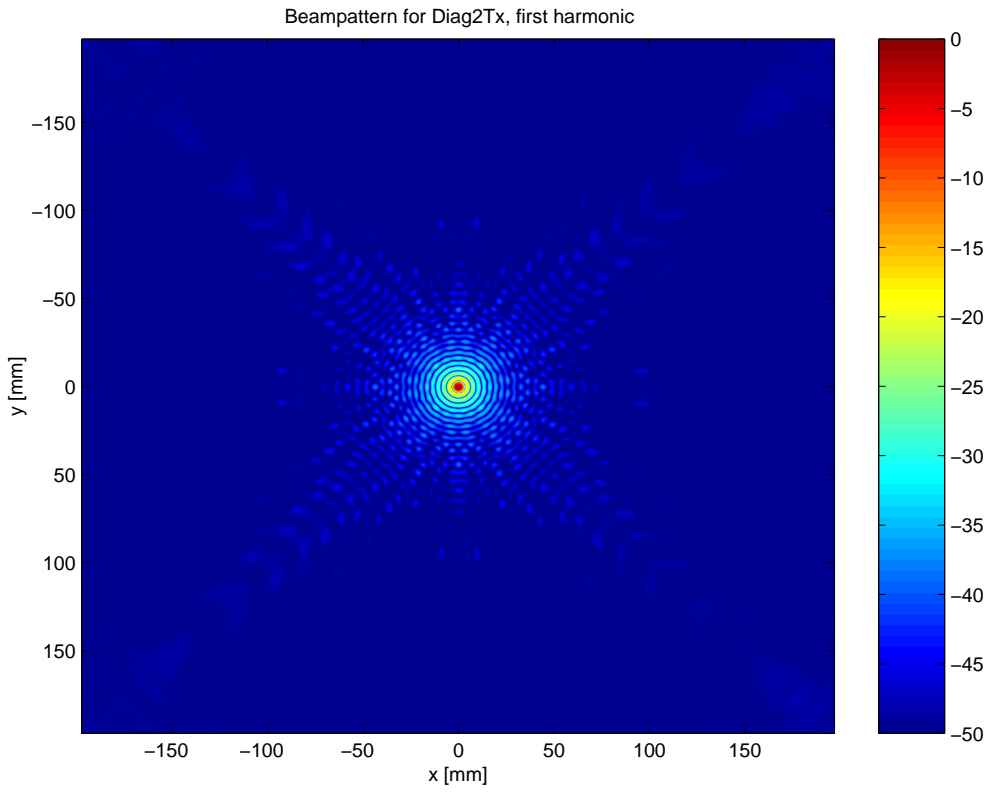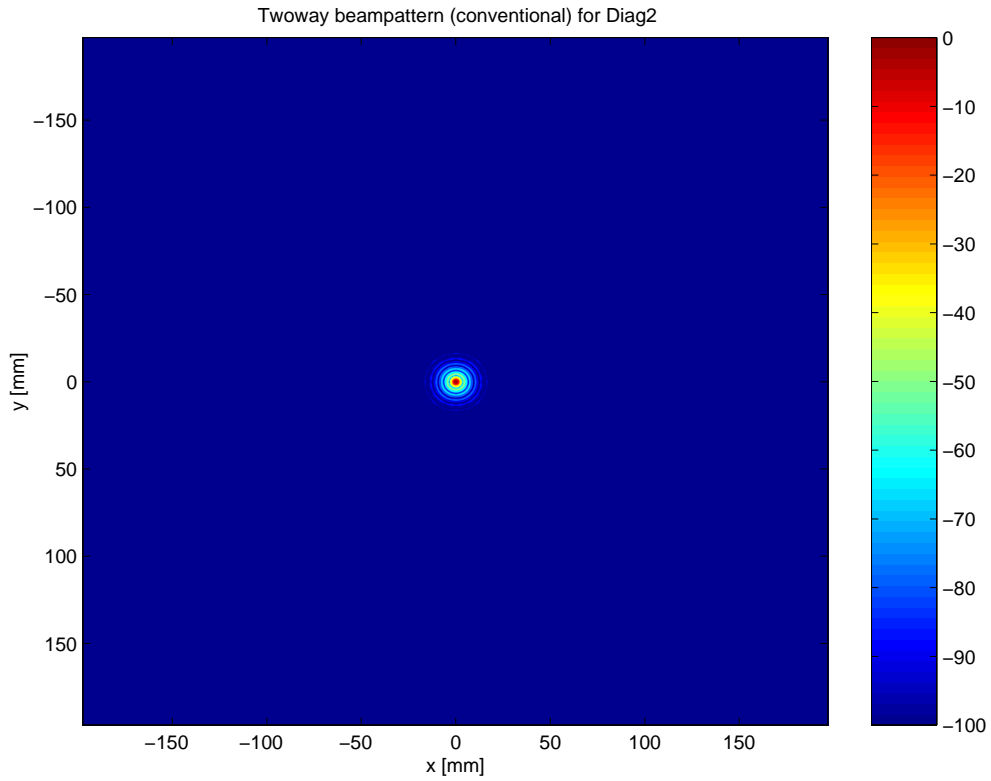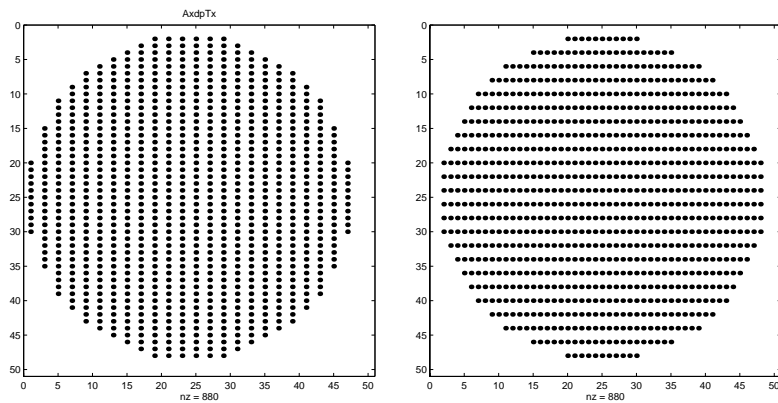(b) Conventional two-way response from a point scatterer.

Beampattern for Diag2Tx, first harmonic

(c) DiagTx.

Beampattern for Diag2Tx, second harmonic

(d) Second harmonic.

Figure 7.12: First and second harmonics in focal plane $z = 80$ mm.
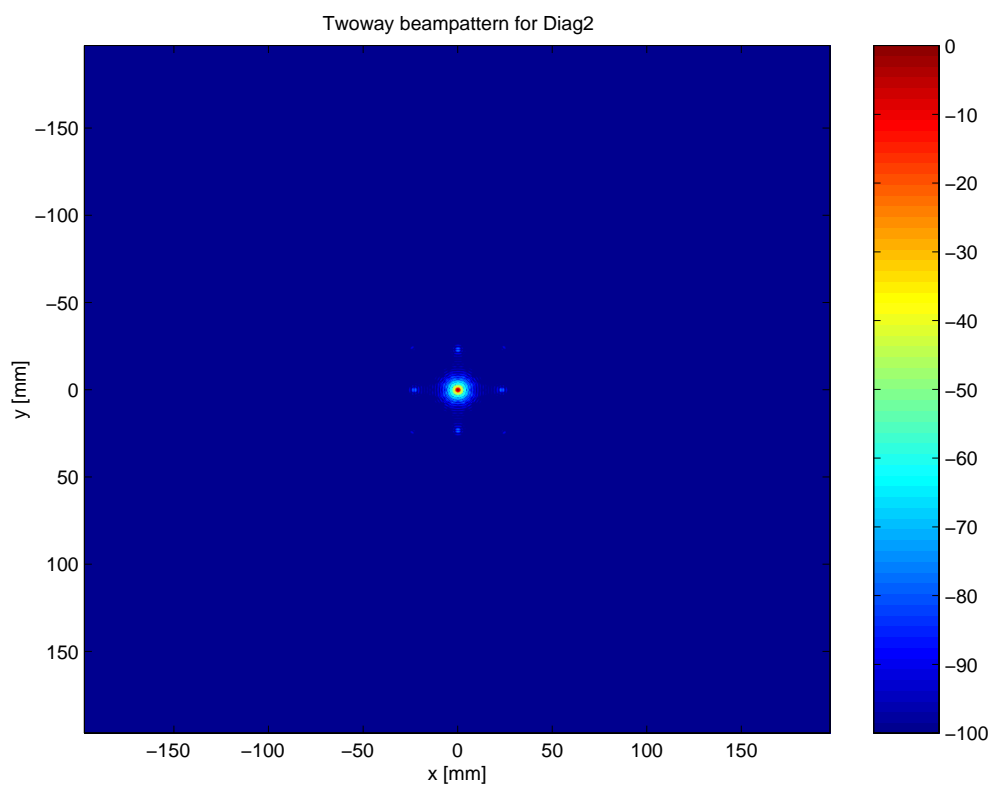
Figure 7.13: Harmonic two-way response from a point scatterer.

Figure 7.14: Conventional two-way response from a point scatterer.

(a) AxdpTx.

(b) AxdpRx.

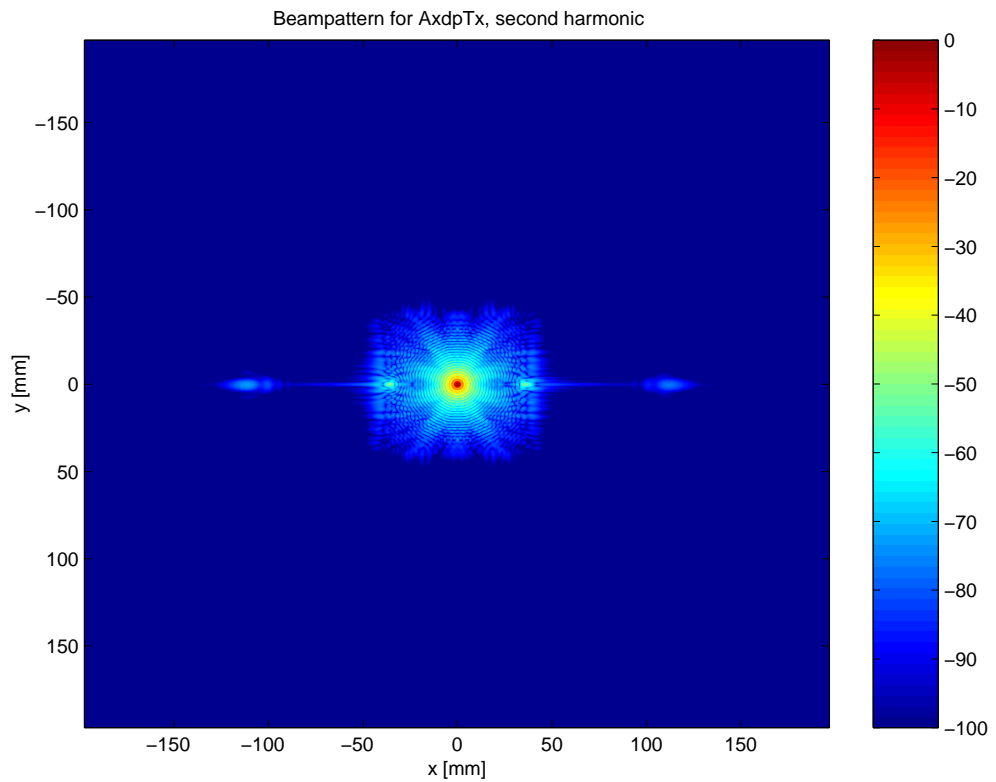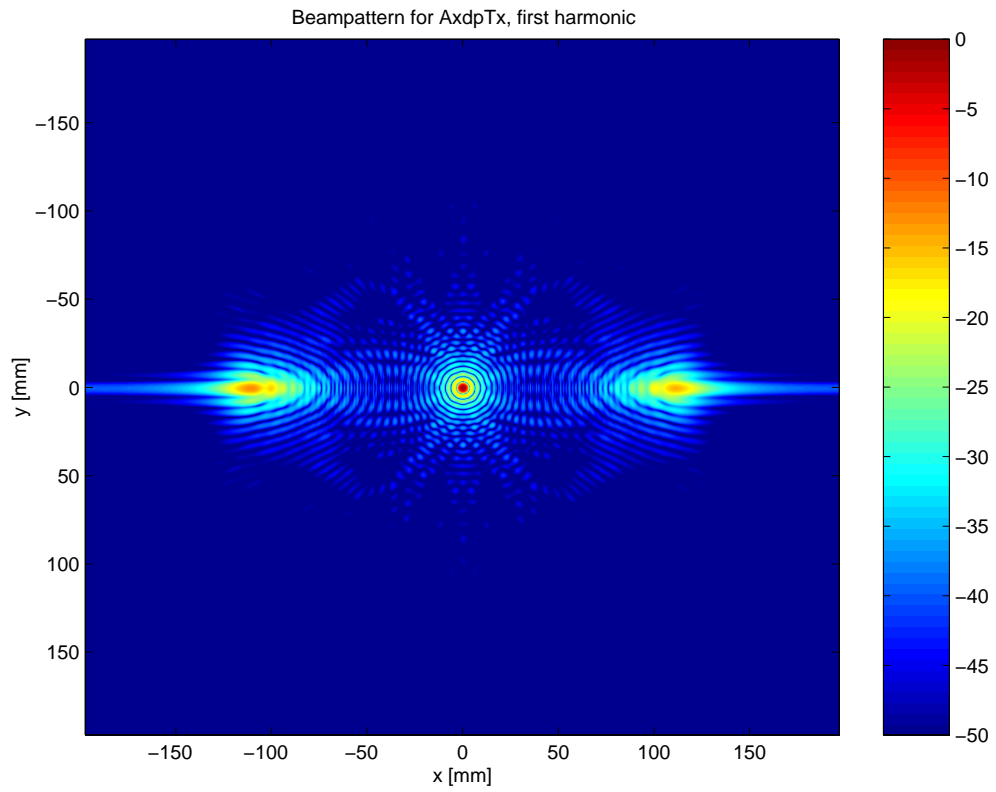Figure 7.15: Axial dense-periodic transducer used at transmission and reception.
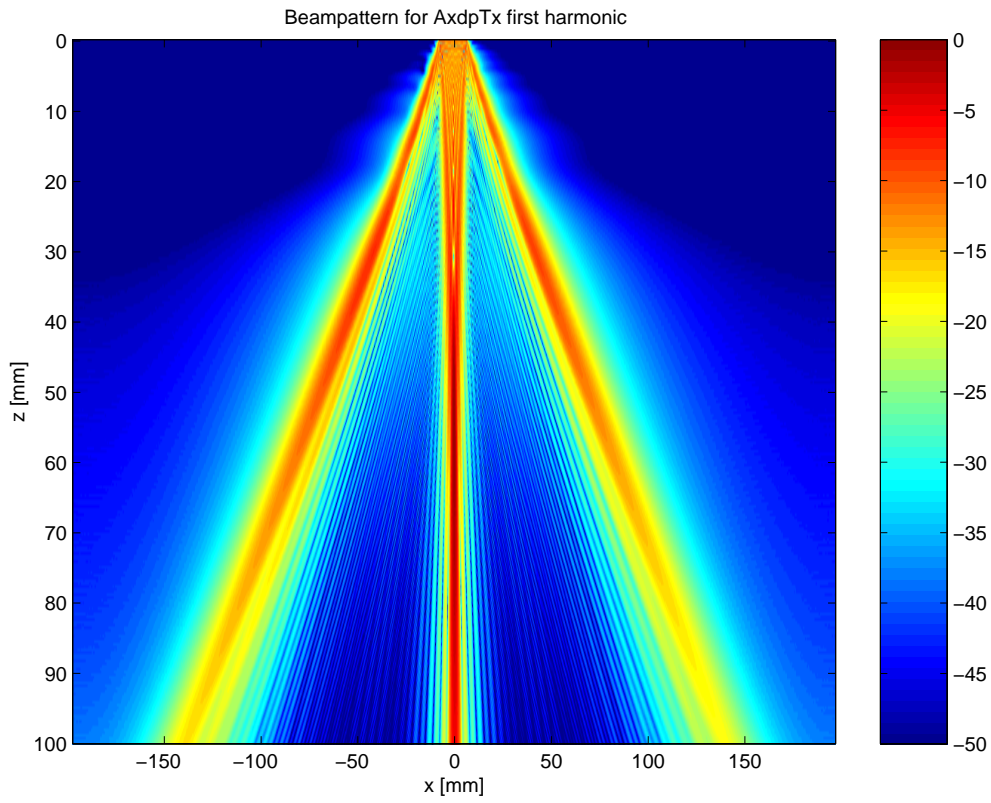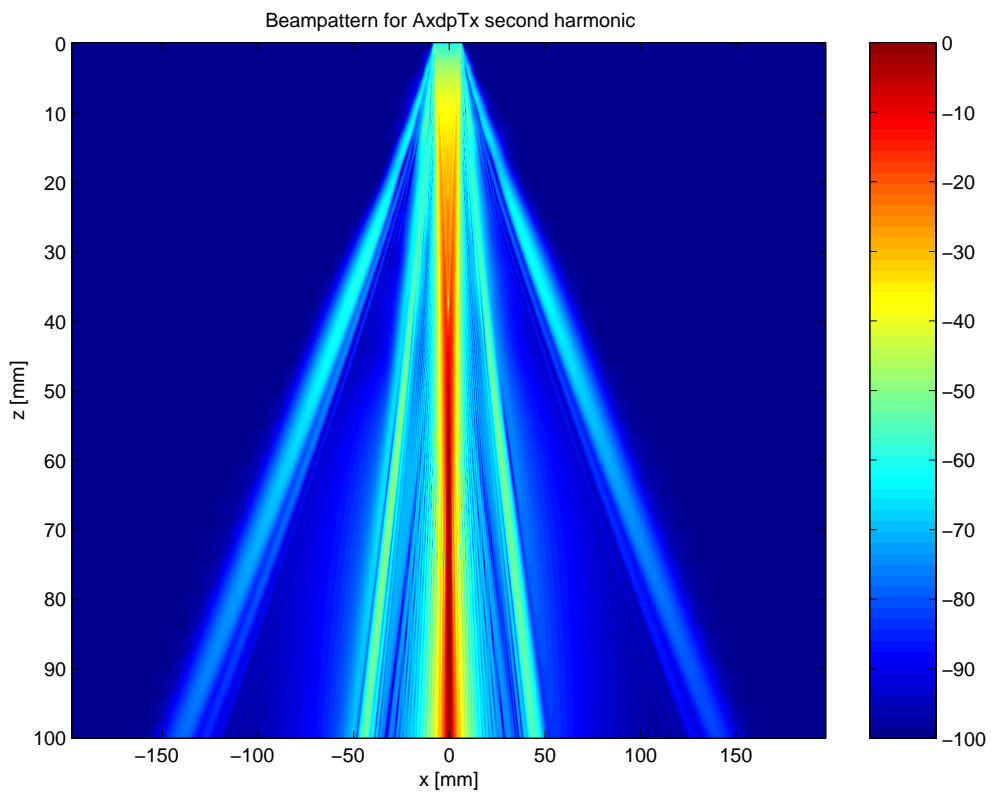
(a) AxdpTx.

(b) Second harmonic.

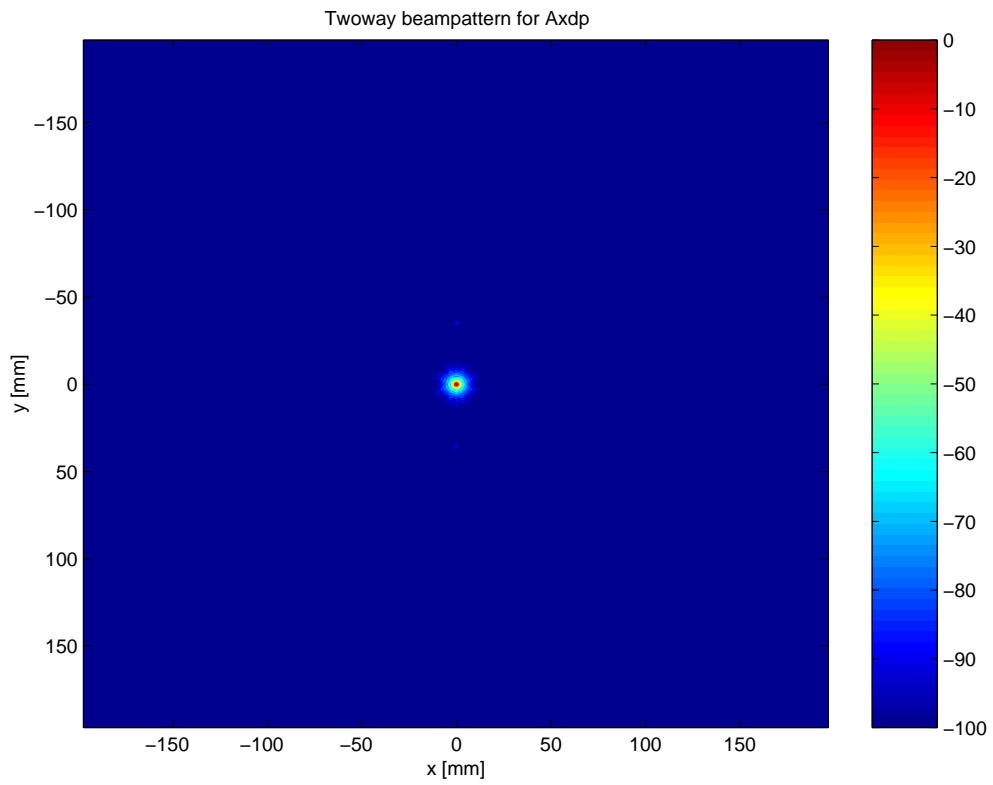Figure 7.16: First and second harmonics in focal plane $z = 80$ mm.
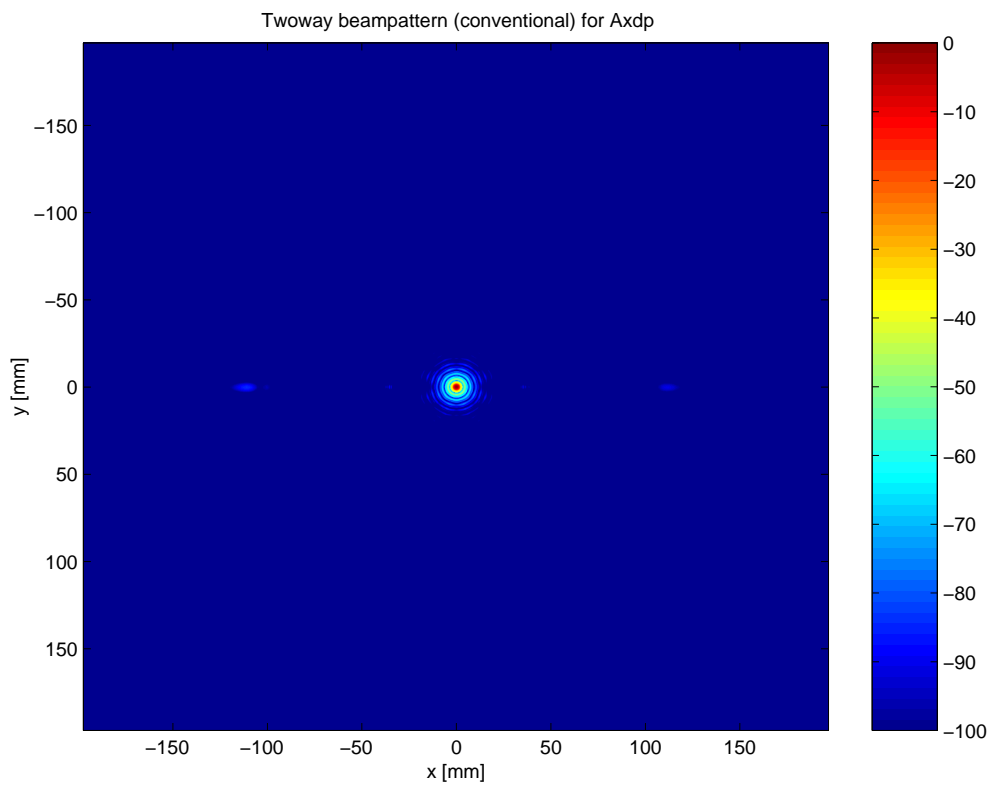
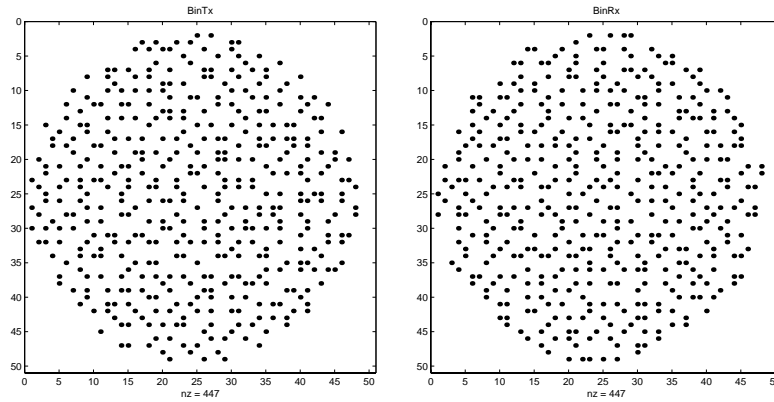(a) First harmonic.

(b) Second harmonic.

Figure 7.17: First and second harmonics in $y = 0$ plane.

(a) Harmonic two-way response from a point scatterer.

(b) Conventional two-way response from a point scatterer.

(c) BinTx.   (d) VernRx.

Figure 7.18: Binned transducer used at transmission and reception.

7.4.4 Binned transducer

Non-overlapping random layouts have the advantage that they separate transmit and receive elements. Rectangular binned arrays are constructed by dividing the array into equal-size bins, and then an element is chosen at random within each bin. This prevents the existence of grating lobes, but the sidelobe level is generally higher.

The transmit and receive layouts are constructed with a bin size of 2x2 elements. When the receive layout is chosen, there is a restriction on the receive layout. It is not allowed to use the same element as was chosen in the transmit array. This makes the layout non-overlapping. The transducer geometry in this case is shown in figure 7.18.

The simulation for these layouts is shown in figure 7.19. The same image scaling is used as in the previous examples. It is seen that there are no grating lobes and the sidelobe level is almost constant. The second harmonic has a smaller area with high sidelobes.

In this case the beam pattern in the $y = 0$ plane is given in figure 7.20. There are no fingers in the second harmonic in this case either.

The two-way harmonic response from a point scatterer is shown in figure 7.21(a). The conventional two-way response is shown in figure 7.21(b). The mainlobe width is greater and the sidelobe level is higher compared to the harmonic image.
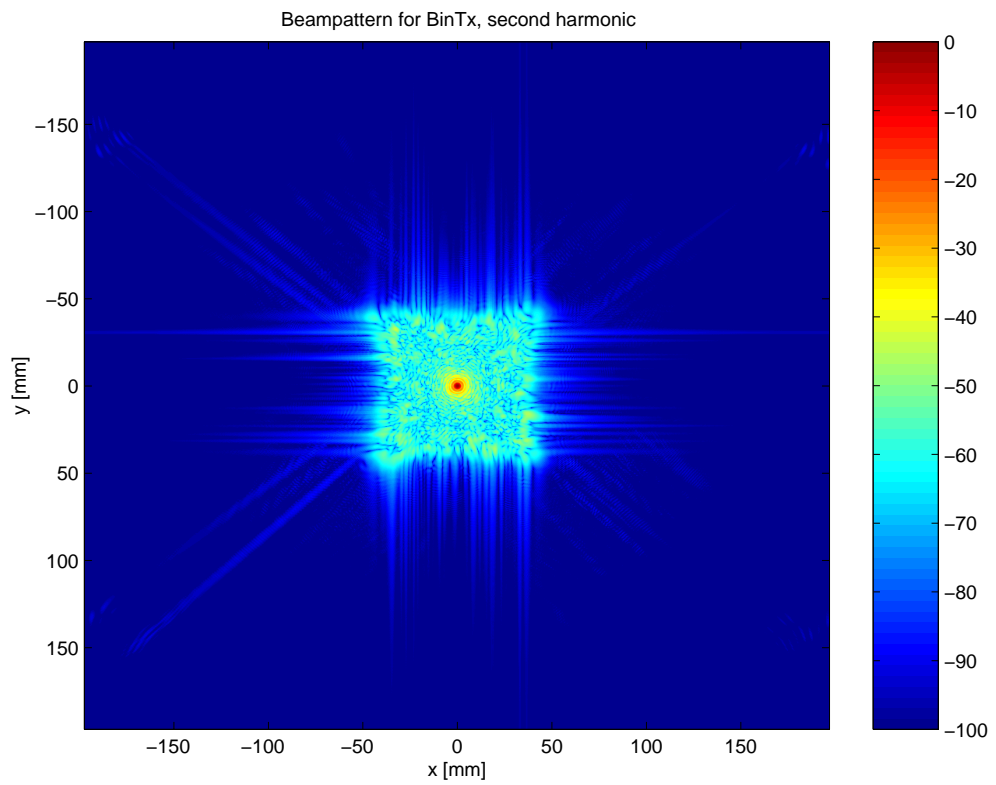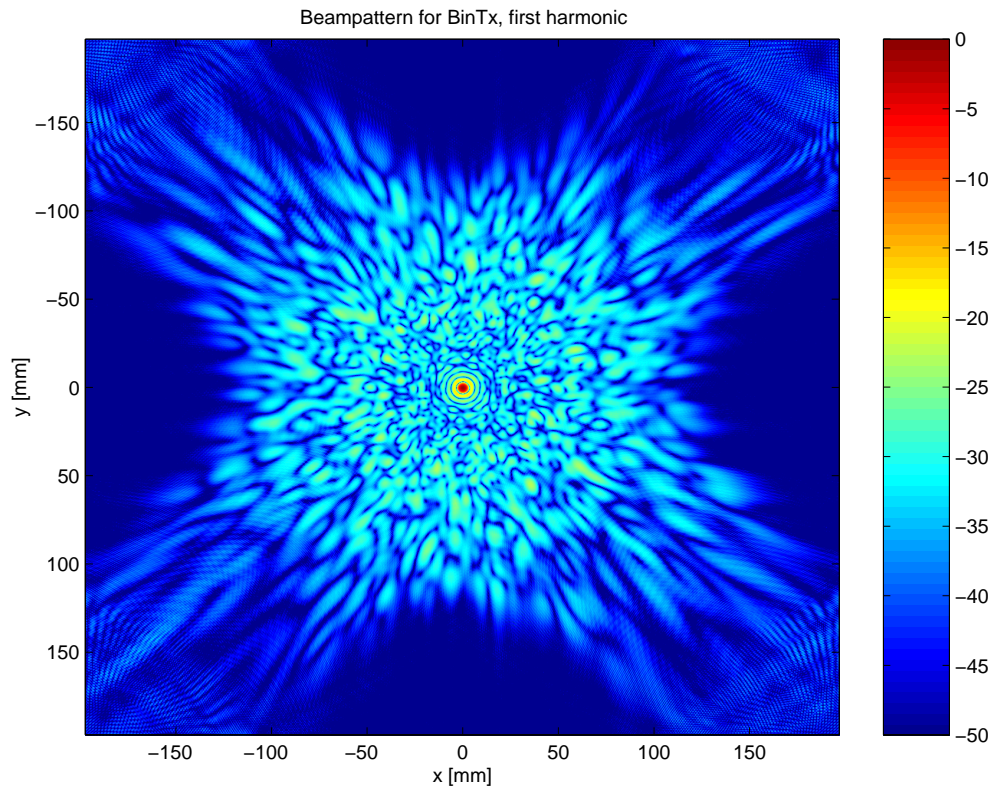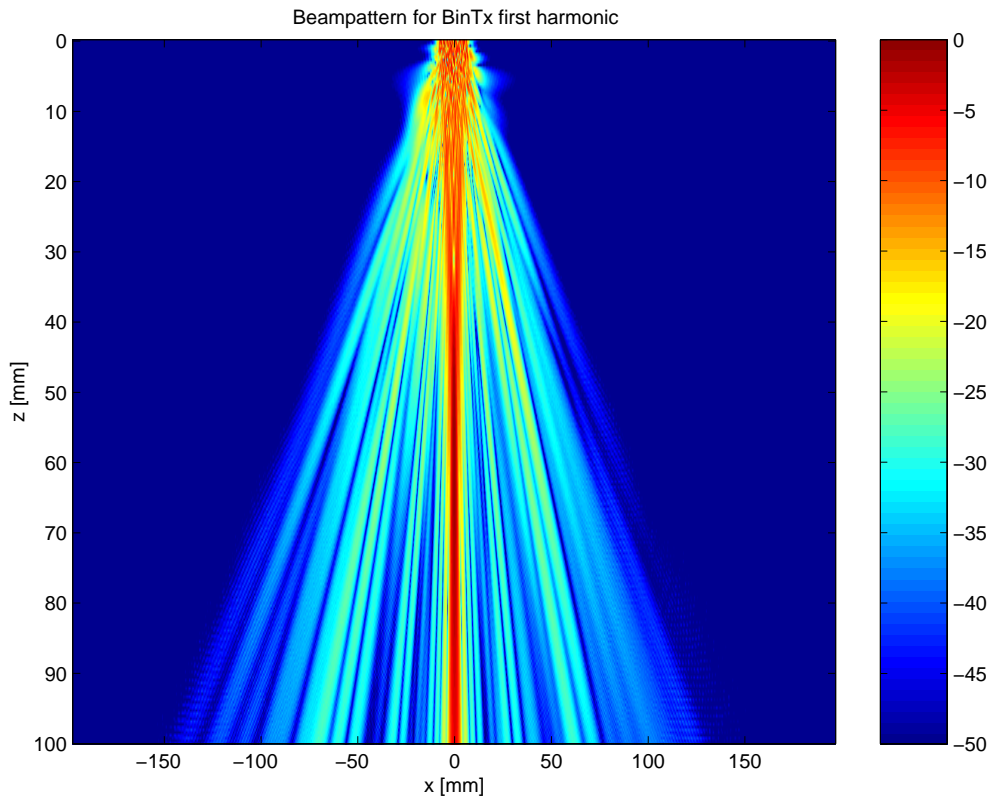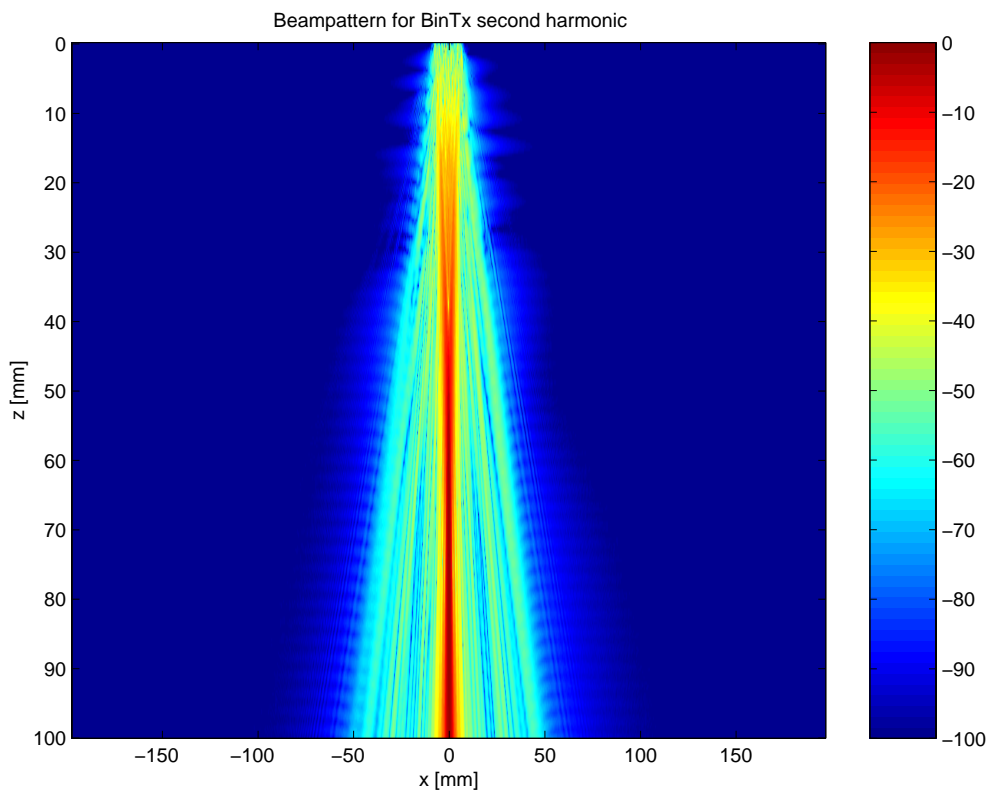
(a) BinTx.

(b) Second harmonic.

Figure 7.19: First and second harmonics in focal plane $z = 80$ mm.

(a) First harmonic.

(b) Second harmonic.

Figure 7.20: First and second harmonics in $y = 0$ plane.
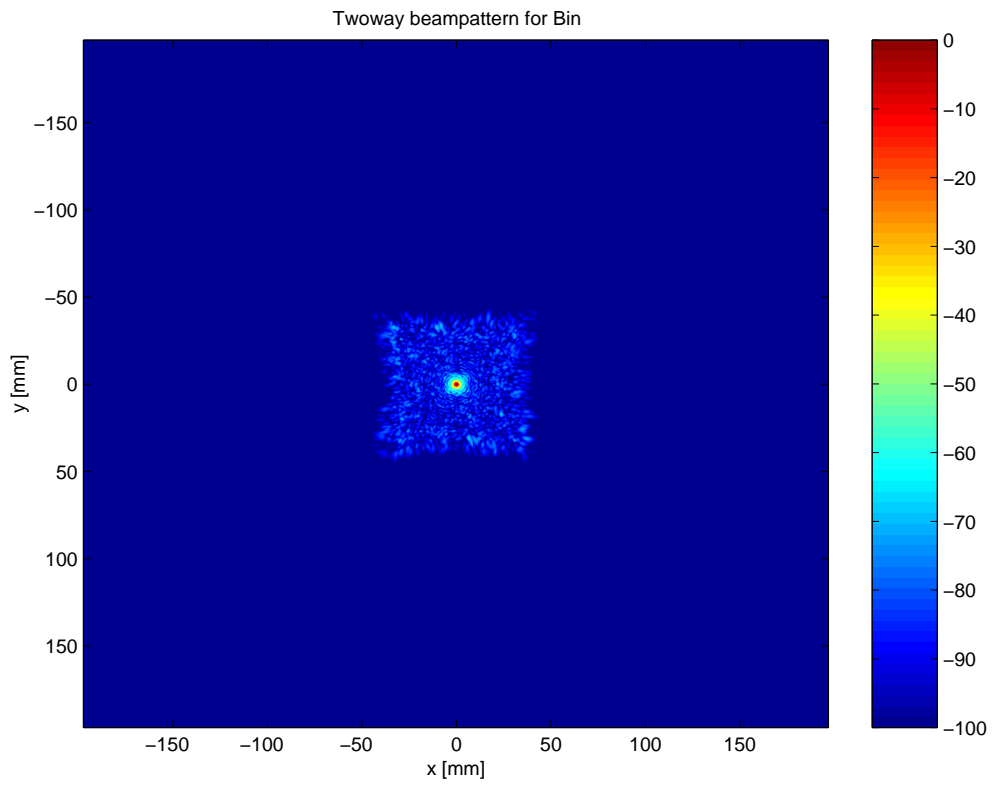
(a) Harmonic two-way response from a point scatterer.
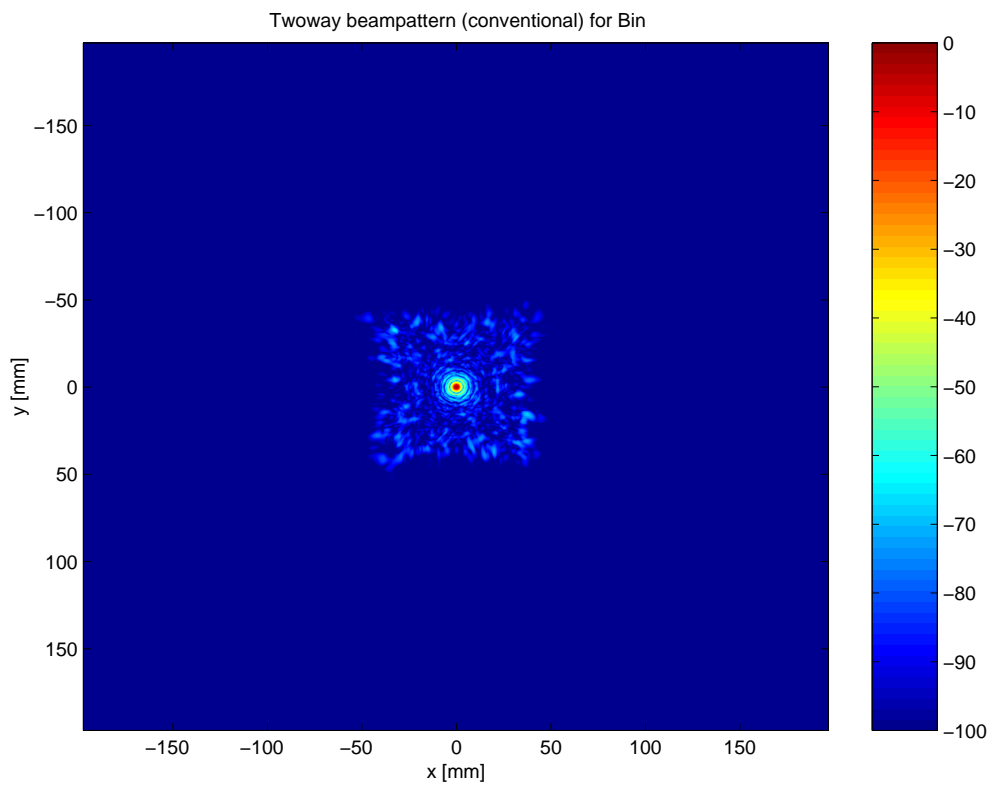
(b) Conventional two-way response from a point scatterer.
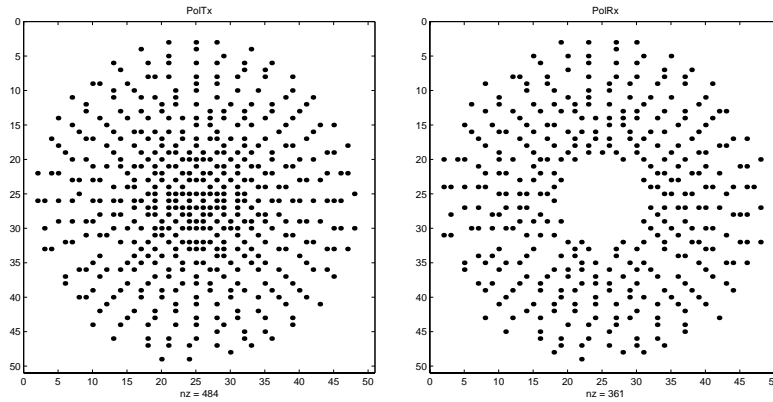
(c) PolTx.

(d) PolRx.

Figure 7.21: Polar transducer used at transmission (a) and reception (b).

7.4.5 Polar binned transducer

Another approach, called polar binned, is to choose elements in a binned way along rays from the center to the edges. The receive array was constructed by rotating the rays half the angle between two adjacent rays. The transducer geometry in this case is shown in figure 7.21.

The simulation for these layouts is shown in figure 7.22. The results do not differ much from those of the binned simulation.

In this case the beam pattern in $y = 0$ plane is given in figure 7.23.

The two-way response from a point scatterer is shown in figure 7.24(a). The backscattered beam pattern looks like the binned case, but the sidelobe level is slightly lower.

7.4.6 Worst case comparison

The worst case comparison of all the simulations is shown in figure 7.24 and figure 7.25. The second figure is a zooming of the first since it is only interesting to study the signals down to about -80 dB.

It is a bit unfair to compare all the different geometries. They have different amount of active elements and this implies that the costs of the transducer varies. Also the flexibility of choosing the sparseness is a factor to consider.

The Vernier transducers are used with the sparseness factor of $p = 3$ and $p = 2$. These are the lowest possible values for using different layouts for transmission and reception. Diagonal and Vernier transducers consist of the

Beampattern for PolTx, first harmonic

(a) PolTx.

Beampattern for PolTx, second harmonic

(b) Second Harmonic.

Figure 7.22: First and second harmonics in focal plane $z = 80$ mm.

85

(a) First harmonic.
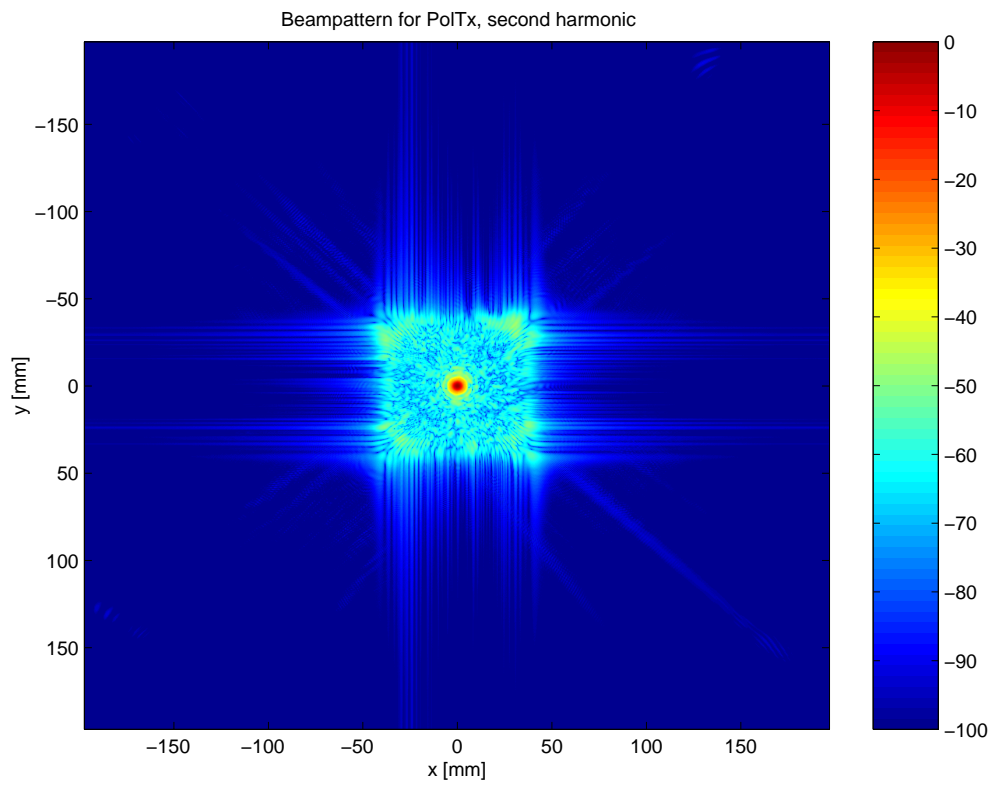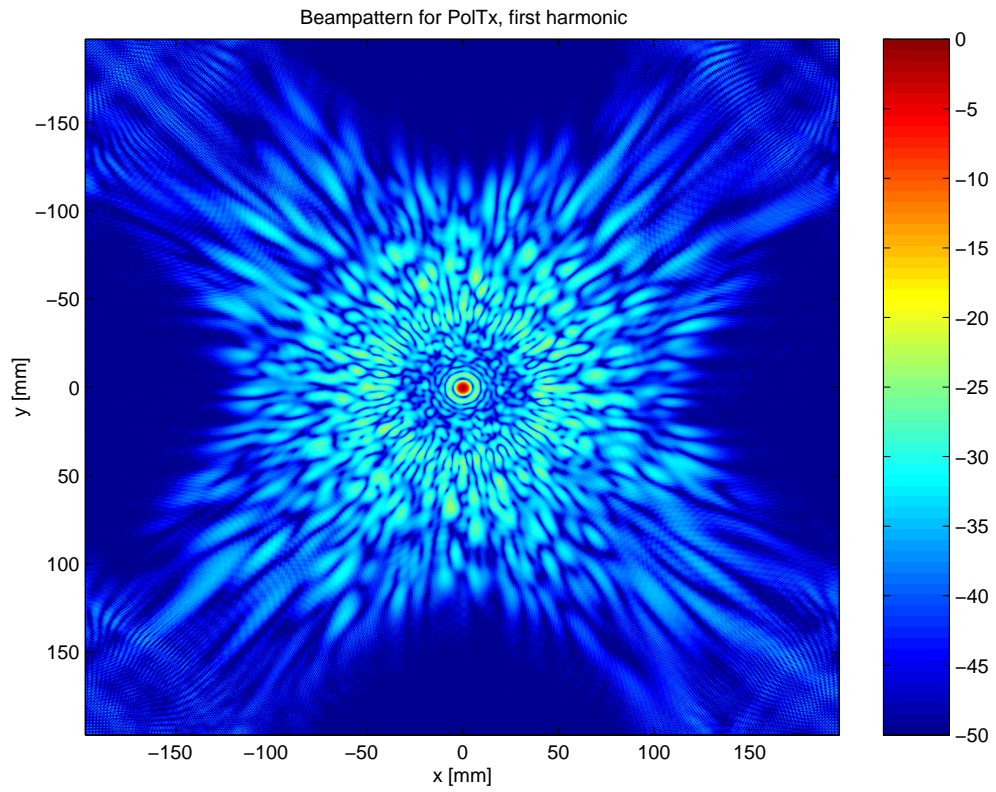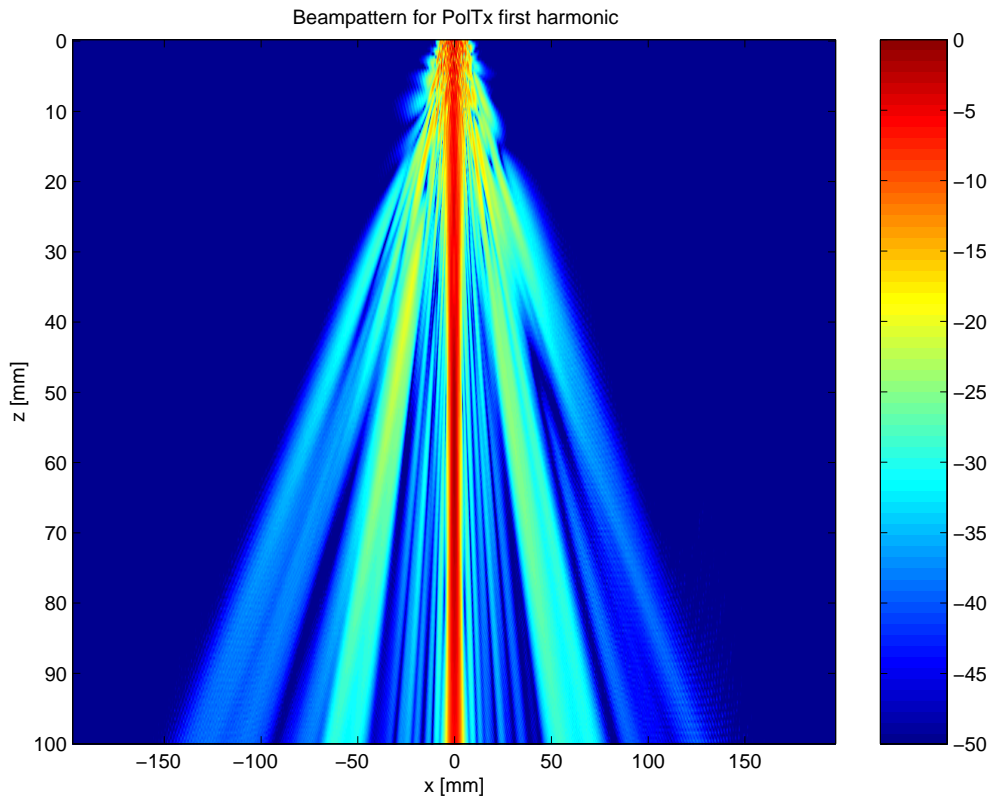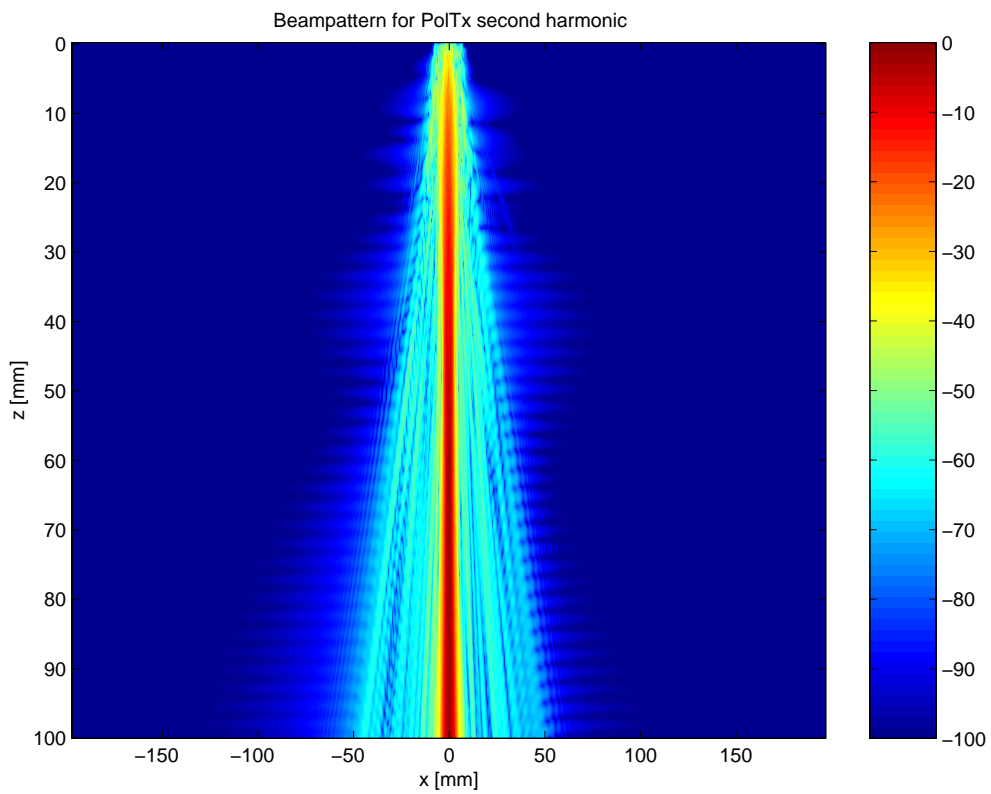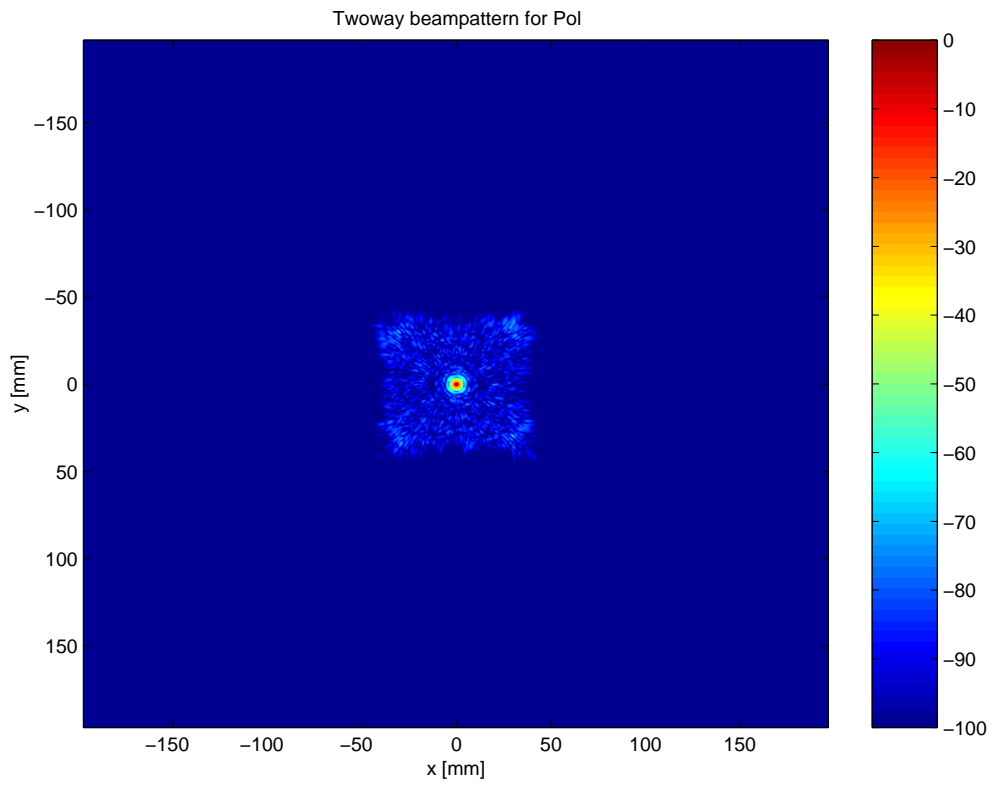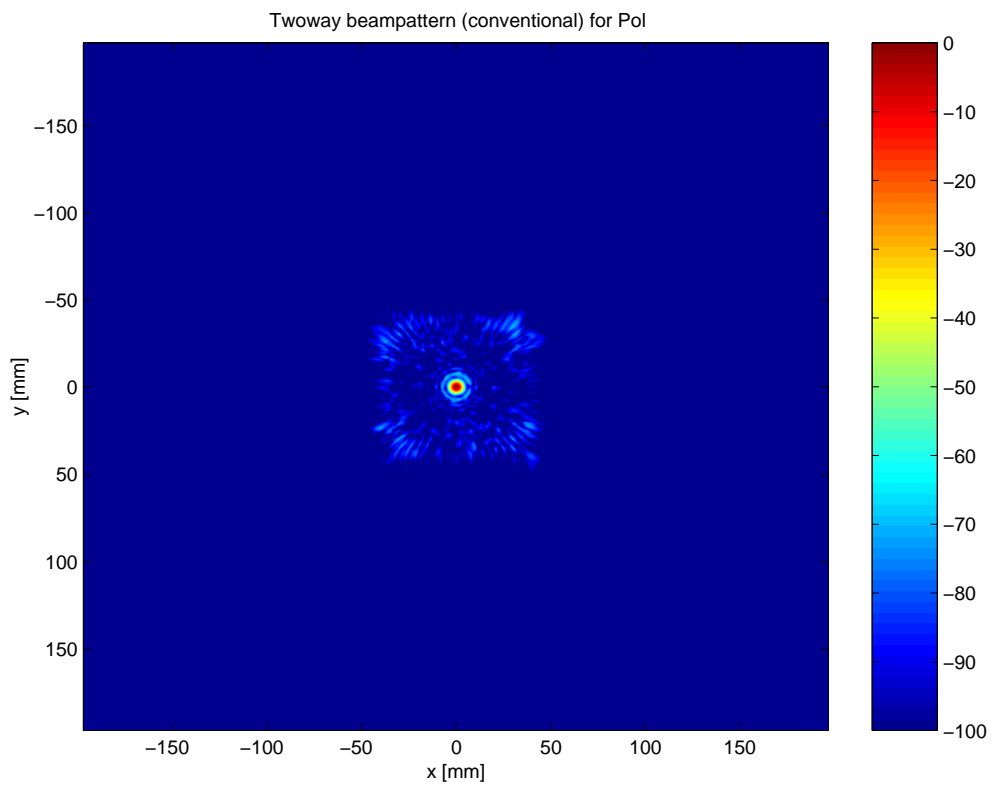

(b) Second harmonic.

Figure 7.23: First and second harmonics in $y = 0$ plane.

86

(a) Harmonic two-way response from a point scatterer.

(b) Conventional two-way response from a point scatterer.

Layout	Tx	Rx	Overlapping elements	Sum(Class)
Axial Dense Periodic	880	880	428	1760(3)
Diagonal 2	877	796	396	1673(3)
Improved Vernier	421	796	182	1217(2)
Diagonal 1	877	208	99	1085(2)
Binned	447	447	0	894(1)
Polar Binned	484	361	0	845(1)
Vernier	421	208	48	629(1)

Table 7.3: Number of elements in the different layouts.

largest number of elements considered here. Therefore, they are expected to give good performance, and this is shown in the figure.

Other types of transducers are the binned and the polar binned. They have an approximately constant sidelobe level. This is advantageous since there is no worst direction. Also, it is easy to define the sparseness factor with the polar binned layout. The number of elements in each direction and the number of directions can be chosen. This makes it possible to design a transducer with a certain number of elements.

Table 7.3 shows the number of elements used in transmission and reception showed for the different layouts. The number of overlapping elements is also included.

The unnormalized pressures are shown in figure 7.26. The levels are not normalized to see how much energy in the main lobe that is generated from each simulation. The level depends on how many elements that are used. This is the number of transmission elements added by the number of reception elements. The highest number generates the highest pressure, but the Diagonal 1 has higher pressure than the Improved Vernier despite the latter has 132 more active elements.

Figure 7.29 demonstrates that the mainlobe width of the conventional are larger than harmonic imaging. This figure shows the binned transducer, but this is generally the case.

It is difficult to chose a best layout, but the axial dense-periodic array are probably best from the figure 7.25. The Vernier and improved Vernier are also good. The Diagonal 1 and Diagonal 2 suffer from high grating lobes.

Austeng et al. [2] suggest to form three groups to compare the layouts regardless of design method. The first group consists of design with less than 906 elements. Simulations in this first class is Binned, Polar and Vernier. The latter has generally lower sidelobes and can be considered as the best in this class.

	Conventional		Harmonic	
Transducer	-6 dB	-50 dB	-6 dB	-50dB
Axial Dense Periodic	0.9758	5.6022	0.8791	2.9985
Diagonal 2	0.9756	5.5300	0.8740	2.9837
Improved Vernier	0.9704	5.5994	0.8707	2.9912
Diagonal 1	0.9616	5.4896	0.8645	2.8866
Binned	0.9761	5.7330	0.8747	3.0225
Polar Binned	1.0064	3.8841	0.9356	3.4742
Vernier	0.9747	5.6107	0.8825	2.8626

Table 7.4: Mainlobe beam width comparison of conventional and harmonic imaging.

In the second group each design has sum of elements approximately equal to 1300. The layouts simulated are Diagonal 1 and improved Vernier. The improved Vernier has generally lower sidelobe level so it is better than the Diagonal 1.

The last group has sum of more than 1673 elements. The Axial dense-periodic and Diagonal 2 are simulated in this group. The first has, as discussed previously, generally lower sidelobe level.

In table 7.4 is harmonic and conventional imaging compared. The -6 dB level of the harmonic is some smaller than the conventional. This will improve the resolution some. The more striking result is that the -50 dB level of the harmonic is half the level of the conventional. This will give an improvement of the contrast resolution in the images.

Figure 7.24: Worst case for all the harmonic simulations.

Figure 7.25: Worst case for all the harmonic simulations (zoomed version of the previous figure).

Figure 7.26: Worst case pressure comparison for all the harmonic simulations.
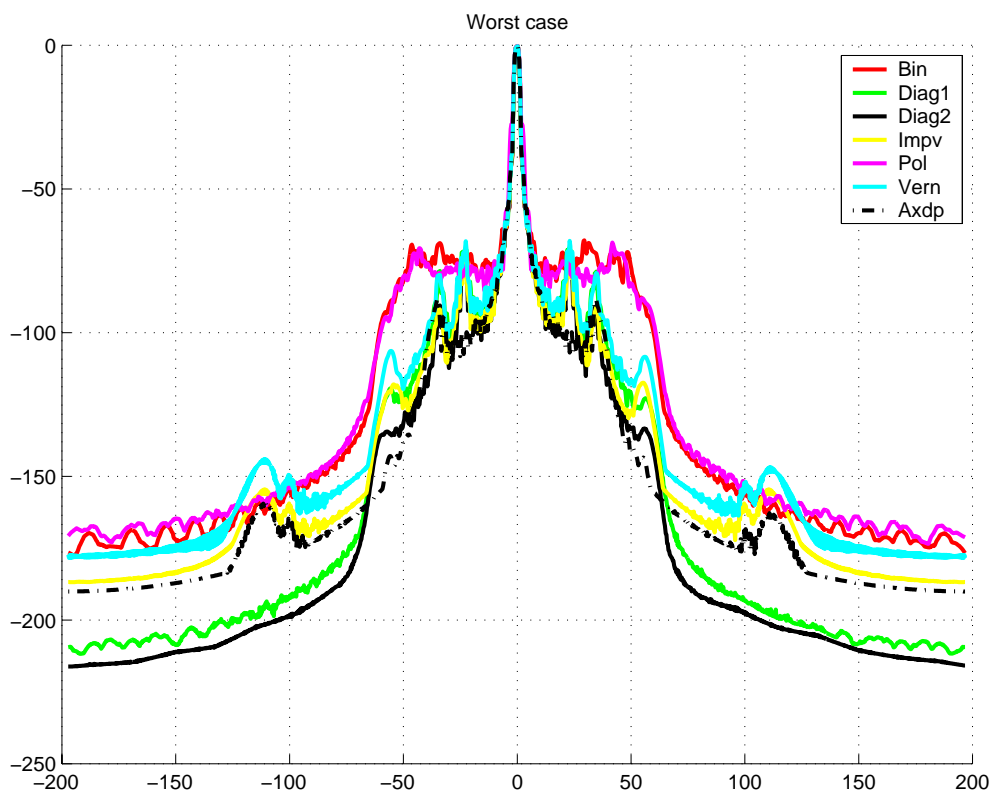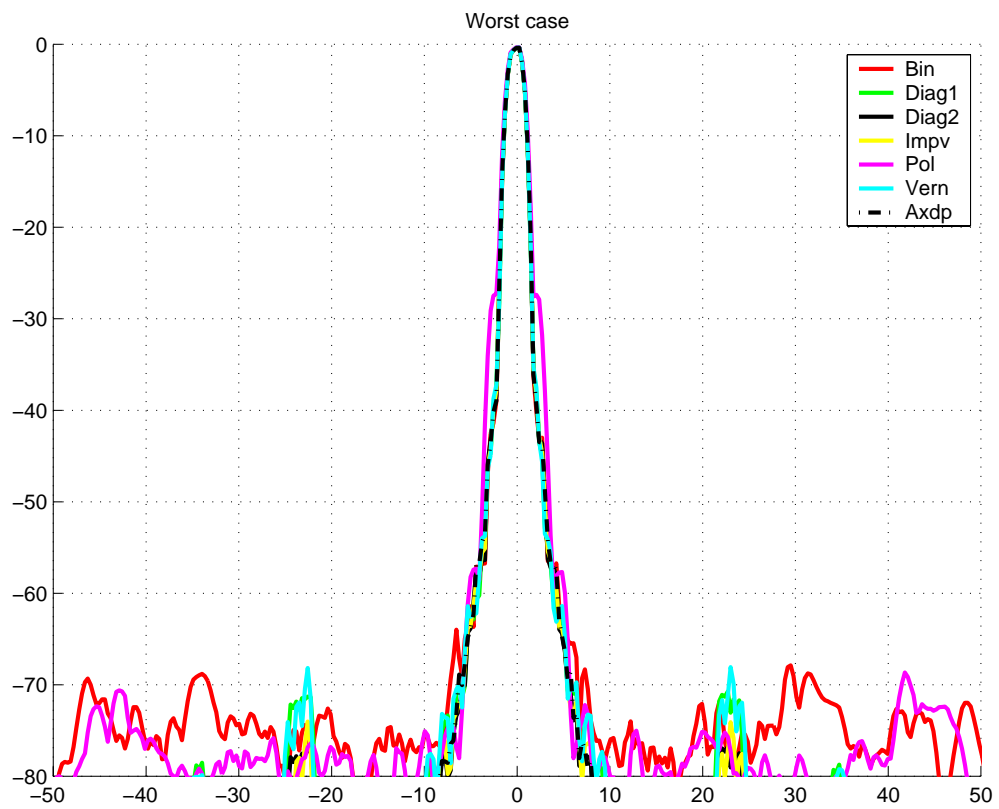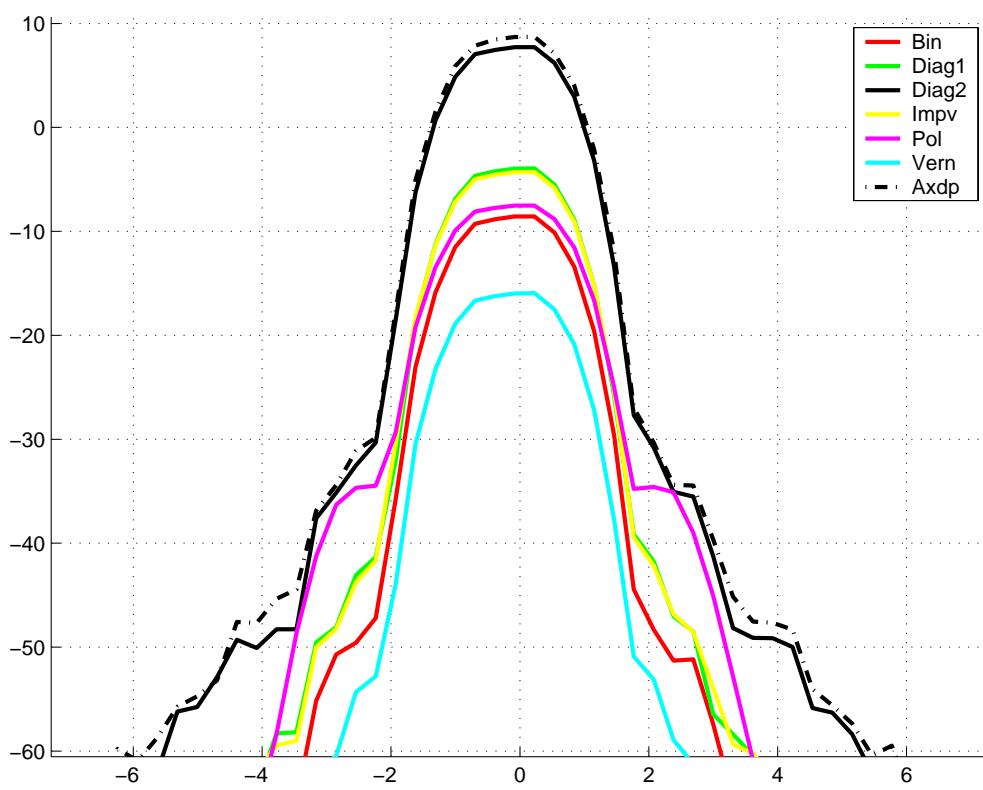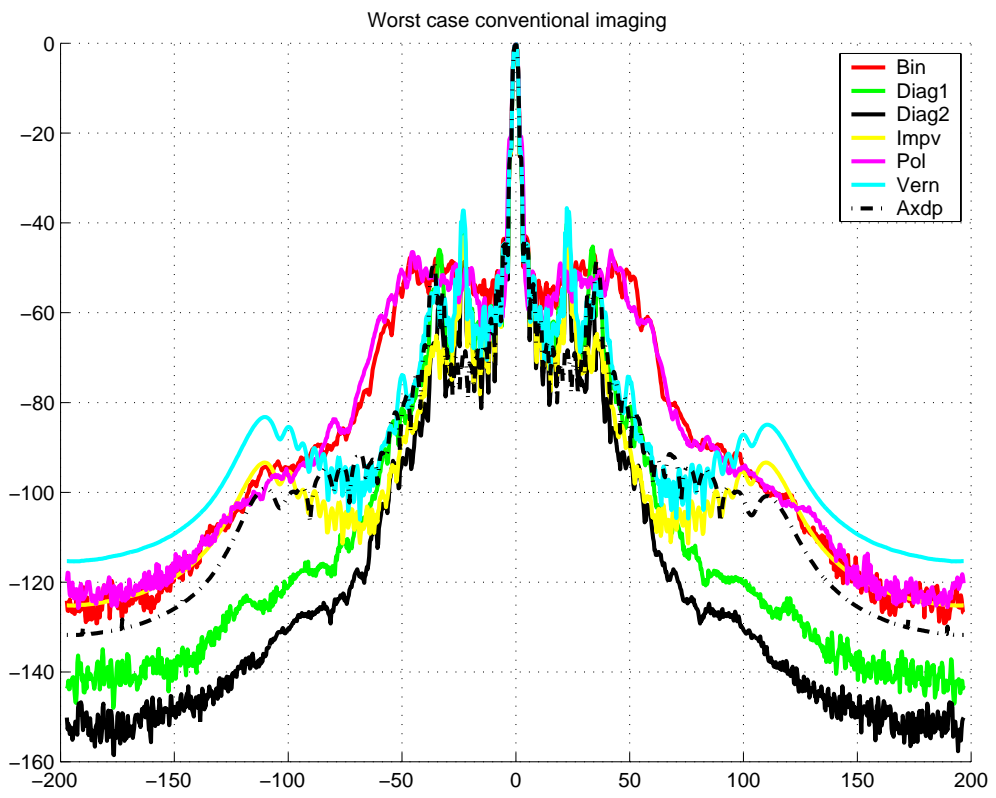
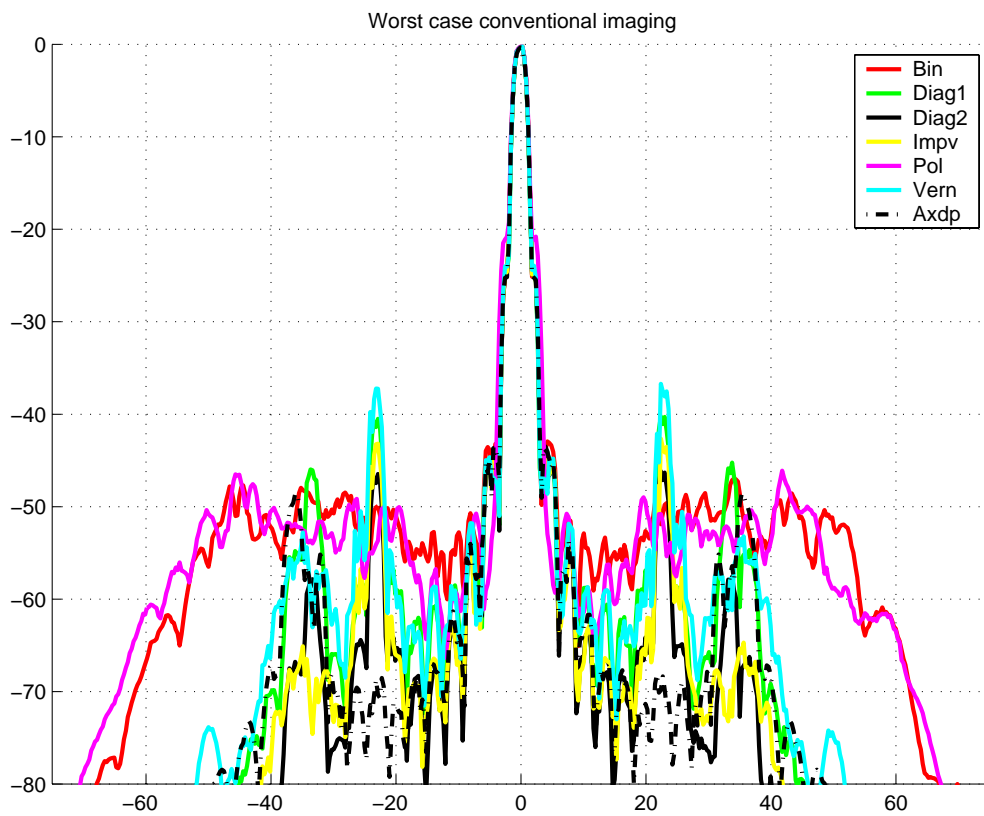Figure 7.27: Worst case for all the fundamental simulations.

Figure 7.28: Worst case for all the fundamental simulations (zoomed version of the previous figure).
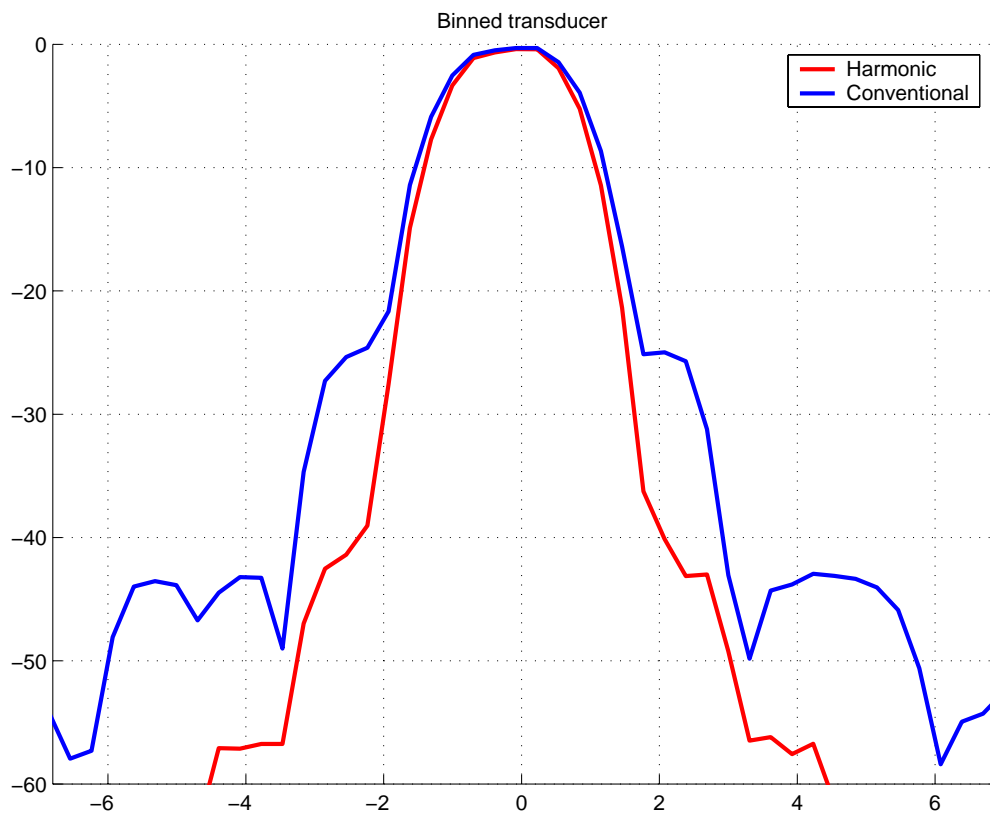
Figure 7.29: Mainlobe width comparison between conventional and harmonic imaging.

Chapter 8

Conclusion and further work

The aim of this thesis has been to extend the angular spectrum algorithm to non-symmetric sources. Burgers equation was used to simulate nonlinear wave propagation. This was then implemented in matlab and verified on measured fields. Finally, some new transducers were simulated which may be used for real-time 3-D imaging. The

The challenges of implementation has been to reduce the memory usage and the execution time.

The simulations are restricted to water, and only continuous waves are simulated. The simulator is ready to be used on pulsed waves, but a parallel computer, to handle the large calculations, was not ready in time. A parallel version of fast Fourier transform was used, so all that is needed is a parallel computer with large enough nodes.

When it was decided to use continuous wave, the field sizes was extended to use as much memory as possible without allowing the computer to swap memory to disc. It was possible to simulate the field in focus to in about $45°$.

Fingers appear on the second harmonic where the fundamental is zero. This was verified in the simulations carried out. A new type of finger has been observed when grating lobes were studied. The second harmonic had a grating lobe at the half of sine to the angle of the fundamental. This has also been measured of NTNU in Trondheim by professor Hans Torp and it is not been reported in the literature before. The practical concern is to make sure that grating lobes are not in the same direction as this new grating lobe appears.

The comparison between conventional and harmonic imaging shows that the contrast is improved. The mainlobe width is slightly smaller with harmonic simulation, but the sidelobe level is lower.

Generation of harmonics depends heavily on the initial pressure of the source. In this thesis the simulations have used mainly one initial pressure, and it would be interesting to experiment with other pressures and see how this

influences harmonic generation.

Also, it would be interesting to simulate pulsed waves. This should not be too difficult to do now, as computer capacity is increasing. This can be done by sampling a pulsed wave in the frequency domain and simulating the different continuous waves with the appropriate weighting.

The transducers used in this thesis are not steered to an angle, and this could be another thing to investigate. When steering is used, non-physical angles appear in the observed field and grating lobes may appear.

It would also be interesting to explore simulation with other values of the β-parameter. Nonlinear propagation with tissue- and fat-values could be studied.

Bibliography

[1] Andreas Austeng and Sverre Holm. Sparse 2D arrays for 3D phased array imaging. *To be submitted*, October 2000.

[2] Andreas Austeng and Sverre Holm. Sparse arrays for real-time 3D imaging, simulated and experimental results. *IEEE Ultrasonics Symposium 2000*, 2000.

[3] Michalakis A. Averkiou, David N. Roundhill, and Jeffry E. Powers. A new imaging technique based on the nonlinear properties of tissues. *IEEE Ultrasonics symposium*, pages 1561–1566, 1997.

[4] Jarle Berntsen, Jacqueline Naze Tjøtta, and Sigve Tjøtta. Nearfield of a large acoustic transducer. part IV: Second harmonic and sum frequency radiation. *J. Acoust. Soc. Amer*, 75(5):1383–1391, 1984.

[5] P. Ted Christopher and Kevin J. Parker. New approaches to the linear propagation of acoustic fields. *J. Acoust. Soc. Amer*, 90(1):507–521, 1991.

[6] P. Ted Christopher and Kevin J. Parker. New approaches to the nonlinear propagation of acoustic fields. *J. Acoust. Soc. Amer*, 90(1):488–499, 1991.

[7] Ted Christopher. Finite amplitude distortion-based inhomogeneous pulse echo ultrasonic imaging. *IEEE Trans. Ultrason., Ferroelect., Freq. Contr.*, 44(1):125–139, January 1997.

[8] Joseph W. Goodman. *Introduction to Fourier optics*. McGraw-Hill Inc., 1968.

[9] Mark F. Hamilton and David T. Blackstock. *Nonlinear Acoustics*. Academic Press, 1998.

[10] Michael E. Haran and Bill D. Cook. Distortion of finite amplitude ultrasound in lossy media. *J. Acoust. Soc. Amer*, pages 774–779, March 1982.

[11] Don H. Johnson and Dan E. Dudgeon. *Array signal processing*. Prentice Hall, 1993.

[12] L. D. Landau and E. M. Lifshitz. *Fluid Mechanics*. Butterworth Heinemann, 1987.

[13] Geoffrey R. Lockwood and F. Stuart Foster. Optimizing the radiation pattern of sparse periodic two-dimensional arrays. *IEEE Trans. Ultrason., Ferroelect., Freq. Contr.*, 43(1):15–19, January 1996.

[14] J. C. Lockwood, T. G. Muir, and D. T. Blackstock. Directive harmonic generation in the radiation field of a circular piston. *J. Acoust. Soc. Amer*, 53(4):1148–1153, 1973.

[15] S. Makarov and M. Ochmann. Nonlinear and thermoviscous phenomena in acoustics, part ii. *Acustica*, 83:197–222, 1997.

[16] Alan V. Oppenheim and Ronald W. Schafer. *Discrete-time signal processing*. Prentice Hall, 1989.

[17] S. W. Smith, H. G. Pavy, and O.T. von Ramm. High-speed ultrasound volumetric imaging system. part I: Transducer design and beam steering. *IEEE Trans. Ultrason., Ferroelect., Freq. Contr.*, 38(2):100–108, 1991.

[18] Peter R. Stepanishen and Kim C. Benjamin. Forward and backward projection of acoustic fields using FFT methods. *J. Acoust. Soc. Amer*, 74(4):803–812, 1982.

[19] Johan-Fredrik Synnevåg. *Linear and nonlinear propagation of limited diffraction beams*. Cand. Scient. thesis, University of Oslo, 1999.

[20] Kai E. Thomenius. Impact of nonlinear propagation on temperature distributions caused by diagnostic ultrasound. *IEEE Ultrasonics symposium*, pages 1409–1413, October 1998.

[21] D. H. Trivett and A. L. Van Buren. Comments on "Distortion of finite amplitude ultrasound in lossy media," by M. E. Haran and B.D. Cook [J. Acoust. Soc. Am. 73, 774-779 (1983). *J. Acoust. Soc. Amer*, pages 1257–1258, October 1984.

[22] Robert C. Waag, James A. Campbell, Jan Ridder, and Peter R. Mesdag. Cross-sectional measurements and extrapolations of ultrasonic fields. *IEEE Trans. Sonics and Ultrasonics*, 32(1):26–35, 1985.

Appendix A

Matlab code

Here is the Matlab (version 5.3) code given.

Some code to generate the figures are listed first, and then the simulator is given.

A.1   Script for generating figures

This is the matlab script for generating some of the figures used in this thesis.

```
file = 'vern';
file2 = ' Vern';

fn1 = strcat(strcat('/local/tmp/hfjelles/',file)...
              ,'Tx600t_cr_1_0.07995.dta');
fn2 = strcat(strcat('/local/tmp/hfjelles/',file)...
              ,'Tx600t_cr_2_0.07995.dta');

h1 = read_h3(fn1,1280);
h2 = read_h3(fn2,1280);

nx = -98.6*2:.308:98.6*2-.308;

figure(1)
imagesc(nx,nx,20*log10(abs(h1)/max(abs(h1(:)))));
caxis([-50 0]);
colorbar;
str = strcat(strcat('Beampattern for ',file2),'Tx, first harmonic');
title(str);
xlabel('x [mm]');
```

```
ylabel('y [mm]');
wf = strcat(file,'Txfoc80_1');
print('-depsc',wf);

figure(2)
imagesc(nx,nx,20*log10(abs(h2)/max(abs(h2(:)))));
caxis([-100 0]);
colorbar;
str = strcat(strcat('Beampattern for ',file2),'Tx, second harmonic');
title(str)
xlabel('x [mm]');
ylabel('y [mm]');
wf = strcat(file,'Txfoc80_2');
print('-depsc',wf);


fn1 = strcat(strcat('/local/tmp/hfjelles/',file),...
                    'Rx600_cr_1_0.07995.dta');
k1 = read_h3(fn1,1280);

figure(3)
imagesc(nx,nx,20*log10(abs(k1)/max(abs(k1(:)))));
caxis([-50 0]);
colorbar;
str = strcat(strcat('Beampattern for ',file2),'Rx, first harmonic');
title(str);
xlabel('x [mm]');
ylabel('y [mm]');
wf = strcat(file,'Rxfoc80_1');
print('-depsc',wf);


nz = 0:.39:100;

fn1 = strcat(strcat('/local/tmp/hfjelles/',file),'Tx600t1.dta');
fn2 = strcat(strcat('/local/tmp/hfjelles/',file),'Tx600t2.dta');
f1 = read_h(fn1,1280,256);
f2 = read_h(fn2,1280,256);

figure(4)
imagesc(nx,nz,20*log10(abs(f1)/max(abs(f1(:)))));
```

```
caxis([-50 0]);
colorbar;
str = strcat(strcat('Beampattern for ',file2),'Tx first harmonic');
title(str);
xlabel('x [mm]');
ylabel('z [mm]');
wf = strcat(file,'Txfoc80b_1');
print('-depsc',wf);

figure(5)
imagesc(nx,nz,20*log10(abs(f2)/max(abs(f2(:)))));
caxis([-100 0]);
colorbar;
str = strcat(strcat('Beampattern for ',file2),'Tx second harmonic');
title(str);
xlabel('x [mm]');
ylabel('z [mm]');
wf = strcat(file,'Txfoc80b_2');
print('-depsc',wf);

figure(6)
b = k1.*h2;
imagesc(nx,nx,20*log10(abs(b)/max(abs(b(:)))));
caxis([-100 0]);
colorbar;
str = strcat('Twoway beampattern for ',file2);
title(str);
xlabel('x [mm]');
ylabel('y [mm]');
wf = strcat(file,'two');
print('-depsc',wf);

figure(7)
b = h1.*h2;
imagesc(nx,nx,20*log10(abs(b)/max(abs(b(:)))));
caxis([-100 0]);
colorbar;
str = strcat('Twoway beampattern (conventional) for ',file2);
title(str);
xlabel('x [mm]');
ylabel('y [mm]');
```

```
wf = strcat(file,'twoc');
print('-depsc',wf);
```

A.2   Simulations

The calls to the simulator is shown for some examples below.

% Parker linear, article

```
as_main(3e6,1,Inf,Inf,0,0,10e-3,100,1,1500,...
    'parker_l_ex1_',200e-3,200e-3,0,-40e-3,...
    .125e-3,200e-3,'parker linear','y');
```

% Parker, nonlinear article

```
as_main(2.25e6,1,Inf,Inf,0,0,19e-3,1000,4,1486,...
    'parker_nl_ex2_',750e-3,.5e-3,0,-200e-3,(5/8)*1e-3,...
    [750e-3;2],'parker nonlinear example','y');
```

% Vingmed

```
as_main(2.3e6,1,80*1e-3,90*1e-3,0,0,11/2*1e-3+i*17/2*1e-3,...
    1000,4,1486,'kk05tst2_',100e-3,.5e-3,0,-61.76e-3,...
    .193*1e-3,[],'KK 05-vingmed transducer','y');
```

% Vernier

```
dir = pwd;
cd ~/hfag/andreas
load VernTx.txt;
weight = [zeros(1,50);VernTx;zeros(1,50)];
cd(dir);
as_main(3e6,1,80e-3,80e-3,50,0,7.5e-3,600,4,1540,...
    'vernTx600t',100e-3,.39e-3,weight,...
    -98.6*1e-3*2,.308*1e-3,[80e-3;3],'vernTx','n');
```

% (For conventional imaging)

```
dir = pwd;
cd ~/hfag/andreas
load VernTx.txt;
weight = [zeros(1,50);VernTx;zeros(1,50)];
cd(dir);
as_main(3e6,2,80e–3,80e–3,50,0,7.5e–3,600,1,1540,...
    'vernTx600c',100e–3,.39e–3,weight,...
    –98.6*1e–3*2,.308*1e–3,[80e–3;3],'vernTx','n');
```

A.3   Angular spectrum simulator

The program can be divided into these main stages:

- Calculate initial velocity field at transducer face.

- Calculate the propagation function

- Display parameters

- Start of main loop

    1. Linear substep

    2. Nonlinear substep

    3. Write to disc

function as_main(freq,send,e_foc,a_foc,tr_sz,att,...
    rad,in_pres,Nmax,c,f_name,z_max,z_inc,weight,...
    x_min,delta,cr_sec,descr,p_f);

```
% Main program to calculate the field!
% (3 harmonics are automatically in xz–plane are saved
%   to /local/tmp/hfjelles)
%
% freq      = design frequency [Hz]
% send      = part of design frequency used as
%               fundamental frequency
% e_foc     = elevation focus [m]
% a_foc     = azimuth focus [m]
% tr_sz     = transducer size (NxN) 0 if piston
% rad       = radius of transducer (complex number
%               for rectangular) [m]
% in_pres   = initial pressure [kPa]
```

```
% Nmax      = number of harmonics
% c         = speed of sound [m/s]
% f_name    = filename (concatunated with #harm.dta)
% z_max     = distance to propagate [m]
% z_inc     = distance between two parallell planes [m]
% weight    = element weight if transducer is not piston
% x_min     = minimum value in x and y direction (has to
%             be negative) [m]
% delta     = sampling in xy–plane [m]
% cr_sec    = vector of cross_sectional planes [m]
%             (2. row # of harm to save)
% descr     = description of geometry (text)
% p_f       = propagation function attenuated at edge?
%             'y' or 'n'

freq = freq*send;   % Frequency [Hz]
rho = 1000;         % density [kg/m^3]
alpha = 2.5e–14;    % attenuation coefficient [Np/(m*Hz^2)]
n_f = 2;            % exponent of frequency in attenuation
                    % expression
q = 0.35;           % excess attenuation factor
B_by_A = 11;        % value for fat
lambda = c / freq; % wavelength [m]

x_max = –x_min–delta;
y_min = x_min;
y_max = –y_min–delta;

a_focus = a_foc;
e_focus = e_foc;

values_x = x_min:delta:x_max;
values_y = y_min:delta:y_max;
N = length(values_x);

beta = 3.5;         % beta–factor (nonlinear parameter)

for ii=1:max(3,Nmax),
  eval(['u_s_' int2str(ii) ' = complex(zeros(N));']);
end;

for ii=1:Nmax,
  eval(['field_' int2str(ii) ' = complex(zeros(N));']);
```

```
   eval(['prop_func_' int2str(ii) ' = complex(zeros(N));']);
end;

% *****************************************
% Calculate initial field of the transducer
% *****************************************

del_ele = zeros(1,N);
del_az = zeros(1,N);
if (e_foc < Inf)
   del_ele = sqrt((values_x.^2)'+e_focus.^2) - e_foc;
else
   del_ele = del_ele';
end;
if (a_foc < Inf)
   del_az = sqrt((values_x.^2)'+a_focus.^2) - a_foc;
else
   del_az = del_az';
end;
u_s_3 = del_ele * ones(1,N) + (del_az * ones(1,N))';
clear del_az del_ele;
u_s_2 = exp(-i*2*pi*freq/c*u_s_3);
if (tr_sz ~= 0)
   u_s_1(N/2-tr_sz/2+1:N/2+tr_sz/2,N/2-tr_sz/2+1:N/2+...
       tr_sz/2) = 1;
   indx = find(u_s_1 == 1);
   u_s_1(indx) = reshape(weight,[tr_sz*tr_sz 1]).*1/c*...
       in_pres;
else
   if (imag(rad) == 0)
     u_s_3 = sqrt((ones(length(values_y),1)*values_x.^2 ...
         + ((ones(N,1)*values_y')).^2);
     u_s_1(find(u_s_3<=rad)) = 1/c*in_pres;
   else
     u_s_3 = ones(length(values_y),1)*values_x+i*...
         (ones(N,1)*values_y)';
     u_s_1(find(real(u_s_3) < imag(rad) & ...
         real(u_s_3) > -imag(rad) & imag(u_s_3) < ...
         real(rad) & imag(u_s_3) > -real(rad))) = 1/c*in_pres;
   end;
end;
u_s_1 = u_s_1.*u_s_2;
u_s_1 = fftshift(u_s_1);
```

```
fftw2(u_s_1,1)
field_1 = fftshift(u_s_1);

disp(['FFT size ', num2str(N)])
go2 = N / 2;                        % index to center of field

% eq(5) in Parker nonlin
for m = 1:Nmax
  b(1,m) = n_f + q * (m - 1) / Nmax;
end;

n_steps = fix(z_max / z_inc);       % number of steps
z_step = z_inc * (1:n_steps);
index_range = -go2:go2-1;
x_vals = index_range * delta;       % x-positions [m]
y_vals = x_vals;                    % y-positions [m]
x_min = min(x_vals);
x_max = max(x_vals);
wndw_size = x_max - x_min;
wo2 = wndw_size / 2;

u_s_1 = ones(N,1) * ((-N/2:N/2-1) / (N * delta));
u_s_2 = u_s_1';
u_s_1 = u_s_1.^2;
u_s_2 = u_s_1';
u_s_3 = u_s_1 + u_s_2;

% ***************************************
% Calculate propagation function & weights
% ***************************************

if (p_f == 'y')
  border = 0.75 * (-x_min);
  wid = -x_min - border;
  u_s_2 = sqrt((ones(length(values_y),1)*values_x).^2 + ...
      ((ones(N,1)*values_y)').^2);
  for m = 1:N,
    in = find(u_s_2(m,:) <= border);
    if isempty(in) == 0,
      u_s_1(m,in) = ones(size(in));
    end;
    in2 = find(u_s_2(m,:) > border);
    if isempty(in2) == 0,
```

110

```matlab
          u_s_1(m,in2) = zeros(size(in2));
          in3 = find((u_s_2(m,:) <= -x_min) & ...
              (u_s_2(m,:) > border));
          if isempty(in3) == 0,
            u_s_1(m,in3) = 0.5*(1+cos(pi*(...
                abs((u_s_2(m,in3)-border)/wid))));
          end;
        end;
    end;
else
    u_s_1(:) = 1;
end;

for m = 1:Nmax,
    mf_c = m * freq / c;
    arg = sqrt(mf_c^2 - u_s_3);
    eval(['prop_func_' int2str(m) ...
          ' = u_s_1.*exp(i * 2*pi * z_inc *arg)'...
          '.*exp(-att*freq*m/(1e6*20)*100*log(10)*z_inc);']);
end;

fprintf('Finished\n');

cent_pt = round(N/2);

save_dir = '/local/tmp/hfjelles/';
file_1 = strcat(strcat(save_dir,f_name),'1.dta');
file_2 = strcat(strcat(save_dir,f_name),'2.dta');
file_3 = strcat(strcat(save_dir,f_name),'3.dta');

fid1 = fopen(file_1,'w');
fclose(fid1);
fid1 = fopen(file_1,'a');
fid2 = fopen(file_2,'w');
fclose(fid2);
fid2 = fopen(file_2,'a');
fid3 = fopen(file_3,'w');
fclose(fid3);
fid3 = fopen(file_3,'a');

st = '';
for m = 1:Nmax-1,
    st = strcat(st,'field_',int2str(m),',');
```

111

end;
st = strcat(st,'field_',int2str(Nmax));

% Display parameters

```
fprintf(['\t TRANSDUCER (', descr ,'):\n']);
fprintf(['\tBeam type          = ', 'CW', '\n']);
fprintf(['\tRadius             = '...
      , num2str(rad*1e3), 'mm\n']);
fprintf(['\tInitial pressure   = '...
      , num2str(in_pres), 'kPa\n']);
fprintf(['\tFrequency          = '...
      , num2str(freq/1e6) ...
      'MHz(',num2str(freq/(send*1e6)),...
      'MHz,',num2str(send),')\n']);
fprintf(['\tElevation focus    = '...
      , num2str(e_foc*1e3), 'mm\n']);
fprintf(['\tAzimuth focus      = '...
      , num2str(a_foc*1e3), 'mm\n']);
fprintf(['\tWavelength         = '...
      , num2str(c/freq*1e3), 'mm\n']);
fprintf(['\t MEDIUM:\n']);
fprintf(['\tVelocity of sound  = '...
      , num2str(c), 'm/s\n']);
fprintf(['\tNon-lin. (beta)    = '...
      , num2str(beta), '\n']);
fprintf(['\tAttenuation        = '...
      , num2str(att), 'dB/cm/MHz\n']);
fprintf(['\t# harmonics        = '...
      , num2str(Nmax), '\n']);
fprintf(['\t# lateral samples  = '...
      , num2str(N/2), '\n']);
fprintf(['\tDensity            = '...
      , num2str(rho), 'kg/m^3\n']);
fprintf(['\tMaximum depth      = '...
      , num2str(z_max*1e3) 'mm\n']);
fprintf(['\tSampling in z      = '...
      , num2str(z_inc*1e3) 'mm\n']);
fprintf(['\tSampling in x&y    = '...
      , num2str(delta*1e3) 'mm\n']);
fprintf(['\tAtt of propfunc    = ', p_f ',\n']);
```

*% ********************

```matlab
% Start of propagation
% *******************

fprintf('Loop over z-values ...\n');

for idx = 1:n_steps,

  % Temporary, used only in the next line
  u_s_1 = ones(N,1)*x_vals * 100000;

  % u_s(2,:,:) is now the spatial frequency (wavenumber)
  u_s_2 = (sqrt((u_s_1.^2) + ...
      (u_s_1.^2)'))/(abs(min(x_vals))*100);

  % **************
  % Linear substep
  % **************

  for m = 1:Nmax,
    % FFT of field
    eval(['u_s_1 = field_' int2str(m) ';']);
    % propagation function
    eval(['u_s_3 = prop_func_' int2str(m) ';']);
    % RFSC truncation
    inx = find(u_s_2 <= ((((freq*m)/(c)) * ...
        sin(atan((-x_min)/z_step(idx))))));
    if (isempty(inx) == 0)
      u_s_2(:,:) = 0;
      u_s_2(inx) = u_s_3(inx);
    end;
    u_s_3 = (u_s_1 .* u_s_2);
    eval(['field_' int2str(m) ' = u_s_3;']);
  end

  for m = 1:Nmax,
    eval(['field_' int2str(m) ' = fftshift(field_'...
        int2str(m) ');']);
  end;

  eval(['fftw2(' st ',-1)']);

  for m = 1:Nmax,
    eval(['field_' int2str(m) ' = fftshift(field_'...
```

113

```
           int2str(m) ');']);
end;

% *****************
% Nonlinear substep
% *****************

for m = 1:Nmax,
  u_sum = zeros(N);
  for nn = 1:m–1,
    eval(['u_sum = u_sum + nn * field_' int2str(nn) ...
          ' .* field_' int2str(m–nn) ';']);
  end;
  for nn = m+1:Nmax,
    eval(['u_sum = u_sum + m * field_' int2str(nn) ...
          ' .* conj(field_' int2str(nn–m) ');']);
  end;
  eval(['u_s_' int2str(m) ' = u_sum;']);
end;

nl_coeff = i * beta * pi * freq * z_inc / (2 * c^2);

for m = 1:Nmax,
  eval(['field_' int2str(m) ' = field_' int2str(m) ...
        ' + nl_coeff * u_s_' int2str(m) ';']);
end;

% ************
% Save to disc
% ************

fwrite(fid1,c/rho*real(field_1(cent_pt,:)),'double');
fwrite(fid1,c/rho*imag(field_1(cent_pt,:)),'double');
if (Nmax > 1)
  fwrite(fid2,c/rho*real(field_2(cent_pt,:)),'double');
  fwrite(fid2,c/rho*imag(field_2(cent_pt,:)),'double');
end;
if (Nmax > 2)
  fwrite(fid3,c/rho*real(field_3(cent_pt,:)),'double');
  fwrite(fid3,c/rho*imag(field_3(cent_pt,:)),'double');
end;

t = [];
```

```matlab
    if (size(cr_sec,1) > 0)
      t = find((z_step(idx)-z_inc/2 <= cr_sec(1,:)) & ...
            (z_step(idx)+z_inc/2 > cr_sec(1,:)));
    end;
    if (t),
      for ii = 1:cr_sec(2,t);
        file_nm = strcat(strcat(strcat(strcat(strcat(strcat(...
            strcat('/local/tmp/hfjelles/'),...
            f_name),'_cr_'),num2str(ii)),'_'),num2str(...
            z_step(idx))),'.dta');
        fid = fopen(file_nm,'w');
        fclose(fid);
        fid = fopen(file_nm,'w');
        eval(['fwrite(fid,c/rho*real(field_',int2str(ii),...
            '(:)),''double'');']);
        eval(['fwrite(fid,c/rho*imag(field_',int2str(ii),...
            '(:)),''double'');']);
        fclose(fid);
      end;
    end;

    for m = 1:Nmax,
      eval(['field_' int2str(m) ' = fftshift(field_'...
            int2str(m) ');']);
    end;

    eval(['fftw2(' st ',1);']);

    for m = 1:Nmax,
      eval(['field_' int2str(m) ' = fftshift(field_'...
            int2str(m) ');']);
    end;

    fprintf('Inx finished : %d\n',idx);
  end;
  fclose(fid1);
  if (Nmax > 1),
    fclose(fid2);
  end;
  if (Nmax > 2)
    fclose(fid3);
  end;
  fprintf('Finished\n');
```